Fabrication of Distortion Free X-ray Masks Using Low Stress Tungsten

by

Yao-Ching Ku

Bachelor of Science
Electrical Engineering
University of South Florida
(1986)

Master of Science
Electrical Engineering
University of South Florida
(1986)

Submitted to the
Department of Electrical Engineering and Computer Science
in partial fulfillment of the requirements
for the degree of

Doctor of Philosophy

at the

MASSACHUSETTS INSTITUTE OF TECHNOLOGY

October 1991

© Massachusetts Institute of Technology 1991
All rights reserved.

Signature of the Author____________________________
Department of Electrical Engineering and Computer Science
October 3, 1991

Certified by____________________________
Henry I. Smith
Professor of Electrical Engineering
Thesis Supervisor

Accepted by____________________________
Campbell L. Searle
Chairman, Departmental Committee on Graduate Students

ARCHIVES

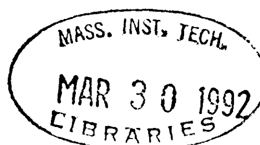

Fabrication of Distortion Free X-ray Masks Using Low Stress Tungsten

by

Yao-Ching Ku

Submitted to the Department of Electrical Engineering and
Computer Science on September 5, 1991 in partial fulfillment of the
requirements for the Degree of Doctor of Philosophy
in Electrical Engineering and Computer Science

Abstract

X-ray lithography is an emerging technology for future integrated circuit fabrication for linewidth of 0.5μm or below. There are two main criterion of applying x-ray lithography in production: x-ray source and mask technology. At this time, x-ray mask fabrication presents the greatest challenge. The two main elements of a x-ray mask are the membrane and absorber. Ideally a good x-ray mask should consist of high mechanical strength, high optical and high x-ray transmission membrane, together with a stress free absorber.

This thesis will address the problems associated with the membrane and absorber technology for x-ray masks. Particularly, I will focus on the technology to deposit low stress tungsten that is compatible with minimum feature size down to 0.1μm and below. The main difficulties in applying tungsten absorber are the high intrinsic stress in sputtered tungsten films, and the ability to control the stress down to 5×10^7 dynes/cm^2. This low stress film is required to minimize the distortion in a x-ray mask below one part per million. Methodologies used to deposit low stress tungsten films will be presented. Sputtered tungsten films were also characterized for their thermal and radiation stability. Measurement techniques and issues regarding the stress induced distortion (both in-plane distortion and out-of-plane distortion) were also discussed. An "in-situ" stress measurement technique, by monitoring the resonant frequency of the membrane, was developed. Experimental results correlating the measured membrane frequency response and the final measured film stress will be presented. Finally a comparison of various membrane materials and membrane characterization techniques will also be presented and discussed.

Thesis Supervisor: Henry I. Smith

Title: Professor of Electrical Engineering and Computer Science

Acknowledgement

I would like to thank my thesis adviser, Prof. Henry I. Smith, for his encouragement, guidance and support throughout the course of my study at MIT. He has provided a challenging and exciting environment to conduct research at the Submicron Structure Laboratory. It has been an enjoyable experience to work under him, particularly in sharing his enthusiasm towards his research and dedication to his work.

The successful completion of my thesis work would not have been possible without the strong support of our lab manager, Jimmy Carter. His dedication in maintaining the smooth operation of the lab, day or night, weekdays or weekends, is essential for anyone trying to finish up their thesis or research on time! I have to thank him for his patience in training me to work in the lab. Many times when I was in trouble and needed a hand, he was always be there for me.

It has been a great pleasure to work with Mark Schattenburg, Bill Chu, Tony Yen, Kathy Early, Alberto Moel, Martin Burkhardt, and Ray Ghanbari in the Submicron Structures Laboratory. I could not hope for a better group of people to work with and to learn from. Furthermore, I would like to thank the following undergraduates that I have work with during the past five years: Lee Peng Ng, Roger Carpenter, Kenneth Lu, Flora Tsai, and Vincent Wong. With their expert assistance, it has made my research work much more productive. Finally, I would like to thank Jeanne Porter, Mark Mondol, and Margaret Hamnett for their expert technical support throughout different phase of my research work.

I would like to dedicate this thesis to my mother, Shu Su Jung. Since my primary school, she has always encouraged me to be the best that I can be, and provided me with anything that's possible to achieve my goals. Her constant encouragement and caring has helped me overcome many obstacles throughout my years of studying.

Finally I would like to thank my whole family: Po-Tsan, Tsao-Chuen, Fan-Su, and my father Pao-Hsin for being there for me and taking care of me.

This work was supported by the Semiconductor Research Corporation and the Naval Research Laboratory (ONR Grant N00014-90-K-2108).

Table of Contents

Table of Contents....4
List of Figures....6
List of Tables....10
1. Introduction....11
2. Distortion Analysis and Measurements....17
2.1 Out-of-Plane Distortion....17
2.2 In-Plane Distortion....21
2.2.1 Finite Element Analysis for IPD....26
2.3 Distortion Measurement....34
2.3.1 OPD Measurement....34
2.3.2 IPD Measurement....37
2.3.2.1 Distortion Interpretation and Analysis....40
2.3.2.2 Measurement Procedure....45
2.3.2.3 Experimental Results....48
3. Low Stress Tungsten Sputtering....51
3.1 Sputtering of Stable α-W....52
3.2 Open Loop Process....55
3.3 Thermal and Radiation Stability....58
3.4 Stress Uniformity....60
4. In-situ Stress Monitoring....66
4.1 Basic Membrane Theory....67
4.2 In-situ Stress Monitoring System Set-up....68
4.3 Experimental Results....76
5. Membrane Characterization....83
5.1 Membrane Test Set-up....84
5.1.1 Bulge Test Measurement....84

5.1.2 Mechanical Properties Comparison Results....87
5.2 Other Measurement Techniques....90
5.2.1 Resonant Frequency Stress Measurement....90
5.2.2 Alpha Step Profilometer Stress Measurement....91
5.2.3 Fizeau Interferometer Stress Measurement....93
5.3 Additional Membrane Characterization Results....96
5.4 Radiation Stability of Nitride Membranes....98
6. Reactive Ion Etching of Tungsten....99
6.1 Experimental Results....100
6.2 Membrane Backside Cooling....109
7. Conclusion and Future Work....110
6.1 Conclusion....110
6.2 Future Work....111
Bibliography....113

List of Figures

Figure 1.1. Schematic of a x-ray mask compatible with x-ray wavelength of 1.3nm....12

Figure 1.2. Illustration of out-of-plane distortion induced by the absorber stress. From top to bottom showing absorber of compressive stress, zero stress, and tensile stress....14

Figure 1.3. A typical plot of tungsten stress versus sputtering pressure on Si membrane. Notice the sharp change in the stress over a small range of pressure....15

Figure 2.1. Cross-section view of the out-of-plane distortion (h), as a function of position....19

Figure 2.2. Sketch of top view and corss-sectional view of the model used for in-plane distortion analysis....22

Figure 2.3. Plot of theoretical calculation of maximum in-plane distortion versus absorber linewidth (or coverage area) for three different membrane materials. 25

Figure 2.4. Plot of in-plane distortion versus absorber stress for absorber linewidths of 100μm, 1mm, 5mm, and 1cm. 27

Figure 2.5. Comparison of in-plane distortion versus absorber linewidth calculated using Eq. 21 (the 1-D model) and finite element analysis (2-D model)....30

Figure 2.6. Comparison of in-plane distortion versus absorber stress calculated using Eq. 21 (1-D model) and finite element analysis (2-D model) for absorber linewidth of 2mm....31

Figure 2.7. Comparison of in-plane distortion versus absorber thickness calculated using Eq. 21 (1-D model) and finite element analysis (2-D model) for absorber stress of $1x10^8$ dynes/cm^2 of linewidth 2mm. 32

Figure 2.8. Plot of in-plane distortion in a x-ray mask, 31mm in diameter with an off-center absorber pad of 100x100µm and a stress of $5x10^7$ dynes/cm^2, for three different membrane materials. 33

Figure 2.9. Plot of in-plane distortion for absorber pads (2x2mm in size) and absorber lines (2mm in width) located at different positions on the mask. 35

Figure 2.10. Schematic of the Linnik interferometer used to measured the out-of-plane distortion induced by absorber stress, and the interferogram taken at the absorber-membrane step edge. 36

Figure 2.11. Linnik interferogram of the OPD measurement for a low stress tungsten film. 38

Figure 2.12. WYCO interferometer measurement at the membrane-absorber step edge for a low stress W film. (a) the deflection at the W side (8.4nm). (b) the deflection at the membrane side (2.81nm). 39

Figure 2.13. (a) Vector diagram representing distortion-free moire fringe patterns in k-space. (b) Vector diagram representing absorber induced distortion in the moire fringe patterns. (c) Illustration of moire fringe patterns expected on the front side of the membrane. 41

Figure 2.14. Illustration of in-plane distortion, δ, in a x-ray mask. 44

Figure 2.15. Fabrication procedures for grid reference membrane for in-plane distortion measurement. 46

Figure 2.16. Illustration for in-plane distortion measurement sequence. 47

Figure 2.17. (a) Photograph of moire fringe patterns obtained on the front side of the membrane. (b) Linnik interferogram of the OPD measurement at the backside of the membrane. 49

Figure 3.1. X-ray diffraction of α-phase W film. 53

Figure 3.2. X-ray diffraction of β-phase W film. 54

Figure 3.3. W film stress versus sputtering pressure over a narrow range of 16-17 mtorr. 56

Figure 3.4. Diagram depicting the repeatability of sputtering zero-stress tungsten. 57

Figure 3.5. Linnik interferograms at the W-membrane step edge before and after the exposure to heavy x-ray radiation of ~9800 J/cm^2....59

Figure 3.6. Linnik interferogram of the W absorber-membrane step edge taken on the backside of the membrane after the exposure to x-ray radiation of 9750 J/cm^2....61

Figure 3.7. Mapping of the OPD measured using Linnik interferometer and the corresponding absorber stress across the whole membrane. 62

Figure 3.8. Linnik interferograms taken at the center and at the edge of the membrane for W sputtered at an elevated temperature of 200°C. 64

Figure 4.1. Schematic of the holder stage for in-situ monitoring of resonant frequency....69

Figure 4.2. Plot of the frequency response for a membrane in vacuum using the in-situ frequency monitoring set-up....70

Figure 4.3. Schematic of the in-situ stress monitoring sputtering system....72

Figure 4.4. Inverting peak and hold circuit schematic....73

Figure 4.5. Front panel display from LABVIEW II for in-istu stress monitoring. 75

Figure 4.6. Plots of resonant frequency versus the sputtering time for three different sputtering pressure....77

Figure 4.7. Plots of resonant frequency versus sputtering time for two different sputtering runs and two different pressure control. The final film stress is less than $5x10^7$ dynes/cm^2....79

Figure 4.8. W absorber stress versus sputtering pressure for W film sputtered on the SiNx membrane over a small sputtering pressure range....80

Figure 4.9. Demonstration of the repeatability of getting zero stress W film on SiNx membranes using the in-situ stress monitoring system. 82

Figure 5.1. (a) Schematic of bulge tester set-up. (b) Typical plot of bulge tester measurement of pressure versus deflection. 85

Figure 5.2. Demonstration of the high strength of low stress LPCVD nitride membrane, used as a vacuum window for a x-ray system.......... 89

Figure 5.3. Sketch of resonant frequency measurement set-up in air.......... 92

Figure 5.4. Plots from Tencor Alpha-Step Profilometer scanning over wafer surface before and after nitride deposition. 94

Figure 5.5. Wafer topography, before and after nitride deposition, measured with Fizeau interferometer. One fringe represent a height differential of 316.4nm.......... 95

Figure 6.1. W etching profile using gas mixtures of $CHF_3/CCl_2F_2/O_2$ mixed at a flow ratio of 10:1:5, using novalak-based photoresist as etch mask.......... 101

Figure 6.2. Diagrams illustrating the holographic process used to prepare samples for W RIE.......... 102

Figure 6.3. Scanning electron micrograph of W etching profile using $CHF_3/CCl_2F_2/O_2$ mixed at a flow ratio of 27:9:8, at a bias voltage of 105 volts and at a pressure of 8 mtorr.......... 104

Figure 6.4. Scanning electron micrograph of W etching profile using $CHF_3/CCl_2F_2/O_2$ mixed at a flow ratio of 20:9:8, at a bias voltage of 600 volts and at a pressure of 8 mtorr.......... 105

Figure 6.5. Top view shows 100nm period W grating lines for a x-ray mask etched using $CHF_3/CCl_2F_2/O_2$. Bottom graph shows the 100nm period PMMA lines exposed using the W x-ray mask shown on the top.......... 106

Figure 6.6. Plot of W etch rate versus gas flow ratio of SF_6 in CHF_3. A higher SF_6 flow ratio resulted in a faster etch rate and less directionality in the etching profile.......... 107

Figure 6.7. Scanning electron micrograph of W etching profile using SF_6/CHF_3 mixed at a flow ratio of 1:1.8, at a bias voltage of 600 volts and at a pressure of 10mtorr.......... 108

List of Tables

Table 1 Membranes characterization and comparison table. 88

Table 2. Nitride deposition parameters from three different sources.......................... 97

Chapter 1

Introduction

One of the main challenges in applying x-ray lithography technology in practical very-large-scale integrated circuit (VLSI) fabrication is developing masks with high pattern placement accuracy. Figure 1.1 depicts a general schematic of a x-ray mask that is used at x-ray wavelength of 13Å. The mask consists of a thin membrane, approximately 1μm thick, with its Si frame anodically bonded to a Pyrex ring. Some of the typical membrane materials are Si, SiNx, SiC, and diamond. The desired circuit pattern to be replicated are defined in the absorber deposited on top of the membrane. Optimal absorber materials are gold or tungsten. The thickness of the absorber is chosen so that it will provide 10dB attenuation at x-ray wavelength of 13Å. Controlling the absorber film stress in x-ray masks is essential to obtain high-accuracy, distortion free masks [1-2]. Since any stress in the absorber will induce undesirable in-plane distortion (IPD) and out-of-plane distortion (OPD), as shown in Figure 1.2, the magnitude of the stress must be maintained at a low enough value to prevent this problem. In the sub-micron regime, for a mask area of $4cm^2$ and a minimum feature size of 0.25μm, the maximum in-plane distortion allowed is one

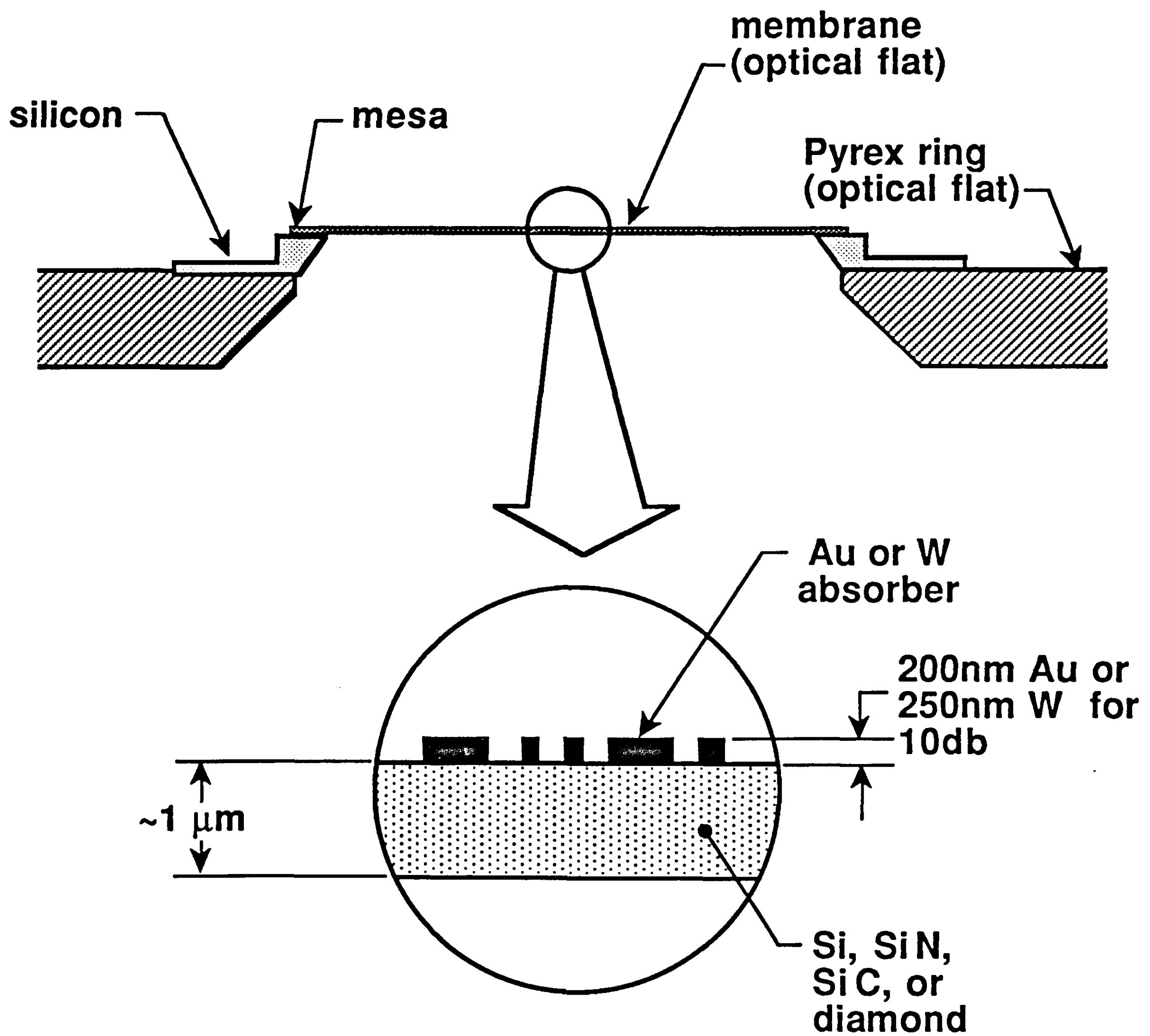

Figure 1.1. Schematic of a x-ray mask compatible with x-ray wavelength of 1.3nm.

part per million (i.e. 40nm), or an equivalent stress of 2×10^8 dynes/cm^2 [1-2]. In my thesis I will be focusing on the problems associated with fabricating distortion-free x-ray masks.

There are several options for the absorber material used in x-ray mask technology. Many researchers have been experimenting with methods of depositing low stress tungsten as the the x-ray absorber material. There are several reasons for choosing tungsten over other materials such as gold(Au) or tantalum(Ta). Although Au is the traditional absorber material used, W and Ta are promising alternatives because both materials can be deposited and reactive-ion etched by dry processes that are compatible with conventional IC manufacturing. However, tungsten appears to be the better absorber material than tantalum because it has higher x-ray absorption, 38.2 dB/μm at λ=1.33 nm versus 31.5 dB/μm for Ta. In addition, when x-ray masks are exposed to repetitively pulsed plasma source of x-ray, the mask is subject to thermal cycling. For this reason it is highly desirable to have a good thermal match between the x-ray mask membrane and the absorber. Tungsten, with a thermal expansion coefficient of $4.3 \times 10^{-6} K^{-1}$, provides a better match to most of the inorganic membrane materials such as SiC($4 \times 10^{-6} K^{-1}$), Si($2.6 \times 10^{-6} K^{-1}$), Si_3N_4($2.7 \times 10^{-6} K^{-1}$), and Diamond($1.2 \times 10^{-6} K^{-1}$), than Au($14.3 \times 10^{-6} K^{-1}$) or Ta($6.5 \times 10^{-6} K^{-1}$). Tungsten is also a refractory metal, thus it should not undergo changes in grain structure or internal stress over time.

Although W is a desirable absorber material, there are several problems which need to be resolved before it can be used as an x-ray absorber. The first problem is that tungsten, deposited by either a sputtering or a CVD process[3], can have an internal stress on the order of 10^9-10^{10} dynes/cm^2 [4-13], which causes unacceptable in-plane and out-of-plane distortion in the mask. In the sputtering process, the internal stress of tungsten is a strong function of the deposition parameters, as shown in Figure 1.3. As we can see from the figure, there is a large change in the internal stress from highly compressive to

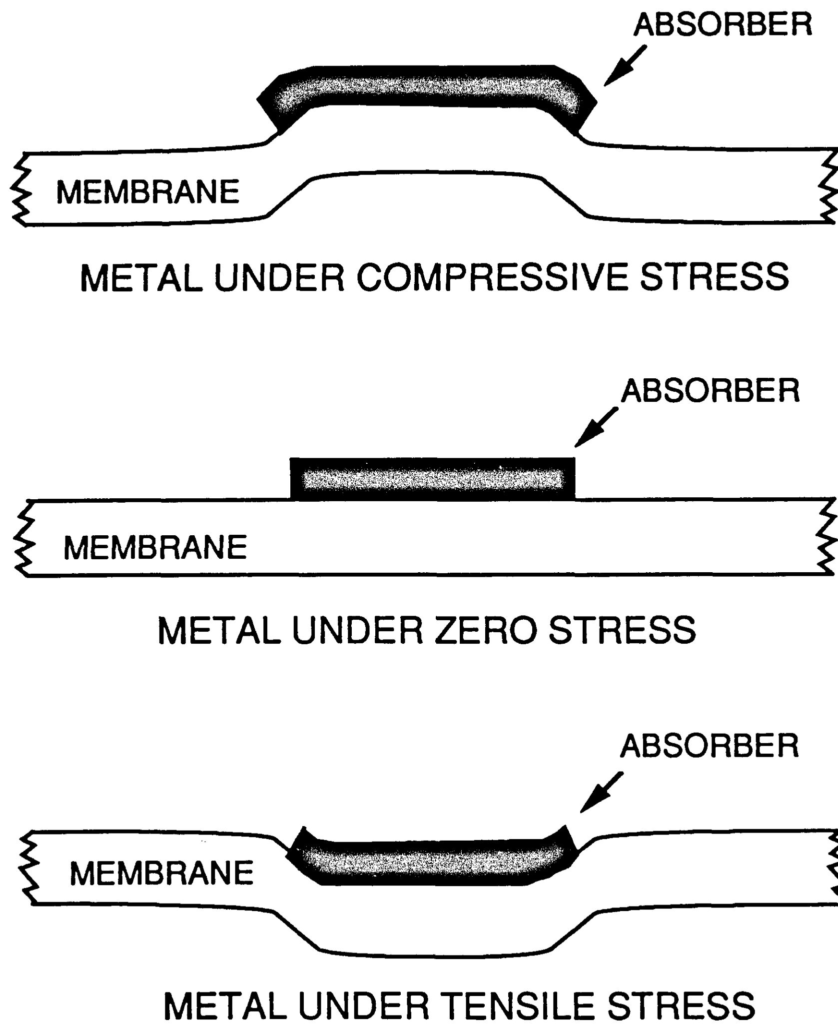

Figure 1.2. Illustration of out-of-plane distortion induced by the absorber stress. From top to bottom showing absorber of compressive stress, zero stress, and tensile stress.

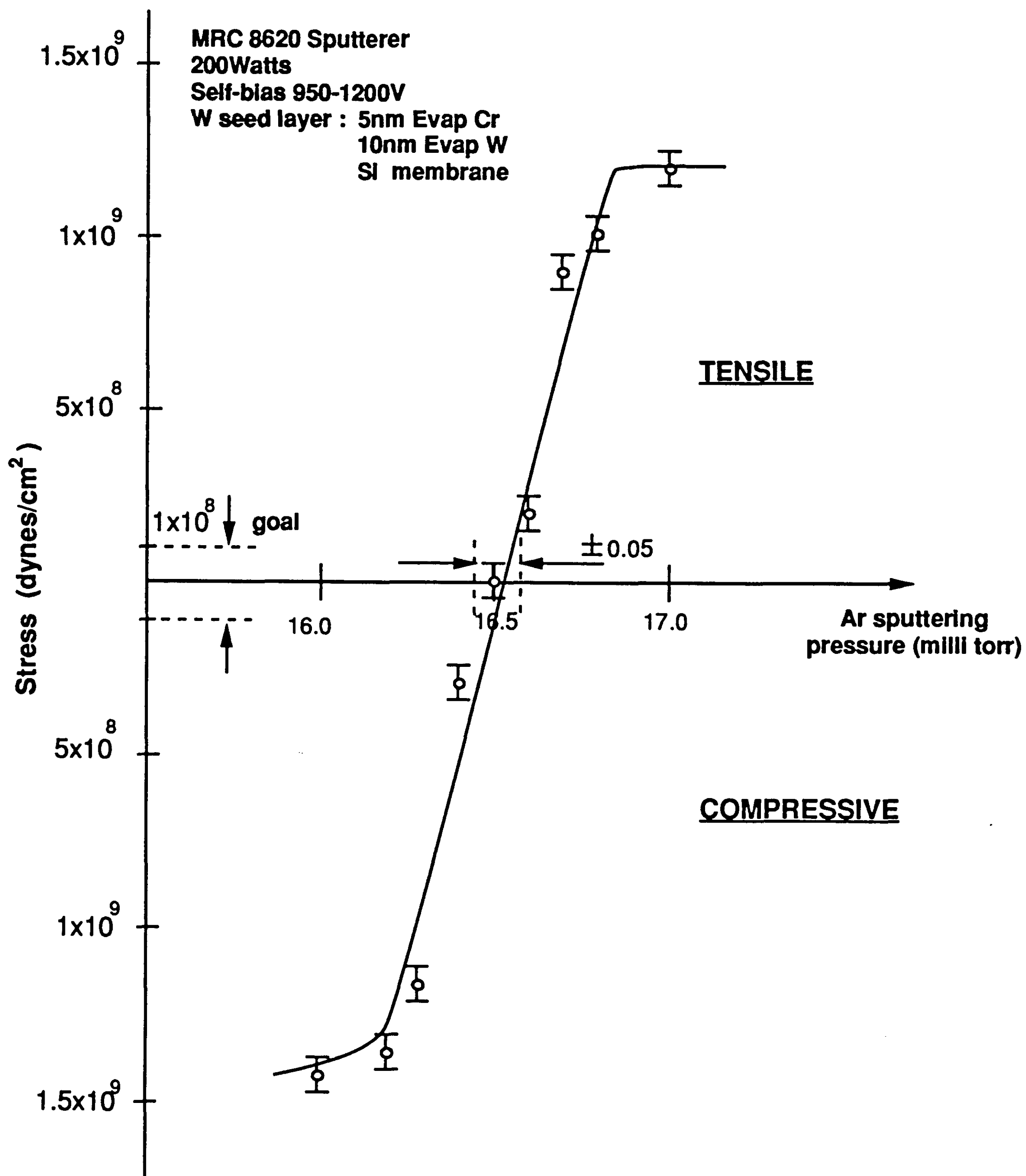

Figure 1.3. A typical plot of tungsten stress versus sputtering pressure on Si membrane. Notice the sharp change in the stress over a small range of pressure.

highly tensile over a small range of pressure (~0.5mtorr). The second problem is the existence of both metastable β–phase tungsten and stable α-phase tungsten [10,14-16]. β–phase W undergoes changes in its internal structure when it is subjected to high temperature annealing and is transformed into α-phase W. This change in the internal structure is accompanied by a change in the stress of the W film, which can be very problematic for an x-ray mask. Finally, a process for reactive-ion etching the tungsten [17-23] of 400nm thickness at a linewidth of 0.25 μm or below has not been fully developed. Therefore in the following chapters these issues will be addressed, and the experimental results will be presented.

Additional critical consideration for a good x-ray mask technology is the choice of mask membrane materials. A mask must be mechanically strong, optically transparent (for optical alignment), free of radiation damage, and easy to fabricate. There are several strong candidates that are being considered for the membrane application. Methodologies used to test and compare these materials will be presented in Chapter 5 to identify the "best" membrane materials.

Chapter 2

Distortion Analysis and Measurements

In order to understand the mask distortion induced by the stress of the absorber, basic mechanical equations that describe the membrane-absorber interaction will be developed. Stress causes both in-plane and out-of-plane distortion. Out-of-plane distortion (OPD) is more of a concern in point-source x-ray lithography than in synchrotron-based x-ray lithography. In-plane-distortion (IPD) is of greater concern for overall circuit overlay accuracy. In this section the origin of these two distortions will be analyzed and discussed. The correlation of IPD and OPD will also be studied.

2.1 Out-of-Plane Distortion

The two basic equations, proposed by Yanof et al.[1], that are used to model the membrane deflection due to the bending from the absorber stress and the membrane tension are given as follow:[24]

$$\frac{d^2\eta}{dx^2} = -\frac{\sigma_a t_a (t_s + t_a)}{2D} + \frac{\eta \sigma_s' t_s}{D}, \qquad x > 0$$
$$\frac{d^2\eta}{dx^2} = \frac{\sigma_s' t_s}{D'} \eta, \qquad x < 0 \qquad (1)$$

where η is the downward deflection of the membrane, σ_a and t_a are the absorber stress and thickness, σ_s and t_s are the substrate stress and thickness, the primed terms are the membrane properties in the region $x < 0$, and unprimed terms are the membrane properties modified by the absorber. Figure 2.1 depicts the bending (η) of the membrane at the absorber - membrane step edge. D' is the stiffness of the membrane which is defined as:

$$D' = \frac{E_s t_s^3}{12(1 - \nu_s^2)} \qquad (2)$$

where E_s is the Young's modulus of the the substrate membrane, and ν_s is the Poisson's ratio for the substrate. Under the absorber region, the effective D should be calculated as the weighted average of the layer properties of both the membrane and the absorber film as follow:

$$D = \frac{1}{t_s + t_a} (D' t_s + D_a t_a) \qquad (3)$$

Solving the differential equations in (1), the solutions obtained are:

$$\eta = K \lambda^2 (1 - e^{-x/\lambda}) + \eta_o e^{-x/\lambda}, \qquad x > 0 \qquad (4)$$

$$\eta = \eta_o e^{-x/\lambda'}, \qquad x < 0 \qquad (5)$$

where K and λ are defined as follow:

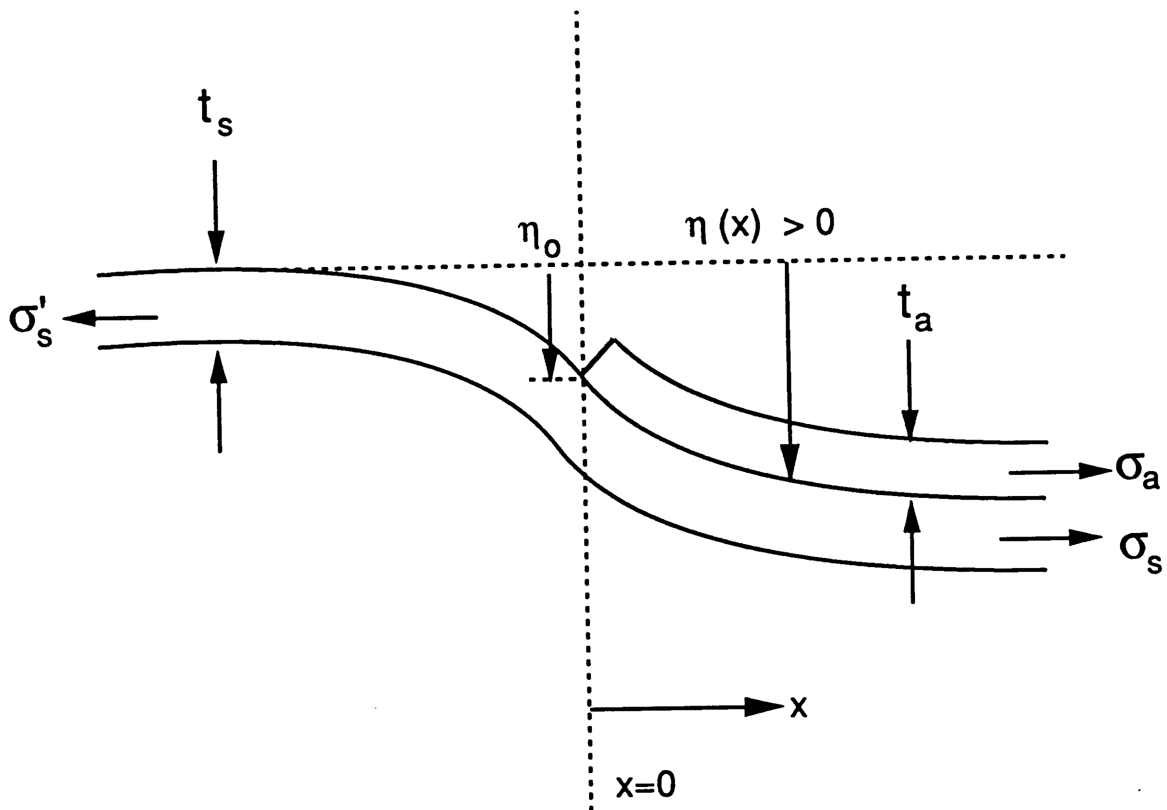

Figure 2.1. Cross-section view of the out-of-plane distortion (η), as a function of position.

$$K = \frac{\sigma_a t_a (t_s + t_a)}{2D} \tag{6}$$

$$\lambda = \sqrt{\frac{D}{\sigma_s' t_s}} \tag{7}$$

$$\lambda' = \sqrt{\frac{D'}{\sigma_s' t_s}} \tag{8}$$

η_o is the deflection at the absorber-membrane step edge, and it is determined from eq.(4) to be:

$$\eta_o = \frac{K \lambda^2}{1 + \lambda / \lambda'} = \frac{\sigma_a t_a (t_s + t_a)}{2 \sigma_s' t_s} \frac{1}{1 + \lambda / \lambda'} \tag{9}$$

As shown in the expression, the deflection at the step-edge is only dependent on the ratio of the stiffness through the characteristic length λ. The ratio of the stiffness, D / D', on either side of the step edge is:

$$\frac{D}{D'} = \frac{t_s + (\frac{D_a}{D'}) t_w}{t_s + t_w} \tag{10}$$

where $\frac{D_a}{D'} = \frac{E_a t_a^3 (1 - \nu_s^2)}{E_s t_s^3 (1 - \nu_a^2)}$

For example, with a 0.4μm thick W absorber ($\nu_a = 0.4$, $E_a = 3.45 \times 10^{12}$ dynes/cm^2) on top of 1μm thick Si membrane ($\nu_s = 0.279$, $E_s = 1.3 \times 10^{12}$ dynes/cm^2), giving a D/D' ratio of 0.186, and a λ/λ' ratio of 0.876. Therefore, usually in the worst case, i.e. λ/λ' equals 1, eq.(9) can be rewritten in the form that relates the absorber stress to the deflection at the absorber-membrane step edge η_o as:

$$\sigma_a = \frac{4 \sigma_s' \eta_o}{t_a (1 + \frac{t_a}{t_s})} \tag{11}$$

Alternatively, if we re-write eq.(4) and calculate the deflection, η_∞, as x approaches ∞, the total deflection can be calculated to be:

$$\eta_\infty = K\lambda^2$$

$$\sigma_a = \frac{2\,\sigma_{s'}\,\eta_\infty}{t_a\,(1+\frac{t_a}{t_s})} \qquad (12)$$

Both eq.(11) and (12) shows that the stress of the tungsten absorber is directly proportional to the measured out-of-plane distortion, η. Alternatively, OPD can be minimized by either reducing the absorber stress or increasing membrane tensile stress.

2.2 In-Plane Distortion

One dimensional calculation for the in-plane distortion will be analyzed in this section. Figure 2.2 shows the model that is used for the in-plane distortion analysis. This figure depicts the absorber of linewidth l centered on the mask and stretched across the whole mask of diameter L (or length L for a square membrane). The basic governing equations for the in-plane distortion is as follow:[25-26]

$$\frac{\partial^2 u_x}{\partial x^2} + \frac{1-\nu}{2}\frac{\partial^2 u_x}{\partial y^2} + \frac{1+\nu}{2}\frac{\partial^2 u_y}{\partial x \partial y} = 0 \qquad (13)$$

$$\frac{\partial^2 u_y}{\partial y^2} + \frac{1-\nu}{2}\frac{\partial^2 u_y}{\partial x^2} + \frac{1+\nu}{2}\frac{\partial^2 u_x}{\partial x \partial y} = 0 \qquad (14)$$

where $u_{x,y}$ are the x and y displacement from the equilibrium after the absorber has been patterned. For a one dimensional problem, the above equations can be simplified to:

$$\frac{\partial^2 u_x}{\partial x^2} = 0 \qquad (15)$$

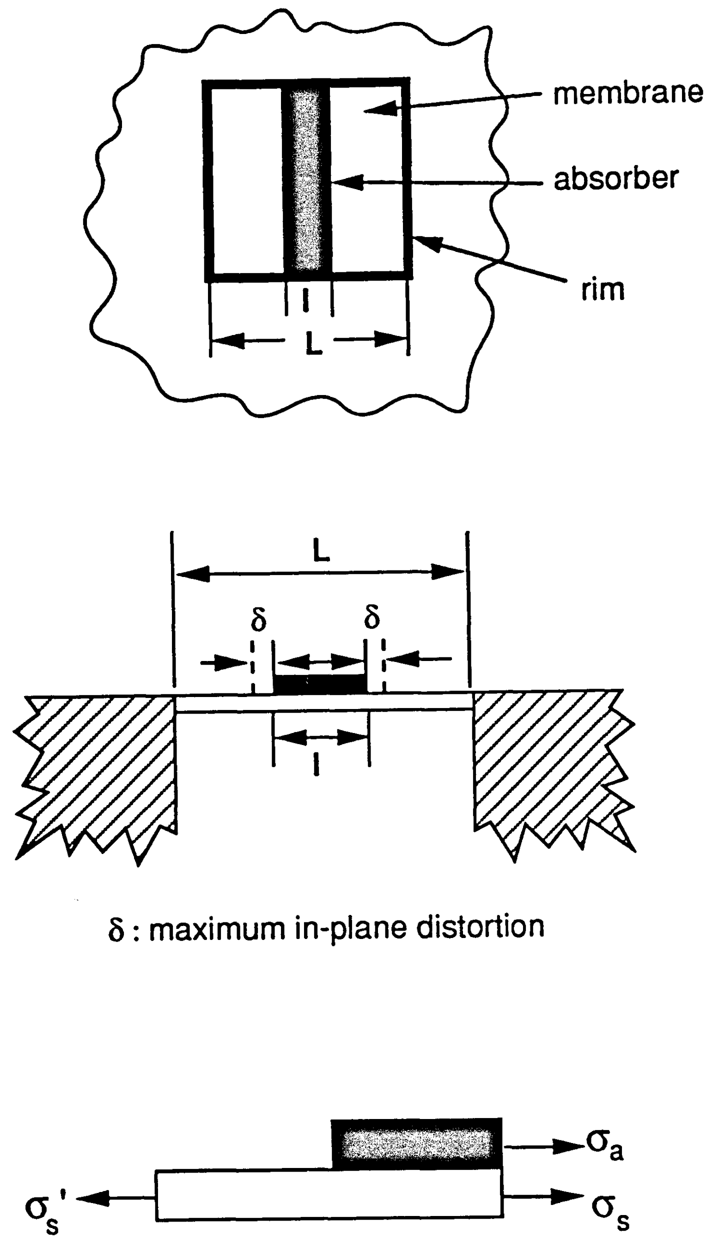

Figure 2.2. Sketch of top view and corss-sectional view of the model used for in-plane distortion analysis.

which means that $\partial u_x/\partial x$, the strain ε_x, is a constant. By applying the continuity of the displacement at the absorber feature boundaries and setting the displacement at the edge and at the center of the mask to be zero, the in-plane displacement, u_x, can be shown to vary linearly from zero (at the mask boundary) to its maximum δ (at the absorber feature boundary). Also from the balance of force at the absorber feature boundary, the applied force σ_a creates a discontinuity in the stress:

$$\sigma_a t_a = t_s(\sigma_s' - \sigma_s) \quad (16)$$

and according to Hooke's Law,

$$\frac{\partial u_x}{\partial x} = \frac{\sigma_x}{E_s} - \frac{\nu\, \sigma_y}{E_s} \quad (17)$$

$$\frac{\partial u_y}{\partial y} = \frac{\sigma_y}{E_s} - \frac{\nu\, \sigma_x}{E_s} \quad (18)$$

this discontinuity created by the absorber stress will induce discontinuity in the derivatives of in-plane displacement u_x (strain ε_x). For the one-dimensional problem, the Hooke's law simplifies to:

$$\varepsilon_x = \frac{\partial u_x}{\partial x} = \frac{1-\nu^2}{E_s}\,\sigma_x \quad (19)$$

The displacement in the absorber region increases linearly from 0 at the center of the mask to δ at the absorber feature edge, which gives a strain of $-2\delta/l$. Similarly, the displacement in the membrane region increases linearly from 0 at the edge of the membrane to δ at the absorber feature edge, which gives a strain of $2\delta/(L-l)$. By taking into account the multi-layered membrane properties on the absorber side, and applying eq.(19) to both regions on the mask, eq.(16) can be rewritten as:

$$\frac{\sigma_a t_a}{t_s} = \frac{E_s'}{1 - \nu^2} \frac{2\delta}{L - l} + \frac{E_s' t_s + E_a t_a}{(t_s + t_a)(1 - \nu^2)} \frac{2\delta}{l} \tag{20}$$

After a few algebraic manipulation, the maximum distortion δ can be rewritten as:

$$\delta = \frac{\varepsilon_a (1 - \nu^2)(1 - k)\, l}{(1 - k\beta)} \tag{21}$$

where

$$k = \frac{l}{L}$$

$$\varepsilon_a = \frac{\sigma_a t_a}{E_s' t_s + E_a t_a}$$

$$\beta = \frac{E_a t_a}{E_s' t_s + E_a t_a}$$

Equation (21) gives the functional dependence of maximum distortion, δ, at one side of the feature in this one dimensional model as a function of various membrane-absorber properties (such as stress and Young's modulus). This equation, giving a more accurate in-plane distortion calculation than the form given by Yanof[1], took into account the differences in the stiffness between the area under the absorber and the clear area of the membrane.

To gain some insight of the in-plane distortion dependence on various x-ray mask material properties, the functional dependence of the IPD [27-28] was plotted as a function of a few of these parameters. Figure 2.3 shows the theoretical calculation of the maximum in-plane distortion predicted for a 0.4 μm thick tungsten absorber, with a tensile stress of 5×10^7 dynes/cm^2, that stretches across the center of the membrane (2 cm in diameter) for four different membrane materials and different absorber linewidths. Two observations can be made from the plots shown in Fig. 2.3. First of all IPD decreases with higher membrane Young's modulus, particularly for diamond membrane (a Young's modulus of 1×10^{13} dynes/cm^2) the distortion introduced by the W absorber is almost insignificant (< 1 part per million, i.e. < 10nm). Also SiC, which is anticipated to be the future membrane

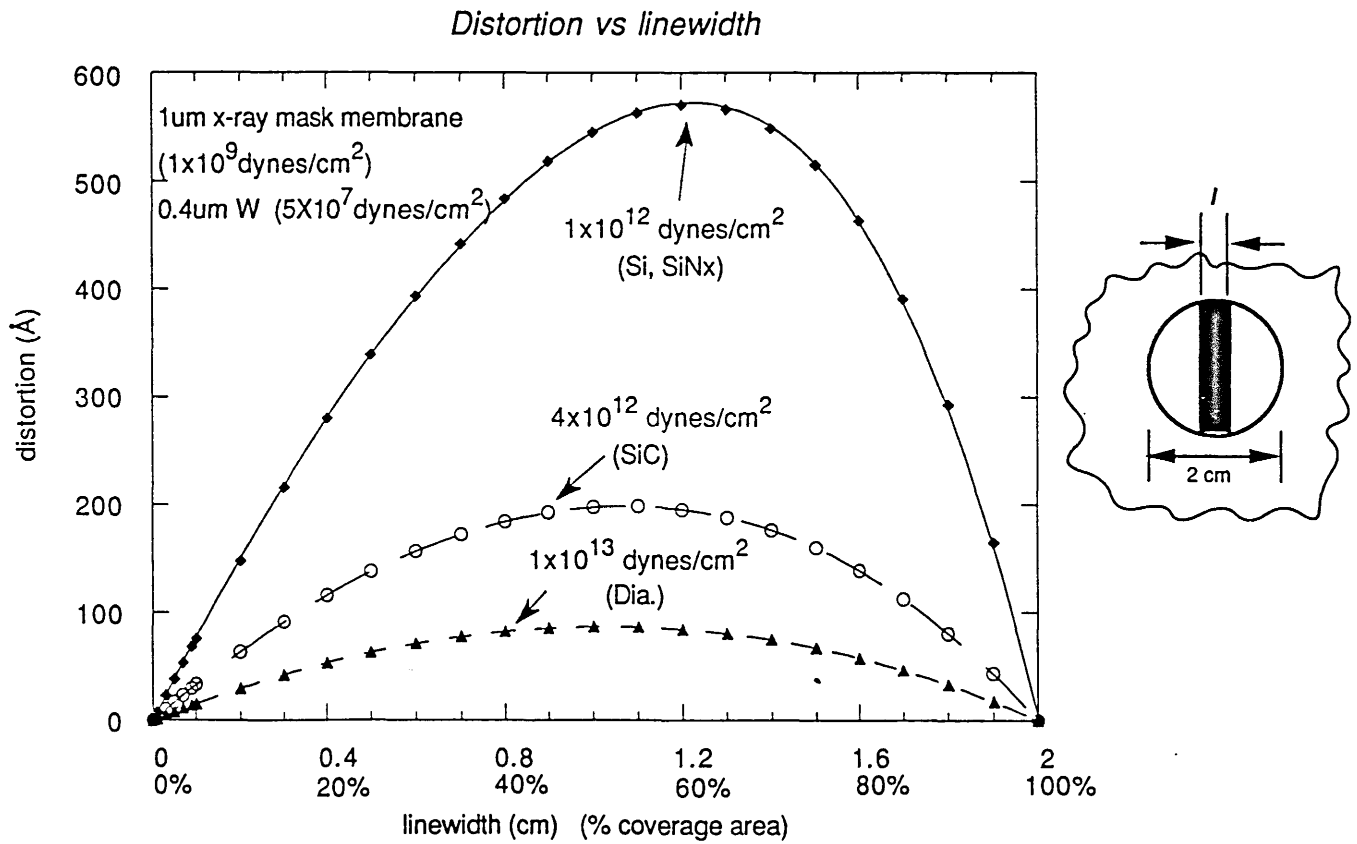

Figure 2.3. Plot of theoretical calculation of maximum in-plane distortion versus absorber linewidth (or coverage area) for three different membrane materials.

material, has 4 times the Young's modulus of Si or SiNx and shows a 3 time reduction in the IPD. Second of all, the IPD increases with increasing absorber coverage area, until it reaches the maximum (around 60% coverage area), then it decreases to zero at 100% coverage. Figure 2.4 depicts the maximum IPD calculated as function of absorber stress for a few selected absorber linewidths. Again, it shows the non-linear dependence of the IPD as function of the absorber stress. However, for most practical circuit layouts, actual pattern features are usually small, less than 1mm, with 100μm pads considered large. Figure 2.4 shows that for pattern feature size of 1mm or less, the maximum in-plane distortion introduced by absorber of stress 1×10^8 dynes/cm^2 or less is smaller than 20nm (i.e. < 1 part per million). Therefore if the stress of the absorber is controlled down to 1×10^8 dynes/cm^2 or below, it is sufficient to use membrane materials such as Si or SiNx, i.e., one does not need to use materials of higher Young's Modulus such as SiC or diamond. Clearly as shown in Fig. 2.3 and 2.4, the key to minimize IPD is to either decrease absorber stress or increase membrane Young's modulus.

2.2.1 Finite Element Analysis for IPD

In this section, a procedure for doing the finite element analysis will be described. The main purpose of this analysis is to further the understanding of IPD for some arbitrary 2-D geometries which does not have simple closed form solution as shown in the previous section. The FEM program used for the analysis is ADINA. Discretization of the elements, the material properties and the boundary conditions are required for the inputs. The masks (both membrane and the absorber) were modeled as linear elastic materials with uniform biaxial residual stress. The residual stress of the film and the absorber was generated as thermal stress by a thermal difference between the film and a reference

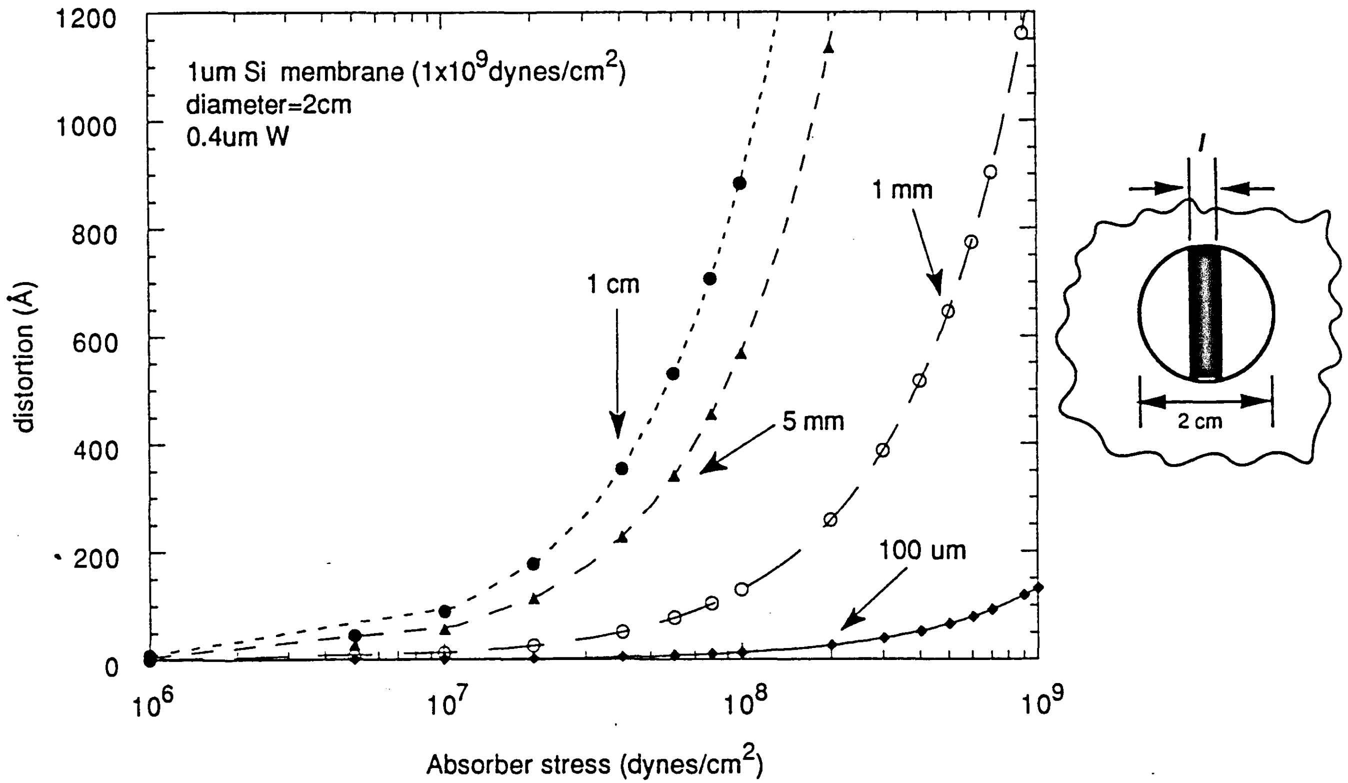

Figure 2.4. Plot of in-plane distortion versus absorber stress for absorber linewidths of 100μm, 1mm, 5mm, and 1cm.

temperature.

A x-ray mask is usually a three-dimensional structure. The mask usually consists of a thin membrane and an absorber layer covering some part of the membrane. The thickness of the membrane is typically 1-2μm thick, and has a length (or diameter) of 2-3 cm. Since the mask has such a large aspect ratio differences (i.e., a factor of 1000 larger for the membrane diameter as compared to membrane thickness), it can be treated as a two-dimensional structures. The x-ray mask, including the membrane and the absorber, was discretized on a rectangular grid. The spacing between the adjacent nodes on the grid is small compared to the minimum absorber feature size on the membrane. In the analysis "shell" elements with 4 nodes and 8 nodes were used for the 2-dimensional structures representation of discrete elements. The main difference in using the larger number of nodes for the same shell elements is that a higher order integration routine will be used. The absorber element was simulated on top the membrane by specifying the boundary and internal nodal points of the absorber to coincide with the membrane nodal points. Using the FEM, variables such as the number of absorbers on the mask, the location of the absorbers on the membrane, and the geometry of the membrane can all be described and simulated. This, in turn, will gave a better understanding of the in-plane distortion in a x-ray mask.

The first goal for the analysis is to check against the theoretical 1-D model developed in the earlier section. In order to accurately describe the same mask configuration for comparison purpose, it is important to establish an equivalent mask configuration for both 1-D and 2-D models. In 1-D model the absorber is stretched all along the mask with a given linewidth. This implies that at any cross-section of the mask perpendicular to the absorber line as shown in Fig. 2.2, the ratio of the absorber linewidth to the membrane length is the same. Therefore the important parameter, that should be

consistent in comparing these two models, is the ratio of absorber area to the membrane area and the location of the absorber on the membrane for the 2-D model to be the same as 1-D model. Also for simulation and comparison purposes, a Si membrane with a diameter of 2cm and W absorber stress of 1×10^8 dynes/cm^2 was chosen. Figure 2.5 shows the in-plane distortion for both 1-D and 2-D model as a function of absorber coverage area on the membrane assuming the absorber line are centrally located on the mask. This shows that the 2-D model follow the trend predicted by the 1-D model very well but gives a smaller value of distortion. Similarly Fig. 2.6 and Fig. 2.7 plot the in-plane distortion as function of absorber stress for an absorber linewidth of 2mm, and as function of absorber thickness for an absorber stress (1×10^8 dynes/cm^2) and linewidth (2mm) respectively. In both cases, the 2-D model follow the trend predicted by the 1-D model very well, but in both cases 2-D analysis give smaller distortion values as compared to the 1-D model.

Once the equivalence for the 1-D and 2-D model has been established, the next goal would be simulating absorbers of various geometries and locations on the membrane to further understand the distortion as a function of these parameters. Only a few selected examples will be presented here. In the first example, a large off center pad of the size 100x100μm and 0.263 μm in thickness sitting on a circular membrane of thickness 1μm and of diameter 31mm was studied. Figure 2.8 shows the in-plane distortion for this mask configuration as a function of 3 different membrane materials. Surprisingly, the distortion is in the order of a few Å with an absorber stress of 5×10^7 dynes/cm^2. Diamond membrane, with the highest Young's modulus among all the three materials, shows an order of magnitude smaller value in the distortion as compared to a typical Si or SiN_x membranes. Even though the diamond membrane shows the smallest IPD, membranes such as Si or SiNx shows an negligible IPD of ~2Å. Therefore with a low stress absorber,

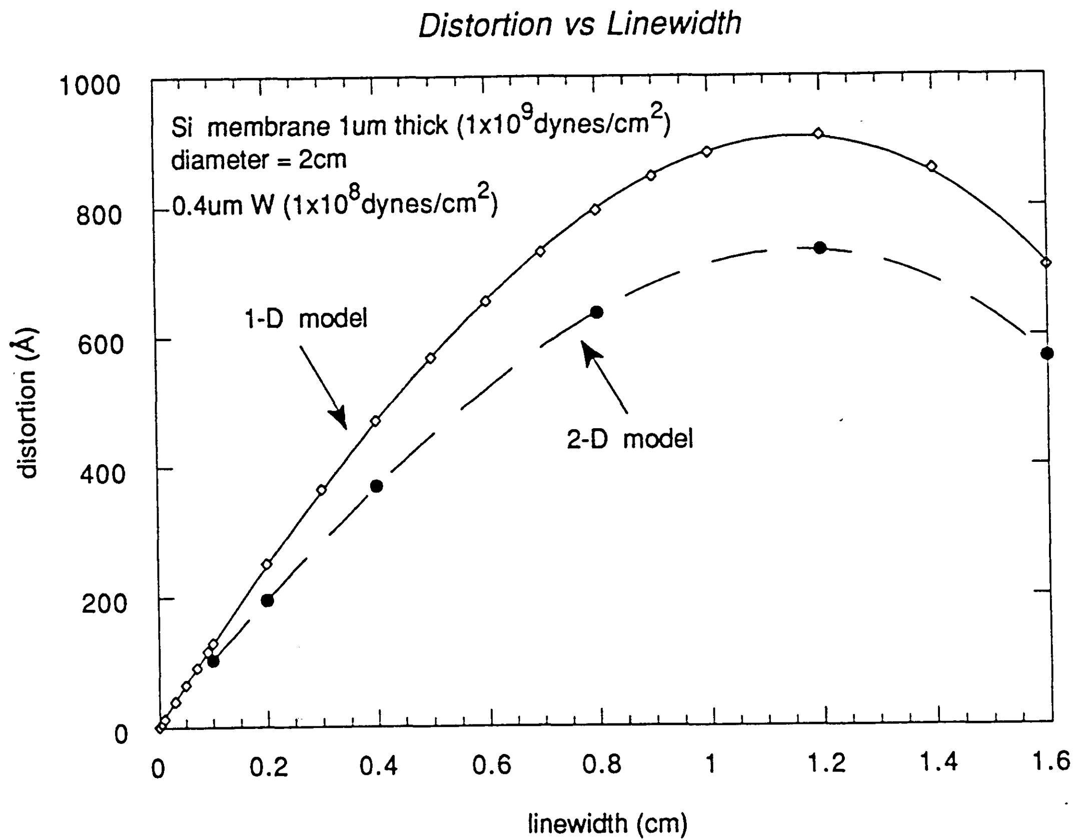

Figure 2.5. Comparison of in-plane distortion versus absorber linewidth calculated using Eq. 21 (the 1-D model) and finite element analysis (2-D model).

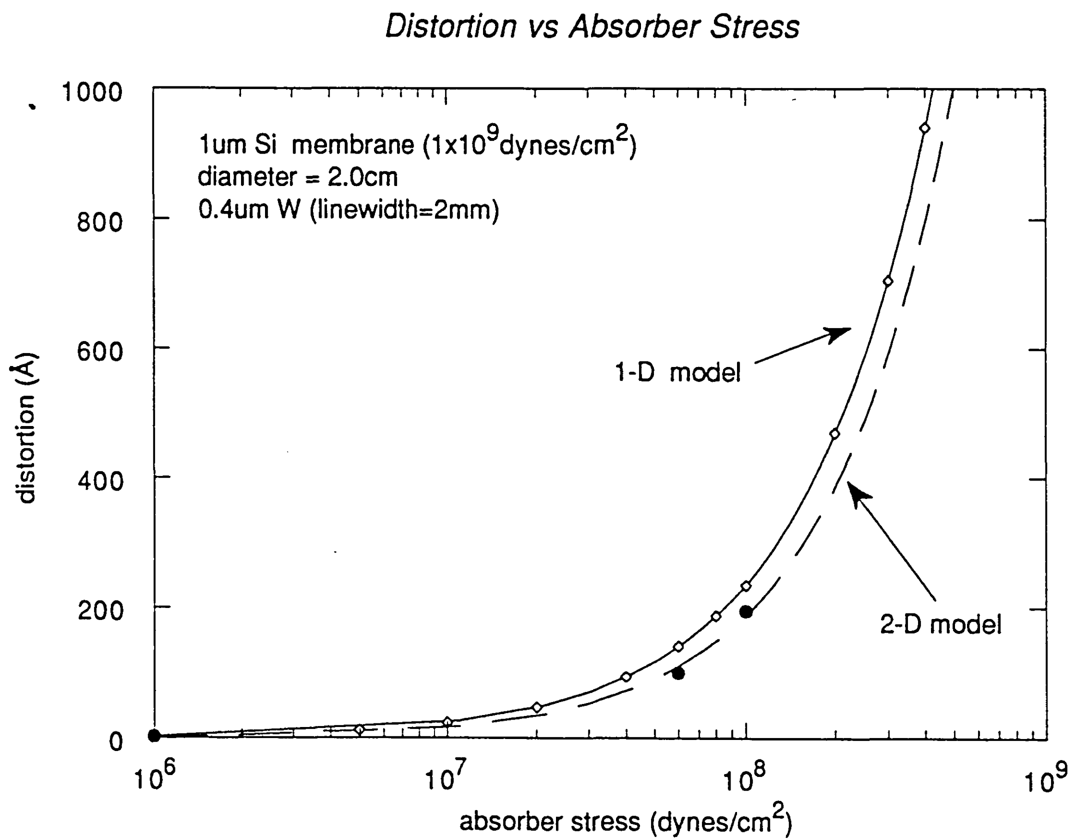

Figure 2.6 Comparison of in-plane distortion versus absorber stress calculated using Eq. 21 (1-D model) and finite element analysis (2-D model) for absorber linewidth of 2mm.

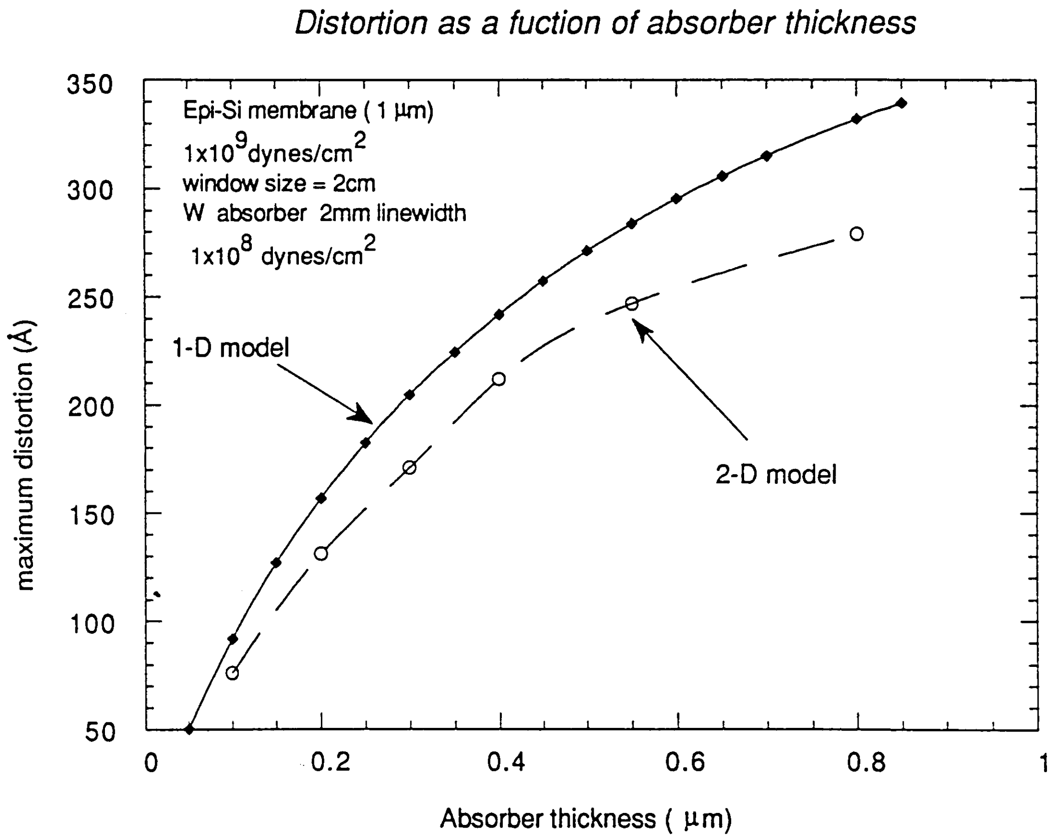

Figure 2.7 Comparison of in-plane distortion versus absorber thickness calculated using Eq. 21 (1-D model) and finite element analysis (2-D model) for absorber stress of $1x10^8$ dynes/cm^2 of linewidth 2mm.

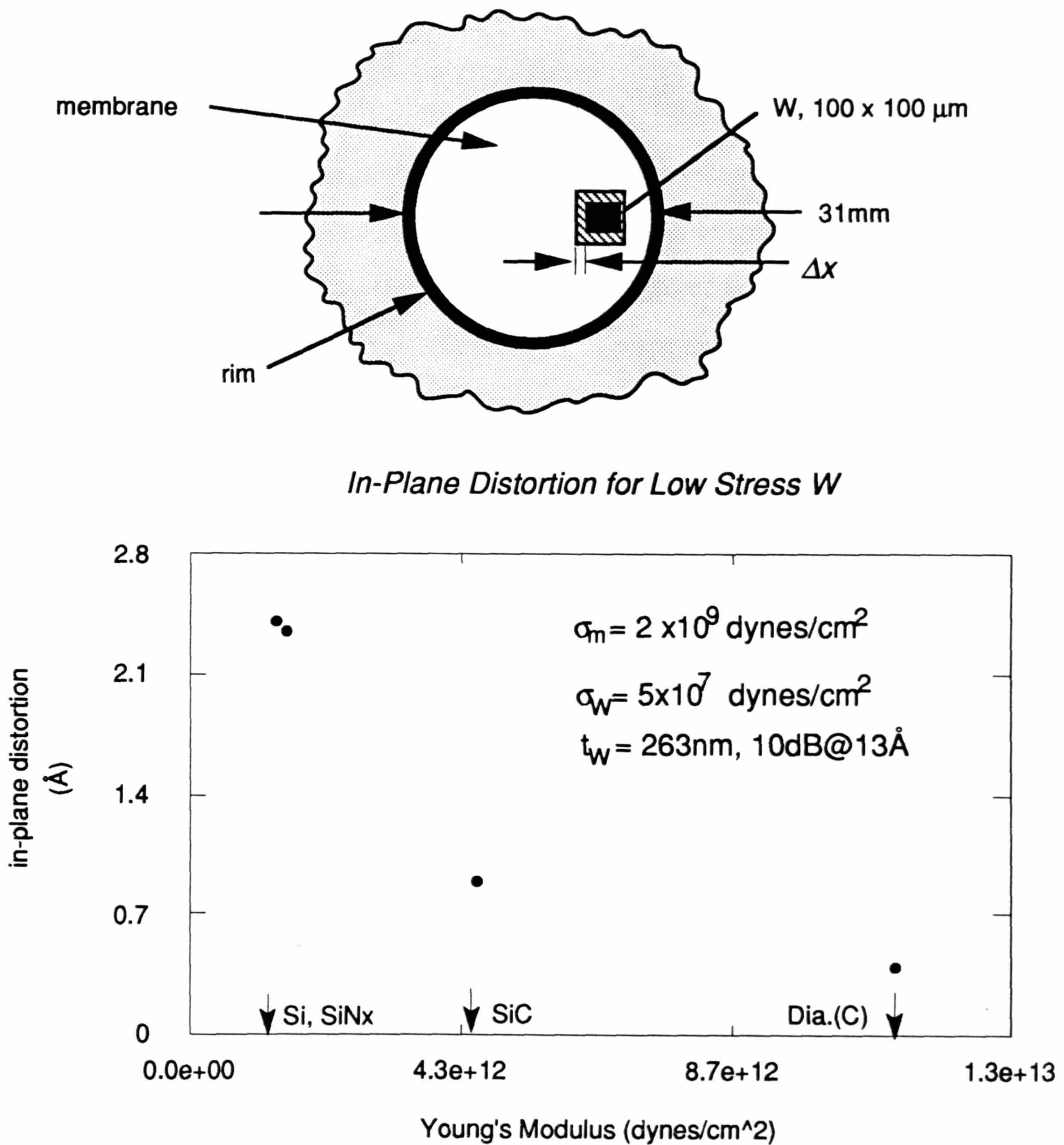

Figure 2.8 Plot of in-plane distortion in a x-ray mask, 31mm in diameter with an off-center absorber pad of 100x100µm and a stress of $5x10^7$ dynes/cm^2, for three different membrane materials.

a mature membrane technology (such as SiNx) provides a better choice as membrane material for x-ray mask.

In the second example, the effect of pattern placement and the resulting in-plane distortion were simulated. In this example the minimum pattern linewidth used for the simulation was 2mm. Patterns such as square of 2mm in length, and lines of 2mm in width which are stretched across the whole membranes, placed at different locations of the mask membranes were simulated and the resulting in-plane distortion is shown in Fig. 2.9. As shown in the figure, an asymmetrically placed absorber introduced almost 50% more IPD than a symmetrically placed absorber. This example demonstrate that by using the FEM simulation [28], various circuit layout patterns and placements on a mask membrane can be simulated and analyzed, and a minimum in-plane distortion configuration can be obtained.

2.3 Distortion Measurement

2.3.1 OPD Measurement

For direct OPD measurement and to extract the absorber stress from the OPD measurement, a Linnik interferometer was used. Figure 2.10 shows a typical Linnik interferogram observed using a Linnik interferometer. This interferometer equipped with a matched pair of 100X, 0.95 NA objective lenses. This technique is advantageous because measurements are done directly on a x-ray mask membrane and it is also very accurate. In the Linnik measurement, the stress of the absorber is related directly to the out-of-plane distortion, and the relationship of the stress vs distortion measured are given by:

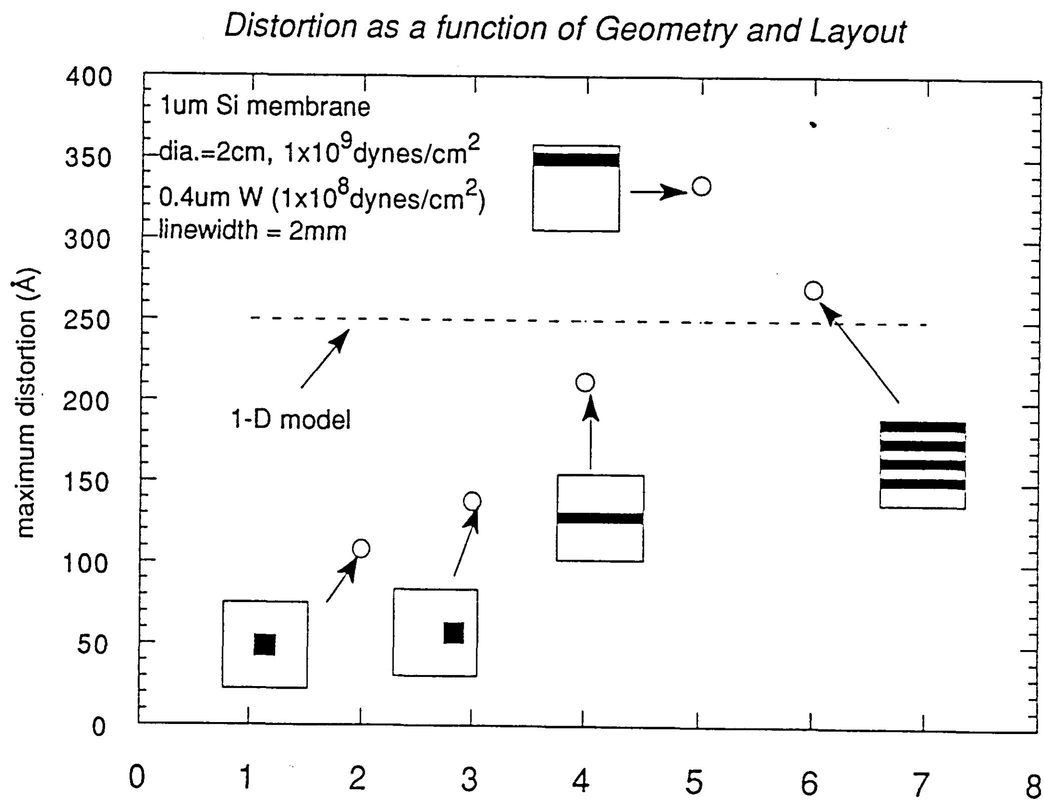

Figure 2.9. Plot of in-plane distortion for absorber pads (2x2mm in size) and absorber lines (2mm in width) located at different positions on the mask.

LOCALIZED TOPOGRAPHY MEASUREMENT
(LINNIK INTERFEROMETER)

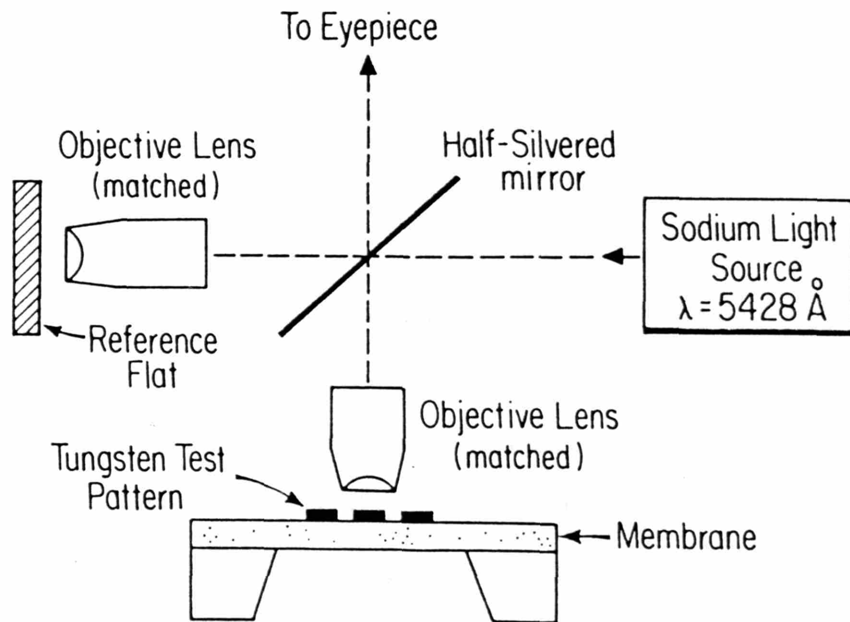

Figure 2.10. Schematic of the Linnik interferometer used to measured the out-of-plane distortion induced by absorber stress, and the interferogram taken at the absorber-membrane step edge.

$$\sigma_a = \frac{2\ \sigma_{s'}\ \eta_\infty}{t_a\ (1+\frac{t_a}{t_s})}$$

where σ_a is the absorber stress, $\sigma_{s'}$ is the membrane stress, η_∞ is the total out-of-plane deflection deflection, t_a is the absorber thickness, and t_s is the membrane thickness. The minimum detectable deflection is ~10nm, which corresponds to a minimum detectable absorber stress of ~5×10^7 dynes/cm^2 assuming an absorber thickness of 400nm, and a 1μm thick membrane of tensile stress 1×10^9 dynes/cm^2[1].

To further extend the accuracy of the OPD measurement, a digital interferometer can be used. A digital interferometer from WYCO corporation was used for this study. The measurement was done on a x-ray mask which consisted of 0.4 μm thick W absorber on 1 μm thick epi-Si membrane. Figure 2.11 shows the Linnik interferograms of the OPD measurement for a low stress W film, with an *estimated* total deflection of one-tenth of a fringe (~260Å). Figure 2.12 gives the WYCO measurement for the same low stress W film. Figure 2.12(a) shows a deflection of 8.4nm on the W side and Fig. 2.12(b) shows 2.81nm on the Si membrane side, which gives a total deflection of 112.5Å (less than 1/20 of a fringe, and the corresponding stress in the W film is 4×10^7 dynes/cm^2)! This is a remarkable results. By averaging over a reasonable area one can measure fringe deflection down to 10nm range which is not possible from the interferogram picture taken from the Linnik interferometer. Thus the WYCO digital interferometer is a powerful tool that can measure deflection down to 20Å or less using advance image processing capabilities. This can extend the accuracy of stress measurement down to the range of a few 10^6 dynes/cm^2.

2.3.2 IPD Measurement

In the previous section, an OPD measurement technique using Linnik interferometer was developed. Consequently, the absorber stress can be extracted from the OPD

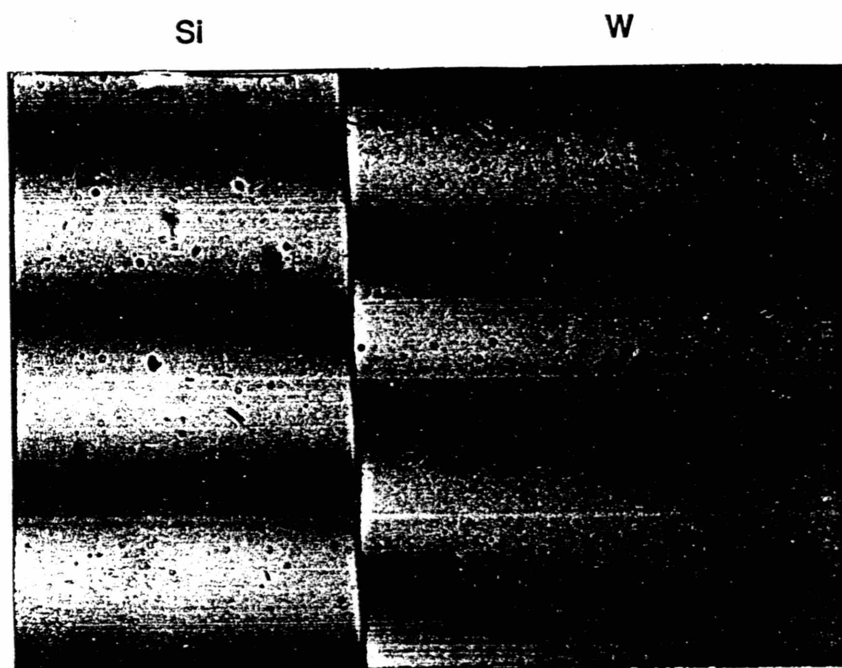

Figure 2.11. Linnik interferogram of the OPD measurement for a low stress tungsten film.

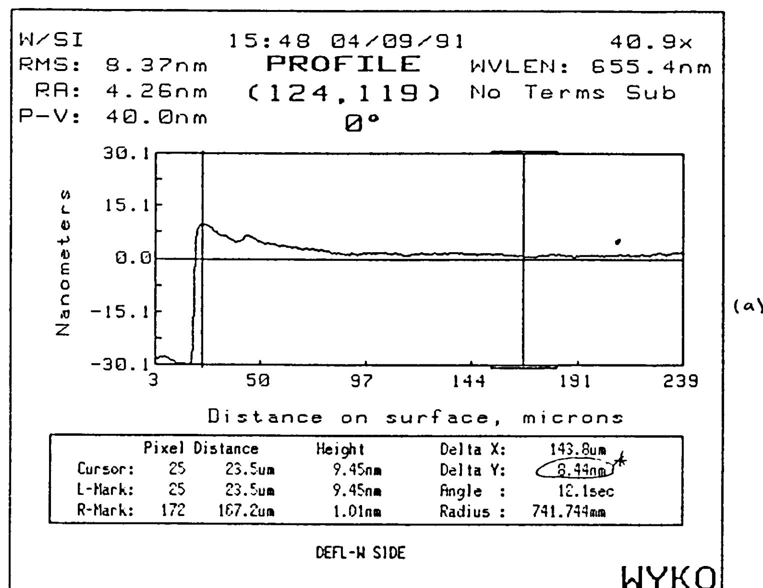

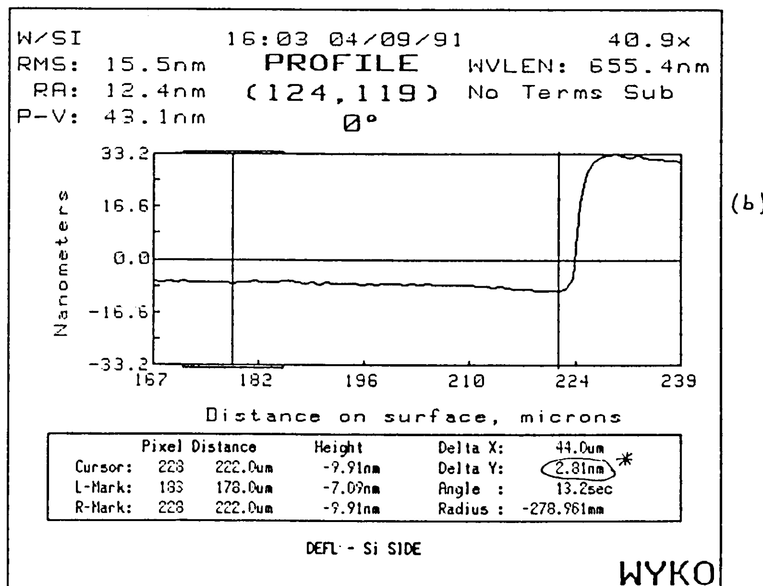

Figure 2.12. WYCO interferometer measurement at the membrane-absorber step edge for a low stress W film. (a) the deflection at the W side (8.4nm). (b) the deflection at the membrane side (2.81nm). The total deflection is 112.5Å. The corresponding W film stress is 4x10^7 dynes/cm^2.

measurement. Furthermore, another important information to be extracted from the absorber stress data is the in-plane distortion due to the absorber stress, since it will be one of the limiting factors for circuit overlay accuracy. Thus the next step would be correlating the OPD measurement to the IPD measurement, and hence correlating the relationship between the absorber stress and IPD. A large area IPD measurement method using moire technique was developed to address these issues.

The basis of the moire technique involves two sets of gratings superimposed at a small rotated angle on the front side of a membrane to form a moire fringe patterns. The resulting moire fringe patterns formed in the area of clear membrane and in the area of membrane covered with tungsten absorber will be oriented at an angle with respect to one another. This angle is a function of in-plane distortion introduced by the stress in tungsten absorber.

2.3.2.1 Distortion Interpretation and Analysis

In order to measure the IPD from the moire fringe patterns observed on the front side of the mask, a brief analysis of the formation of the moire fringe will be presented here.

Figure 2.13(a) depicts the vector diagram for the interpretation of the moire fringe pattern for an "ideal" distortion-free case. The vector **k** is defined so that its magnitude equals to the reciprocal of the periodicty of the grating, and it has a direction perpendicular to the lines of grating. In the diagram, vector $\mathbf{k_P}$ corresponds to the reference grid (of period P) formed on the membrane holographically. When the second grating (with the same periodicity P as the reference grating, and denoted by vector $\mathbf{k_P}'$) is holographically exposed on top of the reference grid at a small rotated angle, θ, a moire fringe pattern of period, M, is formed and it is represented by a vector $\mathbf{k_M}$.

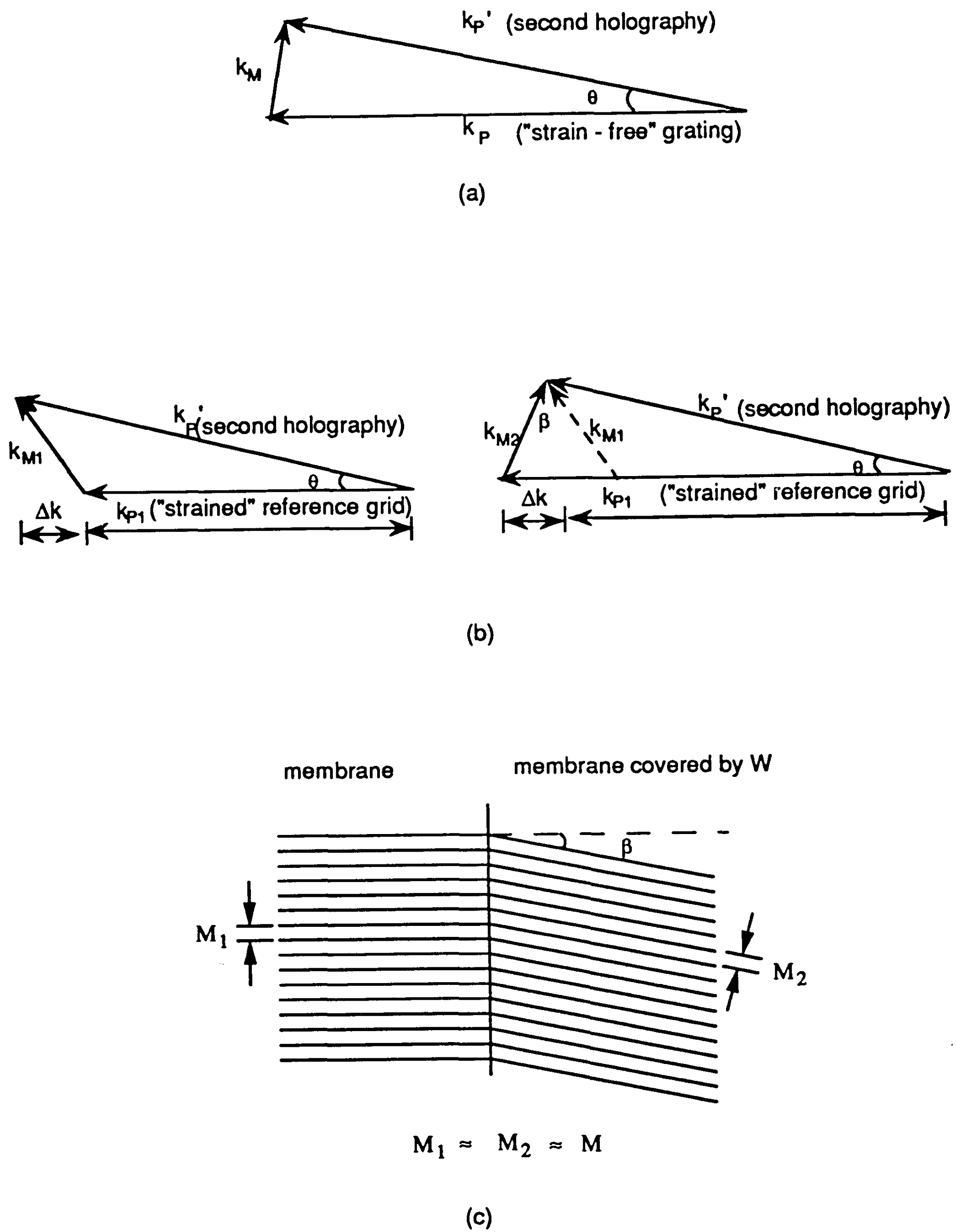

Figure 2.13. (a) Vector diagram representing distortion-free moire fringe patterns in k-space. (b) Vector diagram representing absorber induced distortion in the moire fringe patterns. (c) Illustration of moire fringe patterns expected on the front side of the membrane.

However when a tungsten absorber is deposited on the membrane, the stress in the absorber induces in-plane distortion and hence a change in the periodicity in the initial "distortion-free" reference grid. For a tensile stress tungsten film, the reference grid under the W absorber area will be "squeezed" and hence a smaller periodicity in the reference grid (increase in vector $\mathbf{k_P}$) is expected; the reference grid under the clear membrane area will be "stretched" and hence an increase in periodicty (decrease in vector $\mathbf{k_P}$) is expected. Figure 2.13(b) depicts the vector diagram for a tensile stress film deposited on the grid reference membrane. Vectors $\mathbf{k_{P1}}$ and $\mathbf{k_{P2}}$ represent the "strained" reference grids, of period P1 and P2, formed on the area of uncovered membrane and on the area of membrane coated with W absorber, respectively. The overlapping of the holographically exposed grating on top of the "strained" reference gratings in the membrane produced moire fringe patterns of period M1 and M2, and they are represented by vector $\mathbf{k_{M1}}$ and $\mathbf{k_{M2}}$, respectively. Physically, the distortion in reference grids, k_{P1} and k_{P2}, would be displayed as an angle difference, β, between the two moire fringe patterns in the two different areas as depicted in Fig. 2.13(c). This angle difference was also shown in Fig. 2.13(b) as the angle difference bewteen the two different directed vectors $\mathbf{k_{M1}}$ and $\mathbf{k_{M2}}$. For a small rotated angle, θ, and a small in-plane distortion, the difference in the moire fringe pattern periodicity (i.e. M1 and M2) is too small to be observed over the area of measurement. Therofore, only one moire fringe periodicty, M, is measured.

From the triangle shown in Fig. 2.13(b) the vector $\mathbf{k_M}$ can be determined from the following relationship:

$$k_M = k_P \sin\theta \qquad (22)$$

Since the angle θ is usually very small ($< 1^o$) and the final moire fringe patterns obtained on membrane areas with and without W absorber are almost the same (i.e. $M1 \approx M2 \approx M$), the angle, θ, can be approximated by:

$$\theta = \frac{P}{M} \qquad (23)$$

The deviation, Δk, represents the deviation from ideal vector k_P due to the stress in the W absorber. Here it was assumed that the reference grids over the area of the membrane and the area of membrane coated with tungsten was stretched or squeezed approximately by the same amount since the absorber coverage area is about 50% of the total mask area. Therefore Δk can be calculated to be:

$$\Delta k = k_P \sin\theta \tan\frac{\beta}{2} \qquad (24)$$

Once the change in the the k-vector space is known, k_{P1} and k_{P2} can be determined to be:

$$k_{P1} = k_P(\cos\theta - \sin\theta \tan\frac{\beta}{2})$$

$$k_{P2} = k_P(\cos\theta + \sin\theta \tan\frac{\beta}{2}) \qquad (25)$$

Typically the angle θ and β are small ($<1^o$), therefore using the small angle approximation, the corresponding periodicity of the "strained" gratings can be expressed in the form:

$$P1 = P\,(1 + \frac{\theta\beta}{2})$$

$$P2 = P\,(1 - \frac{\theta\beta}{2}) \qquad (26)$$

Figure 2.14 depicts the in-plane distortion of a tungsten absorber line and the corresponding in-plane distortion , δ, which is defined as :

$$\delta = \frac{L - L'}{2} \qquad (27)$$

where L is the "unstrained" absorber linewidth, and L' is the "strained" absorber linewidth. Using eq.(26) and the relationship that L'/L =P2/P, the IPD can be correlated to the change in the periodicity of the "strain" grating by the following equation:

$$IPD = \frac{\delta}{L} = \frac{\theta\beta}{4} \qquad (28)$$

Using this relationship, the IPD can be measured easily by simply measuring the angle β, and the moire fringe period (and hence angle θ).

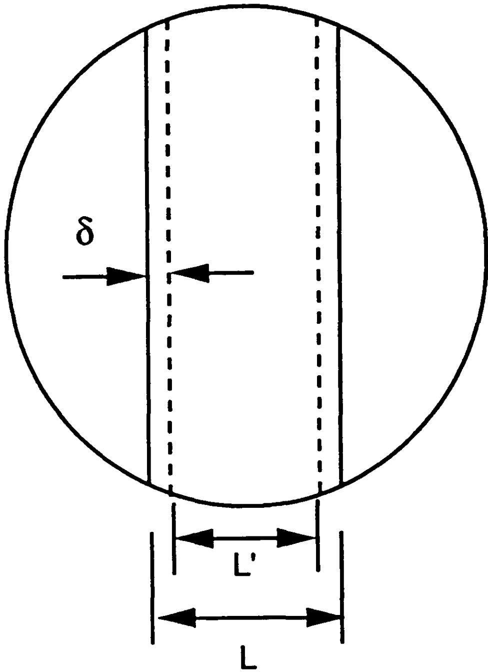

δ : maximum in-plane distortion

$$\frac{\delta}{L} = \frac{\theta \beta}{4}$$

Figure 2.14. Illustration of in-plane distortion (δ) in a x-ray mask.

2.3.2.2 Measurement Procedure

The first requirement for the IPD measurement required the fabrication of a distortion-free two-dimensional reference grid pre-etched into the membrane for future distortion measurement. Figure 2.15 depicts the sequence of this reference grid fabrication. The membrane was first spin coated with anti-reflection coating(ARC) and a thin layer of photoresist (~1900Å). It was then holographically exposed in two perpendicular direction to form a two-dimensional array of dots (200 nm period) as shown in Fig. 2.15. These dots were then shadow evaporated with Ni and reactive-ion-etched down through the ARC layer to the membrane using oxygen. At this stage CHF_3 gas was used to RIE into the membrane approximately 500Å deep to form the reference grid in the membrane. In both RIE processes, it was necessary to provide the backside cooling to the membrane due to the heating from the exposure to the plasma. The backside cooling was provided by coating the backside of the membrane with diffusion pump oil, and the etching was carried out 10 seconds at a time with 1 minute cooling in between the etching. This intermittent etching was necessary to prevent the melting of the resist lines.

Figure 2.16 depicts the sequence of the IPD measurement. A blank x-ray mask with a pre-etched 2000Å period reference grid, on the front side of the membrane,was first fabricated. After the reference grid fabrication, tungsten was sputtered on the backside of the membrane. Then the tungsten absorber was patterned to form the desired geometry (a centrally located line, of 1.1cm in width, stretched across the whole membrane was formed for this experiment). Following the patterning of W absorber, the front side of the membrane was re-coated with with a thin layer of photoresist (~1500Å). Finally it was re-exposed holographically with 2000Å period grating at a slightly shifted angle with respect to the pre-etched grids on the membrane. At this stage the resulting moire patterns formed on the front side of the membrane is ready for the IPD measurement.

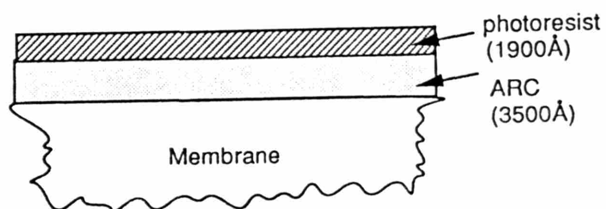

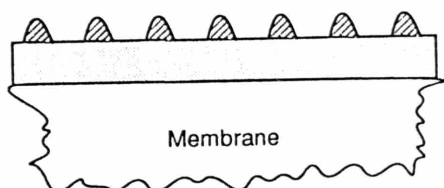

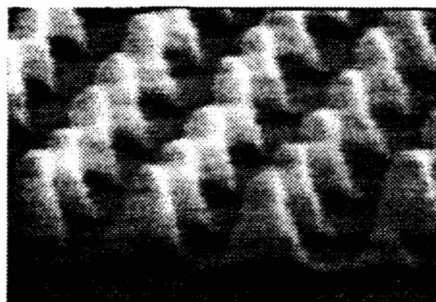

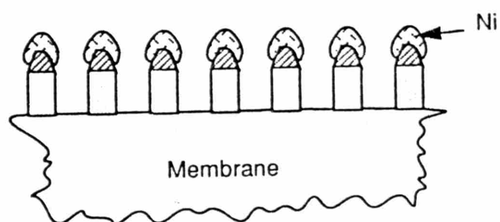

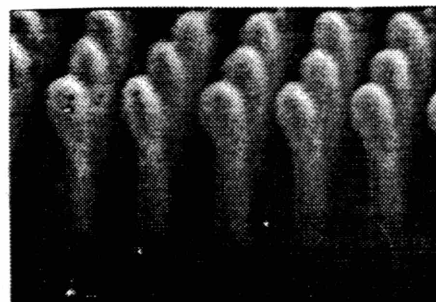

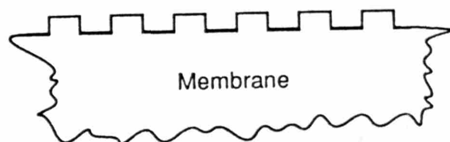

Figure 2.15. Fabrication procedures for grid reference membrane for in-plane distortion measurement.

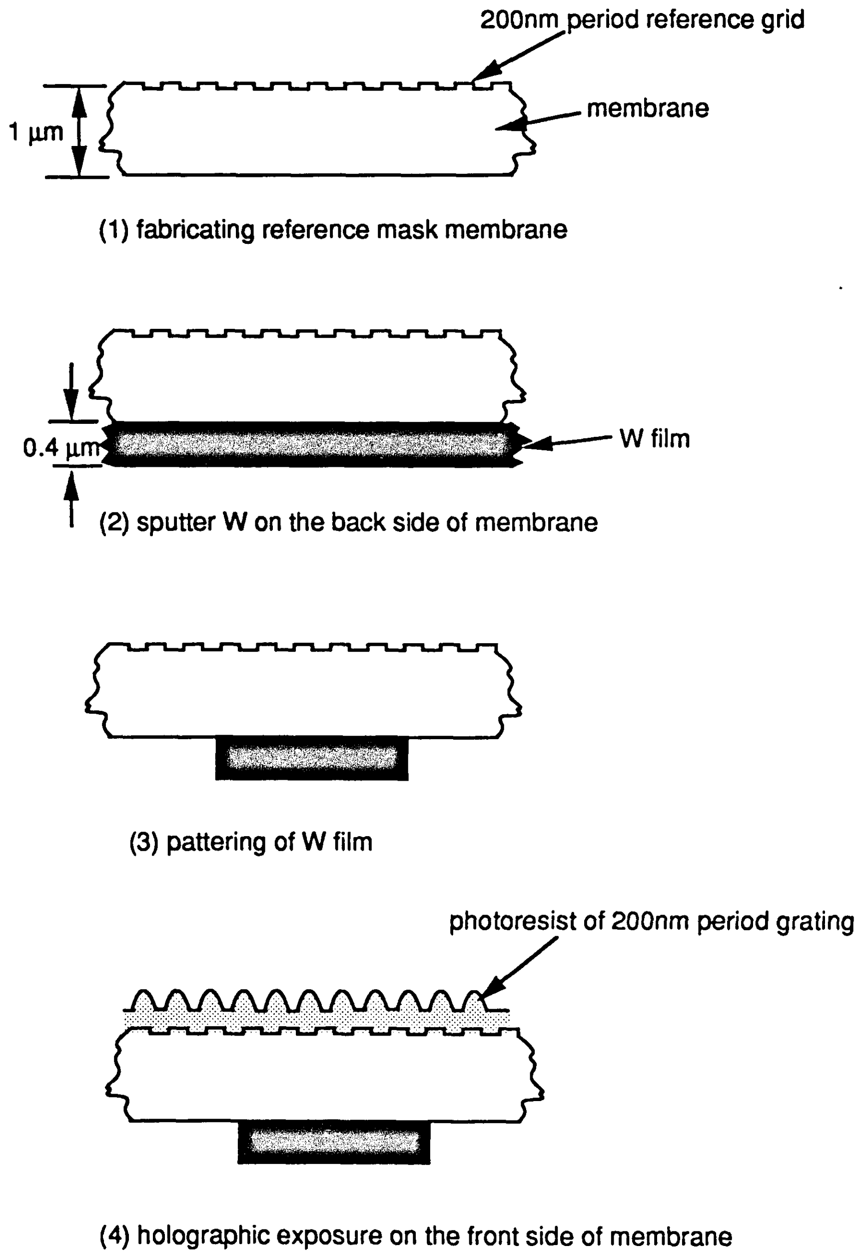

Figure 2.16. Illustration for in-plane distortion measurement sequence.

2.3.2.3 Experimental Results

A sputtering run was carried out to correlate the IPD measurement with OPD measurement. Figure 2.17(a) shows the moire fringe obtained on the front side of a epi-Si membrane, 1μm thick and 2.3cm in diameter, coated with 0.4μm thick tungsten lines (1.1cm in width) that stretches across the whole membrane. The moire fringe periodicity, M, is 44.5μm, and the measured angle β is approximately 2.5±0.2° (4.4±0.3 x10^{-2} rad). The corresponding angle, θ, between the two holographic exposures can be calculated from eq.(23) to be 0.25° (4.5x10^{-3} rad). Therefore the resulting in-plane distortion is:

$$IPD = \frac{\delta}{L} = \frac{\theta\beta}{4} = \frac{49}{10^6} \quad \text{for } (\beta = 2.5^o) \qquad (29)$$

The Linnik interferogram at the membrane-absorber step edge was shown in Fig. 2.17(b). The OPD measured form the picture is approximately 131nm, which corresponds to a stress of 4.7x10^8 dynes/cm^2. This stress would produce an IPD, $\frac{\delta}{L}$, of $\frac{42}{10^6}$ based on the prediction of eq.(21). Furthermore an FEM simulation was also used and the corresponding IPD was calculated to be $\frac{40}{10^6}$. In all three cases, the IPD moire measurement, the OPD Linnik measurement, and FEM simulation all shows consistent agreement. Thus the moire technique provides a powerful tool to examine and to correlate the IPD measurement with OPD measurement.

The main improvement that can be made to increases the accuracy of this technique is to enhance the ability to resolve the angle (β) between the two moire fringe patterns over the area of membrane and the area coated with tungsten, and the ability to control angle θ. Using a CCD camera and further image processing, and with better control of the

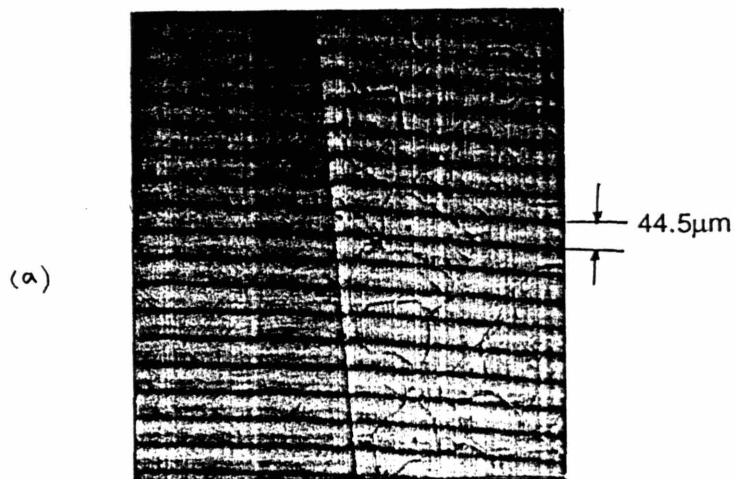

Moire fringe pattern for in-plane distortion measurement

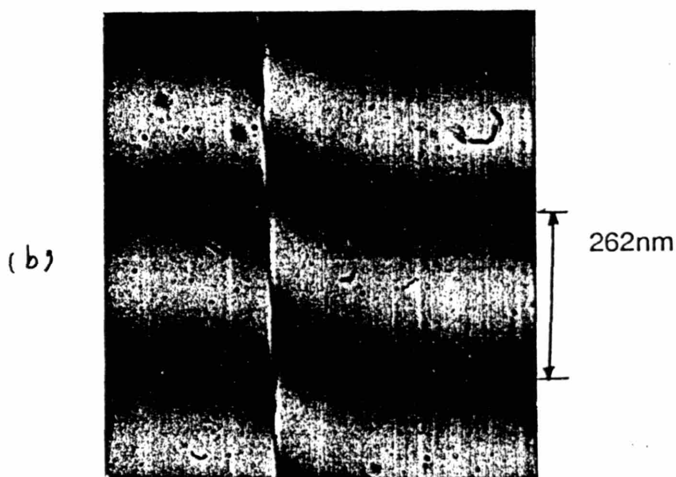

Linnik interferogram at W - membrane step edge

Figure 2.17. (a) Photograph of moire fringe patterns obtained on the front side of the membrane. (b) Linnik interferogram of the OPD measurement at the backside of the membrane.

holographic exposure angles, IPD measurement down to one part per million should be possible!

Chapter 3

Low Stress Tungsten Sputtering

There are extensive efforts around the world to develope the technology to sputter low stress tungsten [9-13], and to understand the physics of the formation of high stress tungsten film. Figure 1.3 shows a typical plot of the dependence of stress on sputtering pressure. The stress of the tungsten film varied from highly compressive at low sputtering pressure to highly tensile at higher sputtering pressure. Although the exact shape of the curve depends on the power density and geometry of the sputtering system used, the general form is the same for most sputtered W film. The formation of a tensile stress film is usually explained by the interatomic attractive forces between the columnar grain boundaries in the W film[7-8]. The compressive stress is usually explained by the peening action of high energy sputtered atoms and neutrals reflected from sputtering target [7-8]. Therefore the low stress tungsten can be obtained by a delicate balance of these two effects.

In addition to the existence of two highly stressed regimes in the sputtering curve, there are additional stability issues to be considered for the W film. It is experimentally determined that there are two phases of W film that can be formed in the sputtering process. One form of structure is the α-phase W film which has a bcc crystal structure, and has a x-

ray diffraction profile shown in Fig.3.1. This is the desirable form of W film that is believed to be stable and therefore no change in the film structure and hence no change in the film stress is expected. The β-phase W film, is an A_3B compound with an A-15 crystal structure, has a x-ray diffraction profile shown in Fig. 3.2. It is metastable and it will undergo structural changes to the α-phase, and hence change the film stress. Thus, β-W is the undesirable form of W film for the x-ray mask absorber.

3.1 Sputtering of Stable α-W

Experiments were designed to deposit low stress stable α-phase W film. Three different Si wafer substrate were prepared for the sputtering experiments. These three substrates were plain Si wafers, Si wafers coated with 5nm of evaporated Cr, and Si wafers coated with 5nm of Cr followed by 10nm of evaporated α-W, so called "seed layer". Then sputtering runs were performed at room temperature and at an elevated substrate temperature of 200°C over a sputtering pressure ranged from 5mtorr to 25mtorr. The crystal structure of the sputtered W films was then examined by x-ray diffraction. It was found from the x-ray diffraction studies that only α-W was obtained over the entire sputtering pressure range (i.e. 5-25 mtorr), when sputtering runs were carried out at an elevated temperature of 200°C on substrates coated with seed layer. The other two substrates showed β-W formation at some sputtering pressure regions. Therefore more sputtering runs were carried out to determine if the seed layer process (using evaporated Cr and W) is repeatable in obtaining α-W from run to run. Over a 12 months period, 20 sputtering runs were performed and the phases of the sputtered films were checked using x-ray diffraction. It was found that α-W film was consistently obtained when sputtering

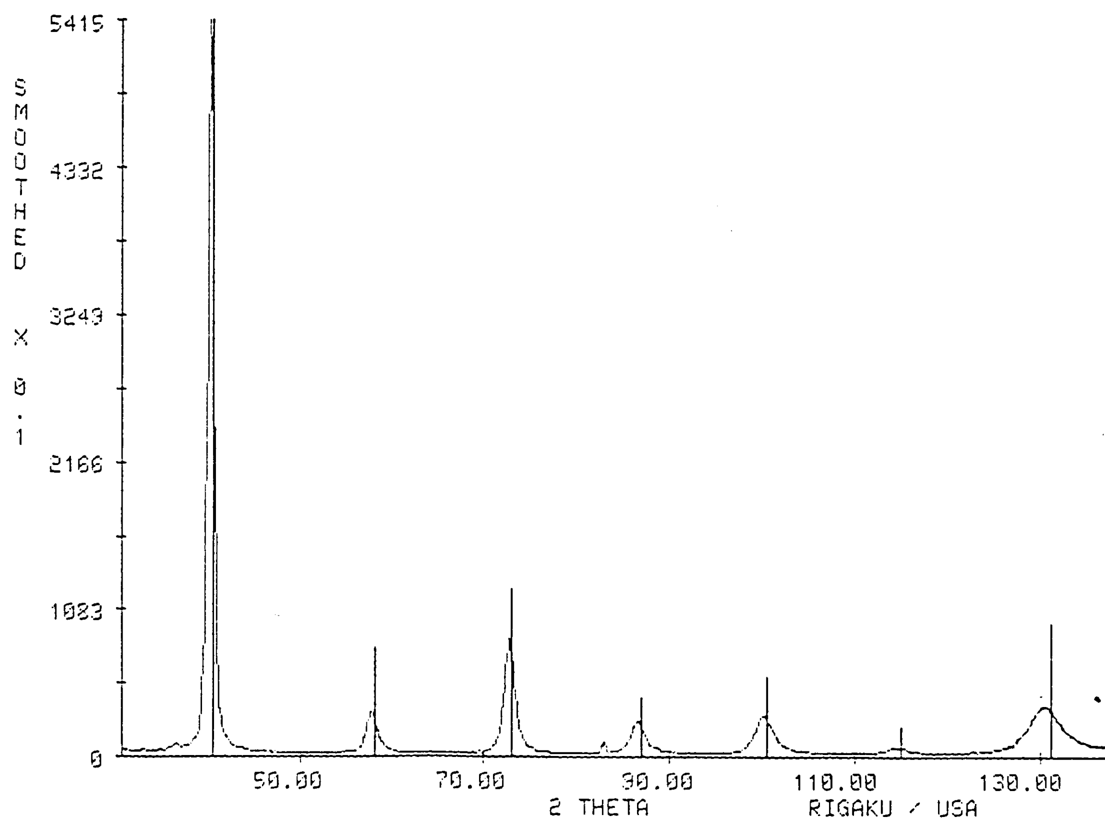

Figure 3.1. X-ray diffraction of α-phase W film.

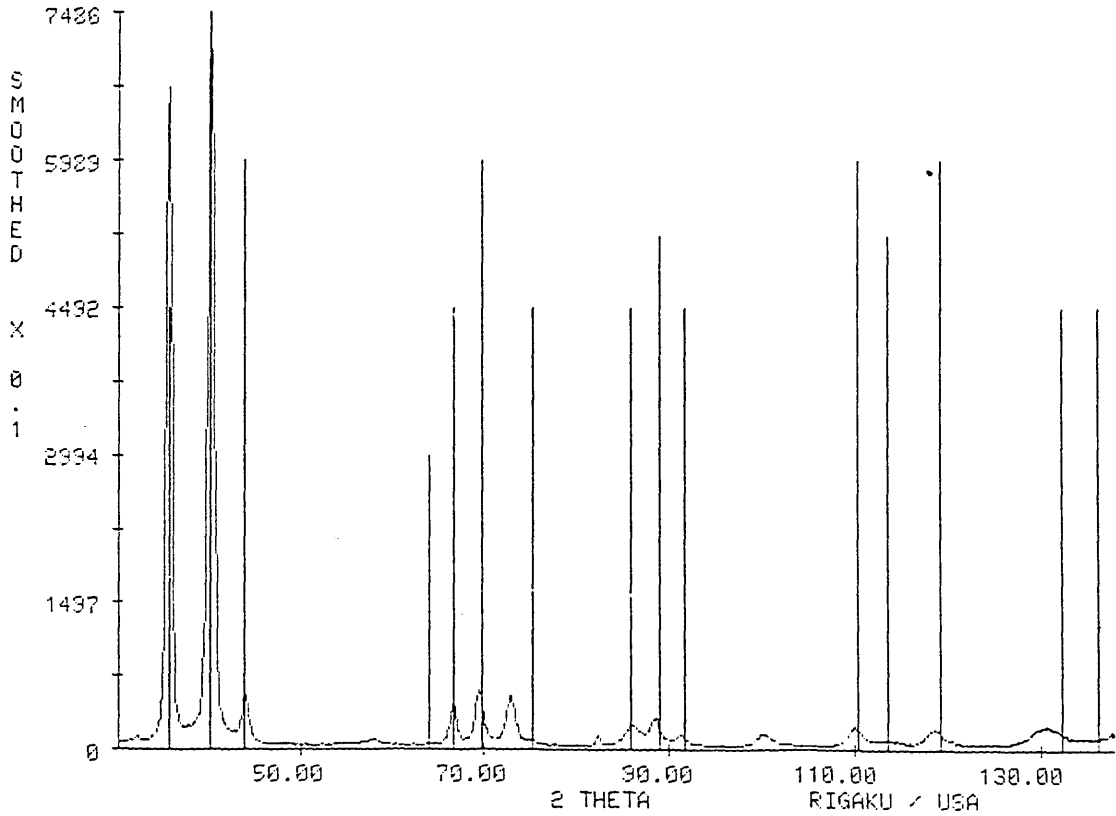

Figure 3.2. X-ray diffraction of β-phase W film.

runs were carried out at an elevated temperature of 200°C and on substrates coated with Cr-W seed layer.

3.2 Open Loop Process

One of the main difficulties in applying W as the absorber materials is the stress control of sputtered W film. Using the "seed layer" recipe for depositing stable α-W, a series of sputtering runs were carried out at an elevated temperature of 200°C and at 1.1Watts/cm^2. This gave a deposition rate of approximately 200Å per minute. Figure 3.3 shows the stress of W film of thickness 400 nm sputtered over a small sputtering pressure range (16-17 mtorr) using a MRC 8620 sputtering system. Note the sharp change of the film stress from highly compressive to highly tensile over a small sputtering pressure range. Therefore in order to sputter W film with stress less than or equal to 1×10^8 dynes/cm^2 it is required to control the pressure to within 0.013 Pa (0.05 mtorr) of the zero-stress pressure. A mass flow controller was installed on the sputtering system to control the pressure to within 0.013 Pa, which is within the requirements. In addition, a throttle valve feed-back controller was also installed to control the pressure within 0.013 Pa. Variables such as substrate temperature, substrate material type, pressure, sputtering power density, and target to substrate distance all have to be well controlled and optimized to deposit a zero stress film and achieving a repeatable process. Once a zero stress point was determined for a particular substrate type from a series of sputtering runs, zero stress W can be repeatable sputtered under the same condition, onto the same substrate, as shown Figure 3.4. This process is called "open-loop" process since it must be calibrated for each substrate type, and the stress is measured only after a run, not during it. In-situ monitoring would , of course, be preferred.

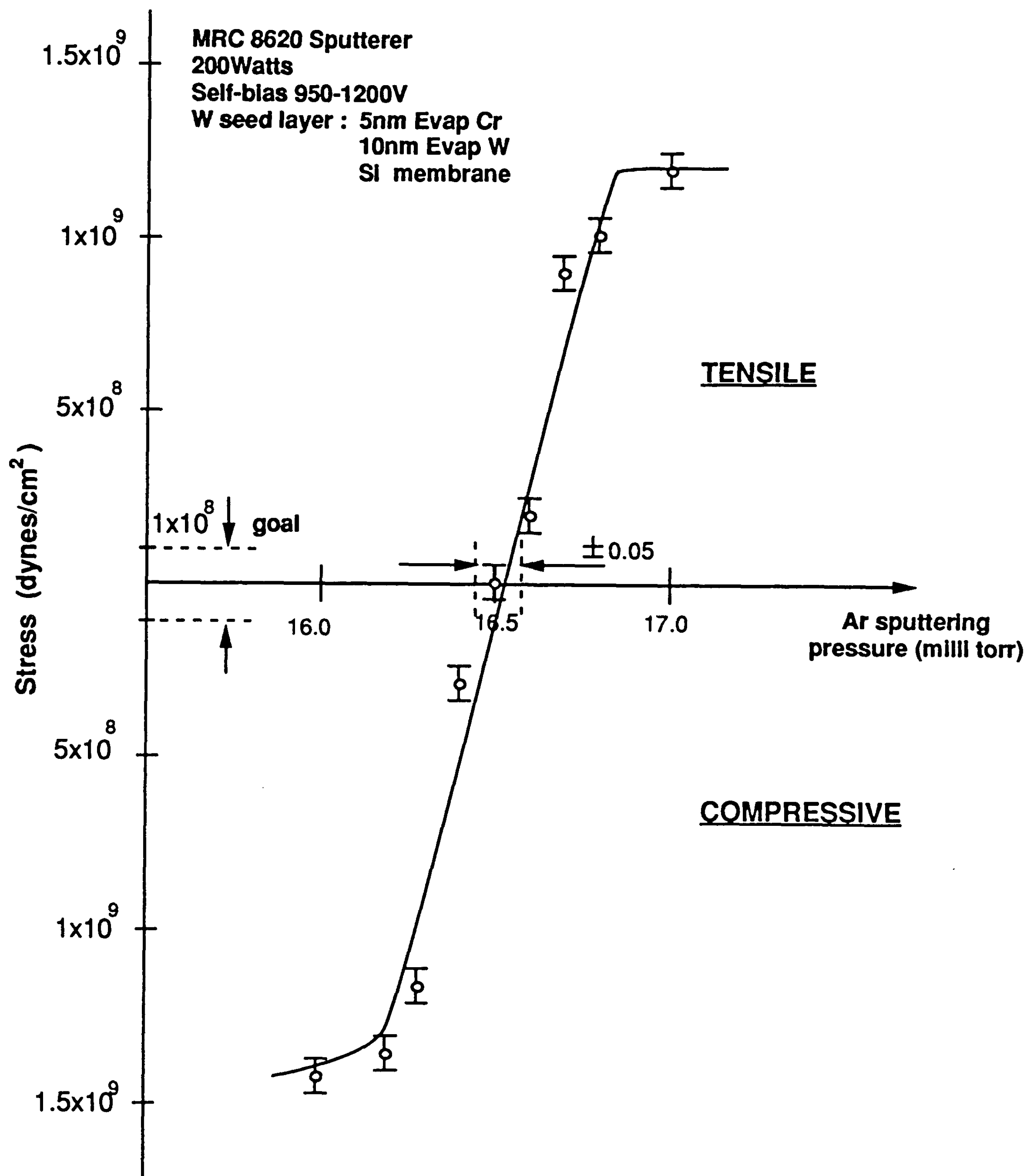

Figure 3.3. W film stress versus sputtering pressure over a narrow range of 16-17 mtorr.

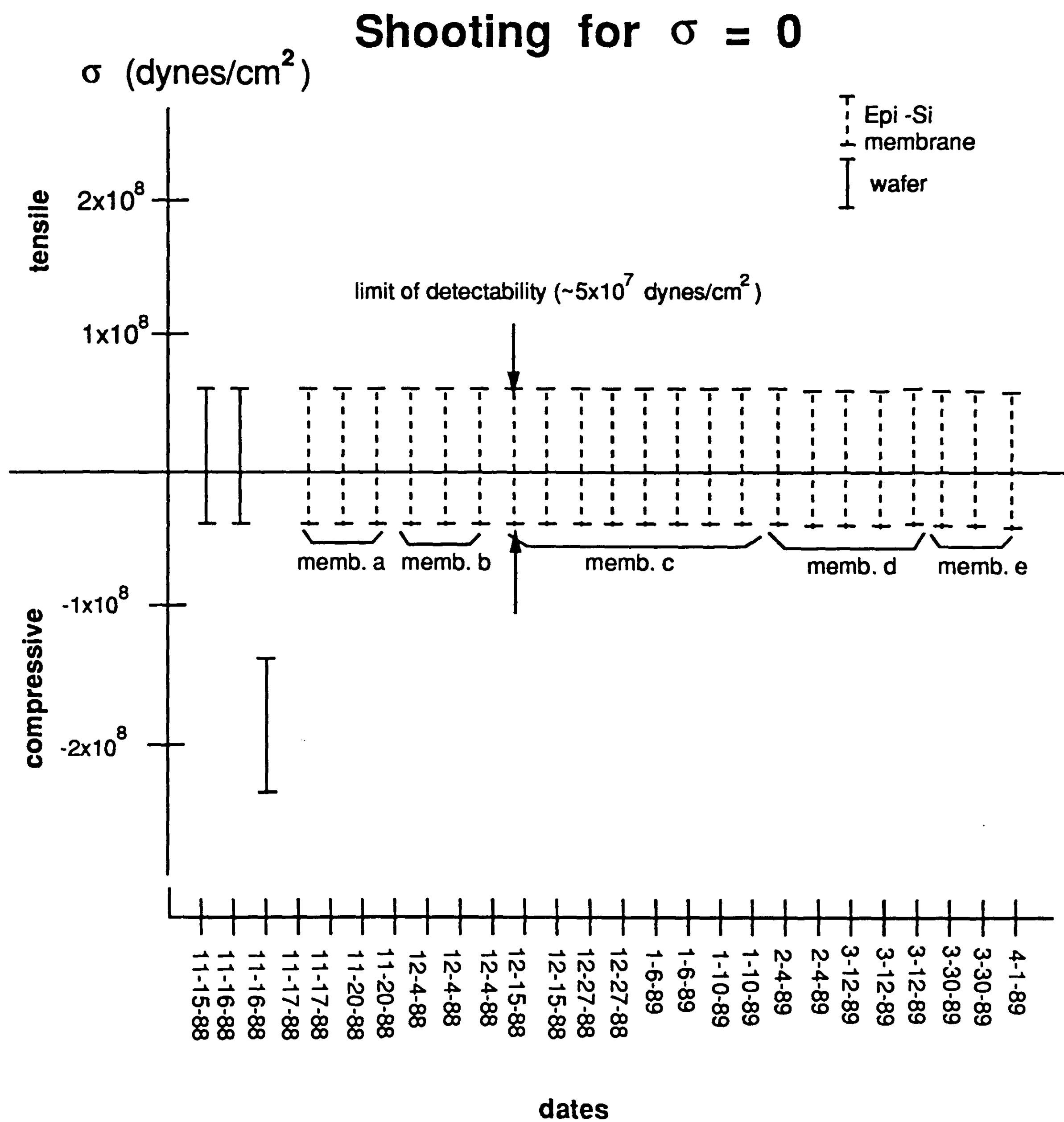

Figure 3.4. Diagram depicting the repeatability of sputtering zero-stress tungsten.

3.3 Thermal and Radiation Stability

The stability of the α-phase was examined by high vacuum high temperature annealing. These experiments were carried out at a base pressure of 10^{-6} or 10^{-7} torr and at a temperature of 200°C and 470°C, respectively. As expected, the α-W did not show any change in the crystal structure nor does it show any change in stress after 50 hours (at 200°C) and 24 hours (at 470°C) of annealing at the elevated temperatures. However for the β-W changes in stress towards tensile region was observed. In addition, W sputtered on the Si and SiN_x membranes were examined with the co-operation with AT&T Laboratory [10]. X-ray diffraction studies were performed to examine the structure of the W film sputtered on these membranes. It was found that α-W was formed on the membrane with and without the seed layer when the W was sputtered at an elevated temperature of 200°C and at a fixed sputtering pressure (~17 mtorr). Furthermore, it has been shown in Bell Lab[10] that 100% α-W film can be obtained by sputtered W at an elevated temperature of 200°C with a low system base pressure, good system cleanliness, and high purity target and gases.

As a final examination of the W stability, x-ray radiation stability were studied. α-W film of thickness 400nm were sputtered on a epitaxial-Si membrane (1μm thick) at an elevated temperature of 200°C. The film was then patterned with a cross as shown in Fig. 3.5. The film had an initial stress of zero ($<5\times10^7$ dynes/cm^2) as indicated by the flat fringes taken with the Linnik interferometer. This zero stress W film was then sent to the

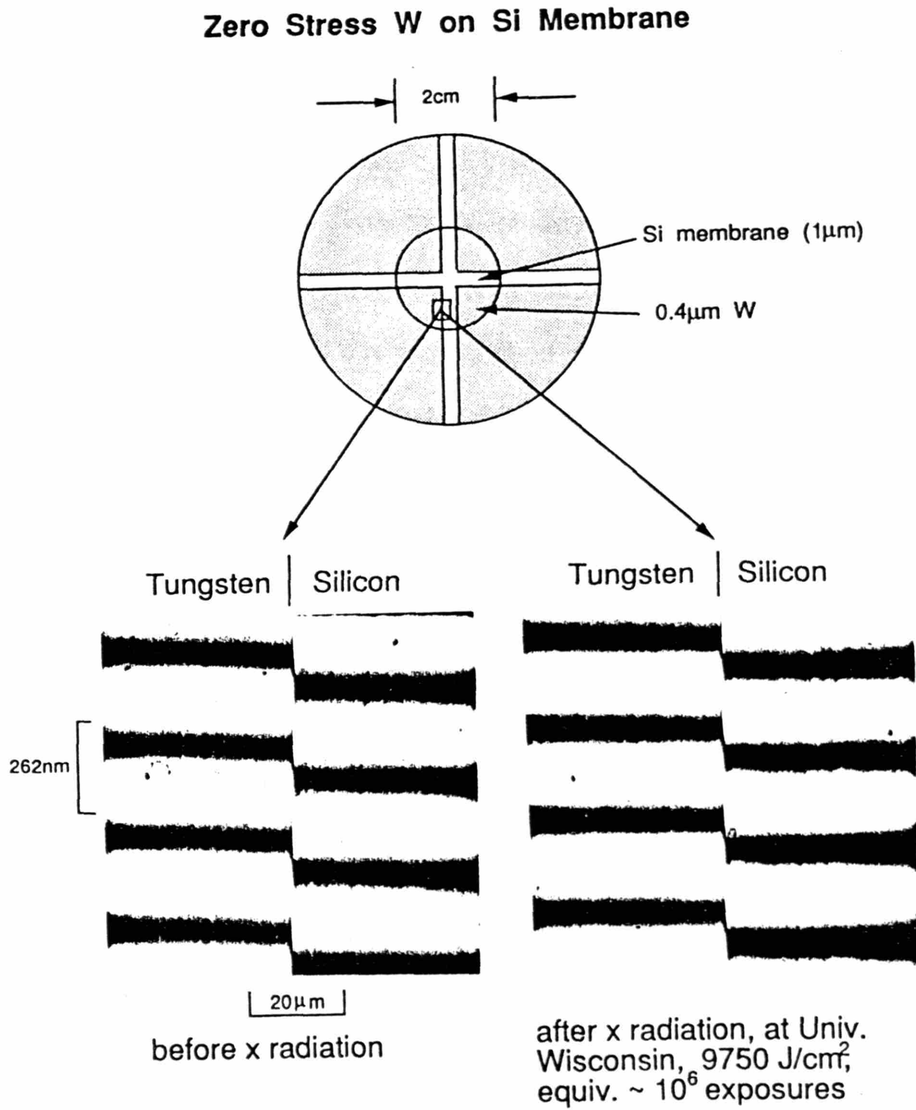

Figure 3.5. Linnik interferograms at the W-membrane step edge before and after the exposure to heavy x-ray radiation of ~9800 J/cm^2.

University of Wisconsin for high dose radiation test. After it was exposed to x irradiation for 38.5 hours using a 0.8GeV beam (incident dose of 1650 J/cm^2), and for 37.75 hours using a 1GeV beam (incident dose 8150 J/cm^2), no change in stress was detectable in the Linnik interferometer. Since no change in stress was expected from the epitaxial-Si membrane, therefore any change in the fringe curvature would be from the change in the W-film stress. Since no changes in the fringe curvature was observed after the high dose of radiation as shown in Fig. 3.5. This indicates the radiation stability of the α-W film. Figure 3.6 shows the interferogram taken from the back surface of the Si membrane, opposite the W pattern. Clearly there is no deflection of the membrane due to W. The total x-ray dose is ~9800 J/cm2. At a wavelength of 1.4nm, which is compatible with the mask configuration (i.e., 1μm thick Si, 400nm W) a resist sensitivity of 9.8 mJ/cm^2 appears feasible. Thus the dose the mask received is equivalent to between 10^5 and 10^6 x-ray lithography exposures.

3.4 Stress Uniformity

Another issue regarding the sputtering of tungsten film on a x-ray mask membrane is the stress uniformity over the entire mask area. Sputtering runs were carried out on various types of membrane, and tungsten film was sputtered at both room temperature and at an elevated temperature of 200°C. It was found that during the sputtering process, when the membrane is exposed to the plasma, additional heating from the plasma introduces a temperature gradient in the membrane. To examine the effect of the stress variation within the membrane area due to the temperature gradient, a tungsten step edge was etched after the sputtering run was completed, and the OPD was measured using the Linnik interferometer. Figure 3.7 shows the measured OPD, and the corresponding stress, versus

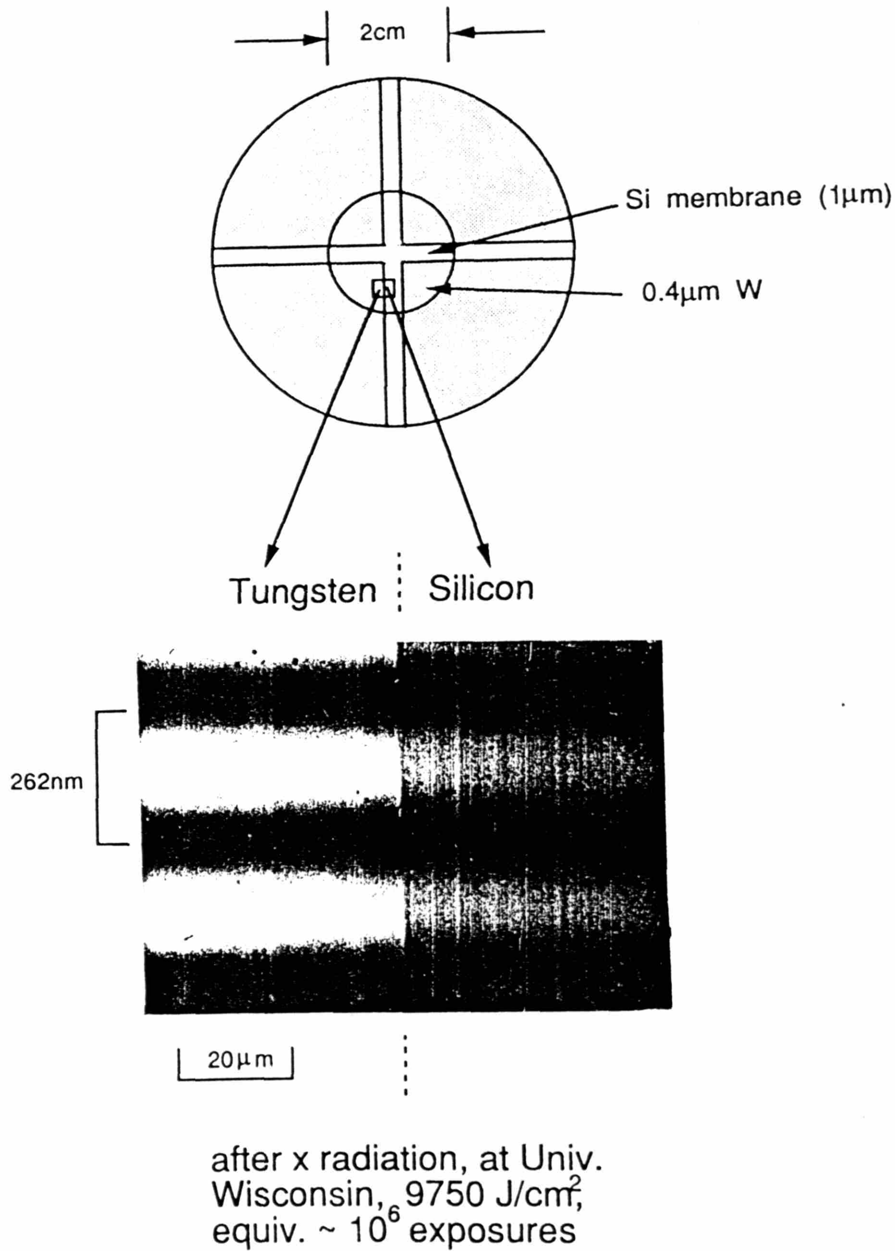

Figure 3.6. Linnik interferogram of the W absorber-membrane step edge taken on the backside of the membrane after the exposure to x-ray radiation of 9750 J/cm^2.

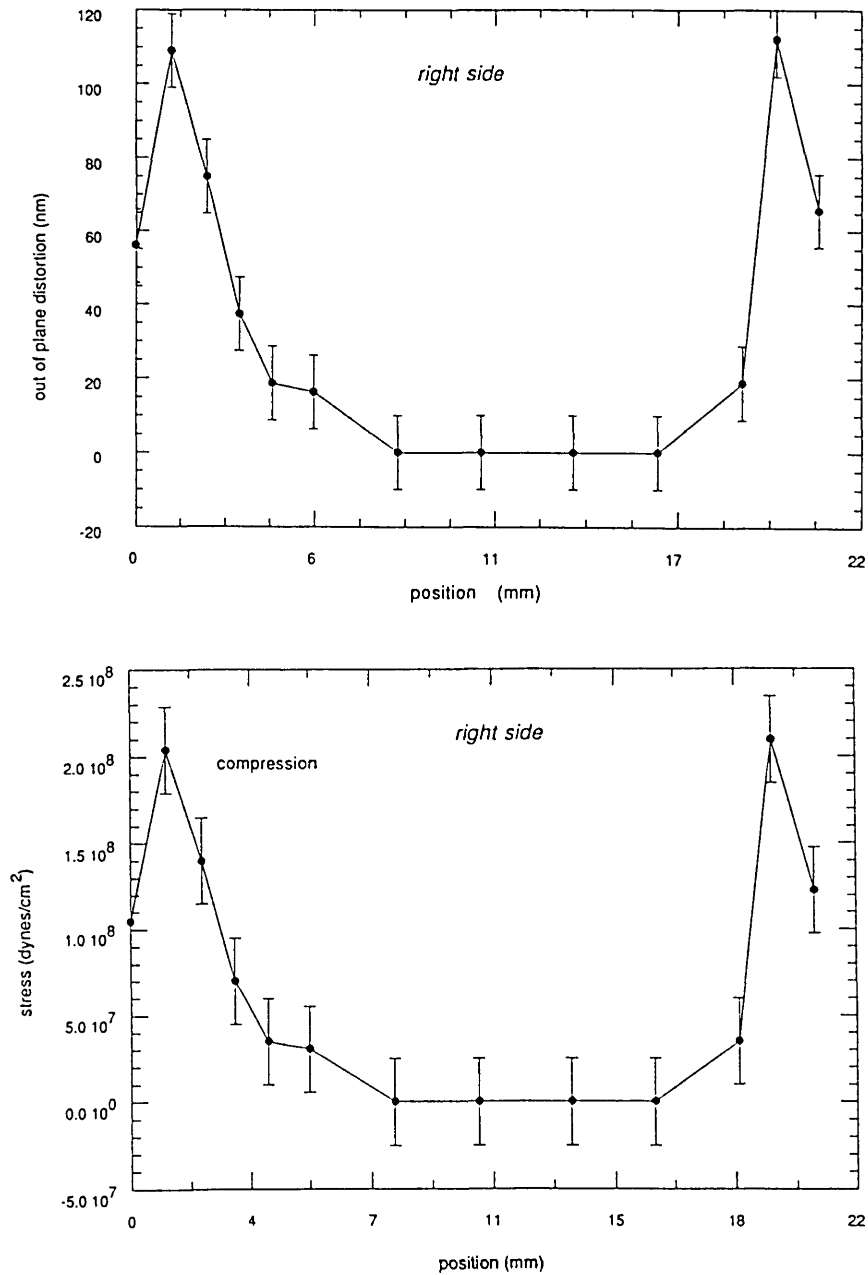

Figure 3.7. Mapping of the OPD measured using Linnik interferometer and the corresponding absorber stress across the whole membrane.

the W step edge position on the membrane for a B-doped Si membrane sputtered at room temperature. As shown in Fig. 3.7 a compressive W film was observed at the edge of the membrane, and a zero stress W film (i.e. $< 5 \times 10^7$ dynes/cm^2) was observed for most of the area along the W step-edge except near the boundary of the membrane. For room temperature deposition when the membrane was exposed to the plasma during the sputtering process, membrane was heated up quickly to some high temperature due to its small heat capacity. The boundary area of the membrane has a closer contact to a large thermal capacity of the substrate and thus better rate of heat transfer, resulting in a cooler boundary area than most of the central area of the membrane. After the sputtering run was completed, both the membrane and the sputtered W film were cooled to room temperature and the magnitude of this change in the thermal stress is given by:

$$\sigma_{th} = (\alpha_w - \alpha_{mem}) \Delta T_{th} E_w \quad (30)$$

where σ_{th} is the thermal stress change, α_{mem} and α_w are the thermal expansion coefficients for the membrane and W film, respectively, ΔT_{th} is the deposition temperature minus the temperature at which stress is measured, and E_w is the Young's Modulus of the sputtered W film. However due to the existence of temperature gradient in the membrane during the deposition process, the central area of the W film on the membrane will go through higher thermal stress change than the W film near the boundary of the membrane. As a result, a more compressive film at the edge of the membrane was expected.

Sputtering runs were also carried out at an elevated temperature of 200°C to check for the stress uniformity. In this experiment, the additional heating provided prior to the sputtering process should help to reduce the temperature gradient in the membrane area, and thus a smaller stress variation should be expected. Fig. 3.8 shows the interferogram of the W-membrane step edge taken at the center of the membrane and at the edge of the membrane. From both pictures, no detectable change in the fringe curvature was observed. Further experiments for both Si membrane and SiNx membrane were carried out, and in

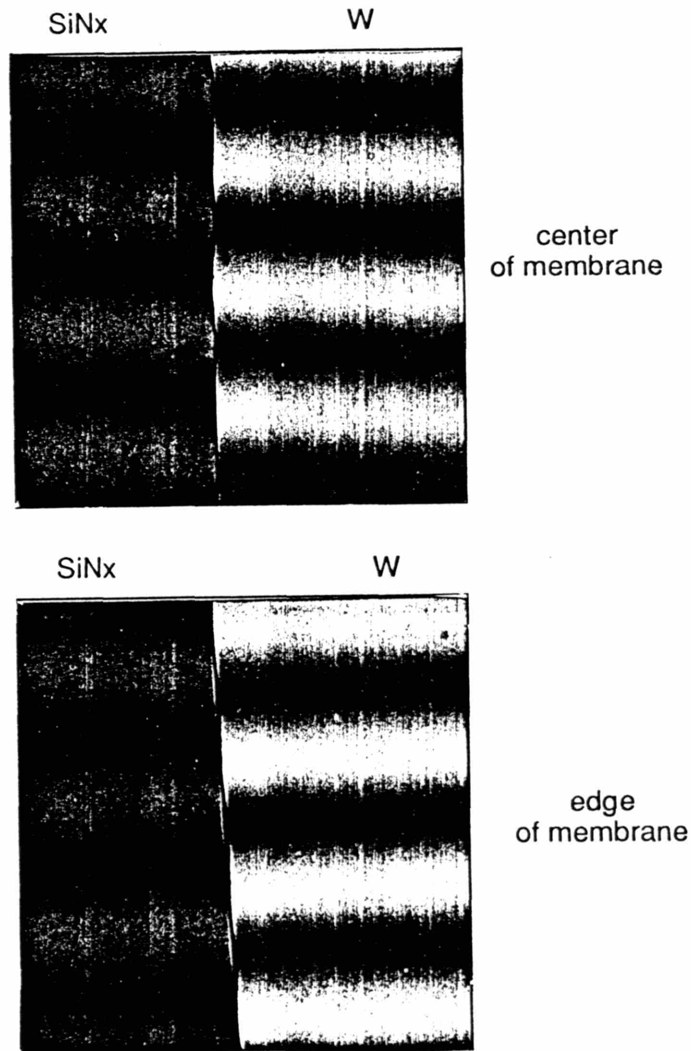

Figure 3.8. Linnik interferograms taken at the center and at the edge of the membrane for W sputtered at an elevated temperature of 200°C.

both cases uniform zero stress (< 5×10^7 dynes/cm^2) W film were observed throughout the area of the membrane. Thus for better stress uniformity and better film stability it is desirable to carry out the sputtering process at an elevated temperature.

Chapter 4

In-situ Stress Monitoring

In the previous section, a zero-stress tungsten (i.e. below the level of detectability in a Linnik interferometer, i.e. below $5x10^7$ dynes/cm^2) deposition process has been described, and the repeatability of getting the zero stress tungsten using this process was also assured. However using this "open-loop" process, the resulting zero stress film cannot be assured until after the deposition is completed and the W film stress is measured directly from the membrane-absorber step edge using the Linnik interferometer. Therefore a process based on the resonant frequency of the membrane, to monitor the stress during the sputtering process was developed. Ultimately this should lead to a closed-loop, automatic, computer control of stress of sputtered film.

The technique of monitoring the membrane resonant frequency was chosen because in a vacuum environment, without atmospheric damping, membrane exhibits extremely high Q [29] and thus a high degree of accuracy in measuring the resonant frequency can be achieved. Since the resonant frequency of a membrane is a direct function of the membrane

stress, it implies that a high degree of accuracy in the stress measurement can also be achieved.

4.1 Basic Membrane Theory

For a single-layer, homogeneous membrane under a uniform biaxial stress, σ, the fundamental resonant frequency of a circular membrane (in Hz) is given by[30-31]:

$$f_{res} = \frac{1}{2.61r} \sqrt{\frac{\sigma}{\rho}} \qquad (31)$$

where r is the radius and ρ is the density of the membrane. This formula assumes small amplitude vibration. For a membrane consisting of several layers of materials, each with thickness t_i, and stress σ_i, eq(32) can be used to define the effective tension per unit length T_{eff} as the sum of the individual tension of each layer:

$$T_{eff} = \sum_i \sigma_i t_i \qquad (32)$$

In the case of a W film deposited onto a homogeneous membrane, the resonant frequency of this composite structure becomes:

$$f_c = \frac{1}{2.61r} \sqrt{\frac{\sigma_m t_m + \sigma_f t_f}{\rho_m t_m + \rho_f t_f}} \qquad (33)$$

where t_m and t_f are the membrane and film thickness, ρ_m and ρ_f are the membrane and film densities, and σ_m and σ_f are the membrane and film stress. According to eq. (33), the stress of the absorber film can be extracted by independently measuring the resonant frequency of the membrane and the thickness of the deposited film. In practice, eq. (33) cannot be used to calculate exactly the resonant frequency because during the sputtering the temperature of the membrane and the temperature gradient between the membrane and the supporting substrate are not know. Also there may be several other factors that affect f_c

which are unknown at this point. Nevertheless, it was believed that the functional dependence of the resonant frequency on film thickness and stress given in eq. (33) is essentially correct and can be used in semiempirical way to monitor and control the stress.

4.2 In-situ Stress Monitoring System Set-up

Figure 4.1 shows the essential elements of the experimental set-up. The mask substrate is held firmly against the stage, which also holds a thin-film thickness monitor beside the substrate. The membrane is driven into vibration using a 20 V peak-to-peak sine wave with a 10 V offset applied to a concentric ring capacitor plate underneath the membrane. The membrane oscillation is detected by means of a fiber optic sensor, MTI-100 Fotonic Sensor. To increase the signal strength, the side of the membrane facing the optical fiber sensor is coated with ~10nm of Al. The sensor is brought within 100 μm of the membrane by means of a special holder. Resonant frequency is determined by sweeping the signal generator and finding the frequency at which the membrane vibration is at a maximum. Because of the very high Q of the membrane, it takes some time for the membrane to reach maximum deflection when stimulated at the resonant frequency. For this reason, the resonant frequency is found by comparing the results of the sweeping up in frequency and down in frequency as shown in Fig. 4.2. (G. L. Miller, et al of AT&T Bell Labs have developed a circuit that tracks the membrane resonance without the need for sweeping) The resonant frequency of this pair of sweeps is approximately 5.97 kHz with a bandwidth of ~ 2.5 Hz, which corresponds to a Q of 2400. The sub-harmonic at ~2983 Hz is also visible.

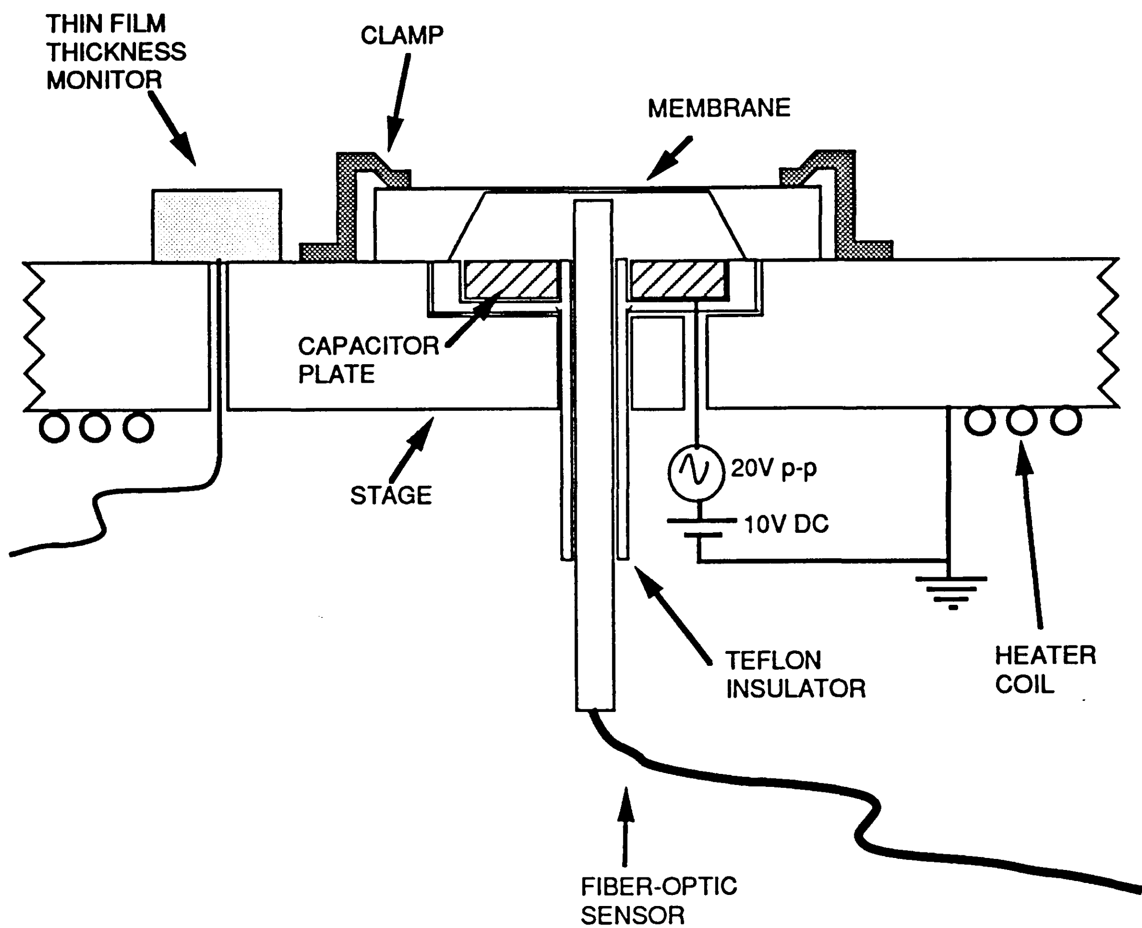

Figure 4.1. Schematic of the holder stage for in-situ monitoring of resonant frequency

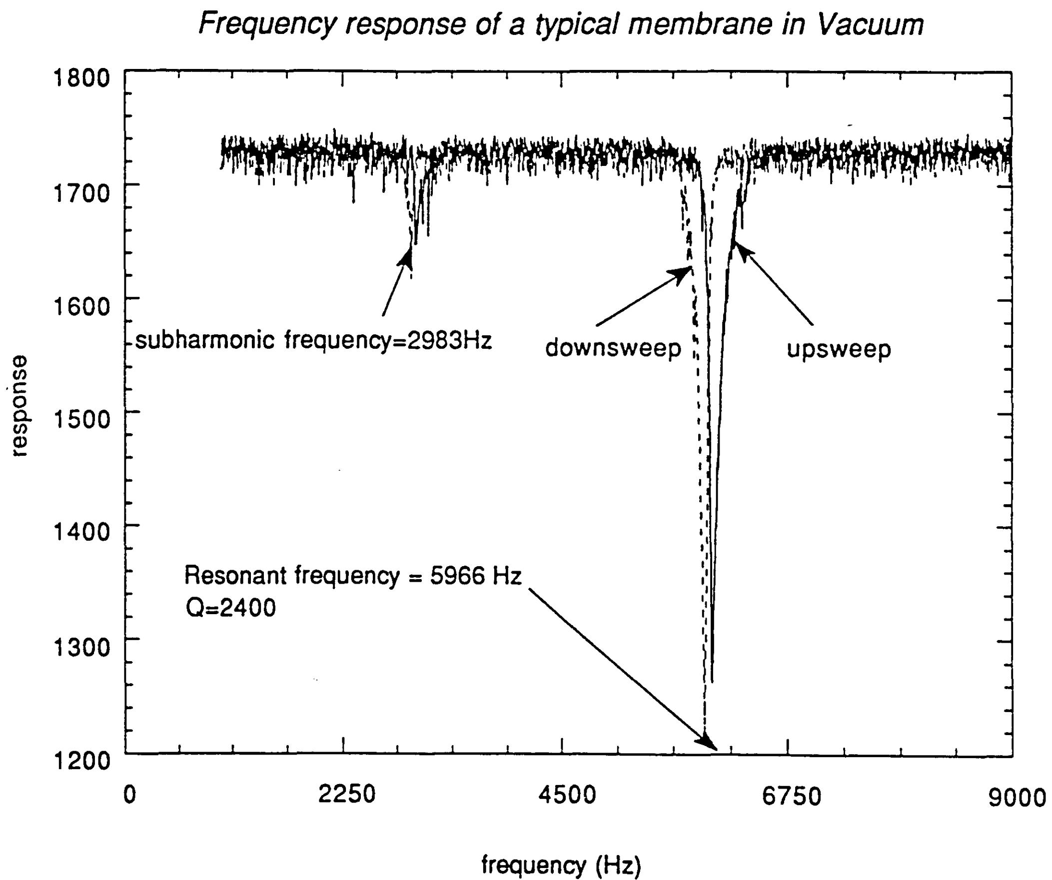

Figure 4.2. Plot of the frequency response for a membrane in vacuum using the in-situ frequency monitoring set-up.

The whole set-up in Figure 4.1 is located in an MRC 8620 rf sputtering system. A W target 15.2 cm in diameter, is positioned 5.8 cm above the x-ray mask. A shutter is interposed between the two prior to initiation of sputtering. An MKS-246 mass flow controller is used to set the Ar gas flow rate in the sputtering chamber, and an MKS-252A throttle valve is used to set the sputtering chamber pressure based on the MKS-390HA pressure sensor and readout unit. All these instruments are tied to an MKS-288 IEEE interface unit which allows a computer to set and monitor the chamber pressure.

Figure 4.3 depicts the set-up of the whole in-situ stress monitoring sputtering system. The control unit for the optical sensor, the Sycon STM-100 thin film thickness monitor, HP 3325B synthesized function generator, the peak detector circuit, and a MacII computer are all located outside the sputtering chamber. The computer acts as the central controller of the in-situ stress monitoring system. The signal generator is connected directly to the capacitor plate under the membrane. The electrostatic force applied to the membrane is proportional to the square of the applied voltage. Therefore, a DC offset in the applied voltage is used to maximize the driving efficiency, with the constraint that it does not cause a large non-linear decrease (i.e. not more than 10%) in the natural resonant frequency. Typically the generator is operated at 20 volt peak-to-peak AC with a +10 volt DC offset, sweeping times of 3-5 seconds, and a frequency range of 1 kHz to 10 kHz. The computer is equipped with a 12-bit A/D converter with an input range of ±10 V. Since the peak output voltage from the Fotonic sensor is only about 100mV at resonance, it is too small to be measured directly by the A/D card. An inverting peak-and-hold circuit, as shown in Fig. 4.4, is used to amplify and hold the signal, and filter out any noise. The computer is used to sweep the signal generator frequency across the range of interest while recording the vibration amplitude and finding the resonant frequency continuously throughout the

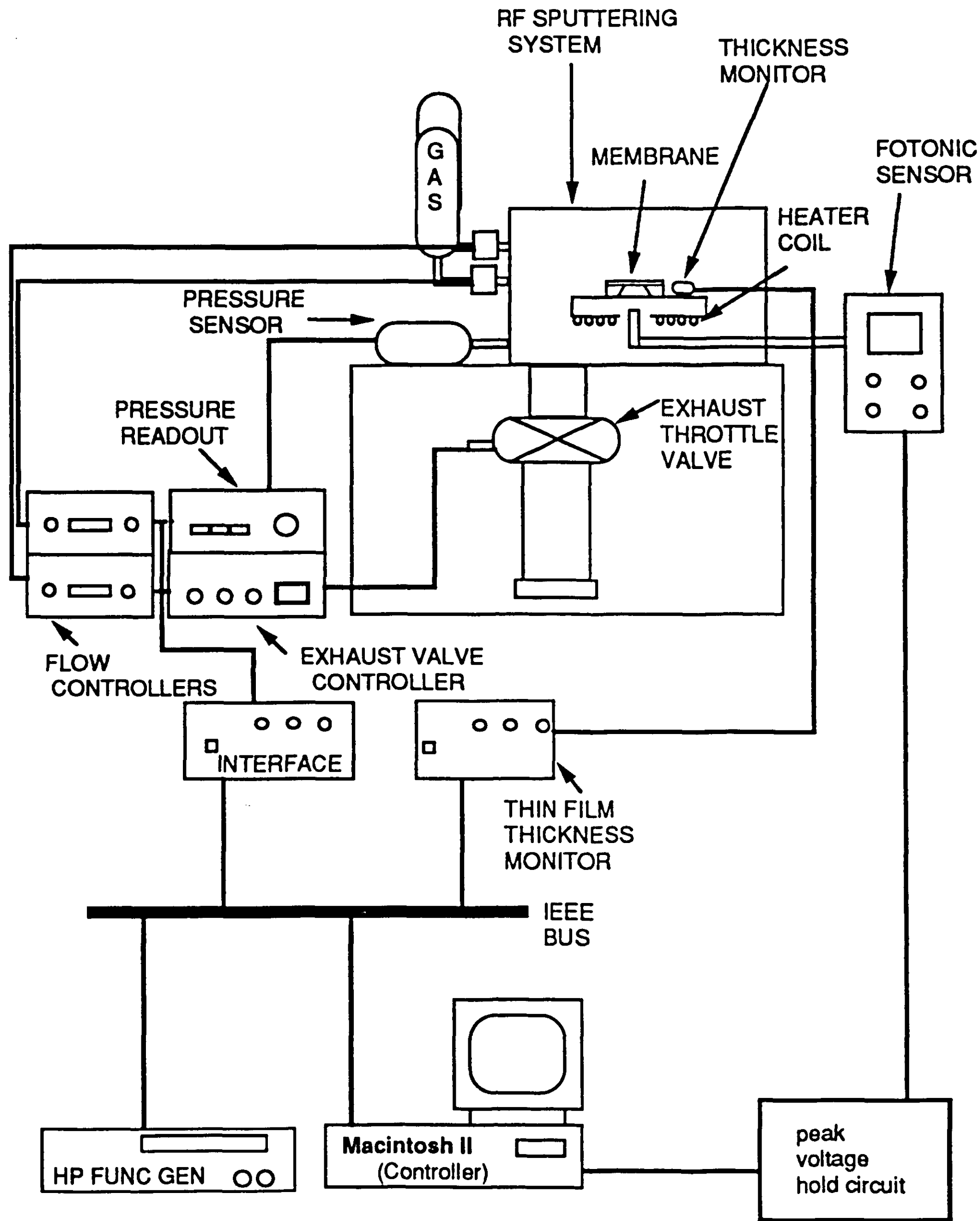

Figure 4.3. Schematic of the in-situ stress monitoring sputtering system.

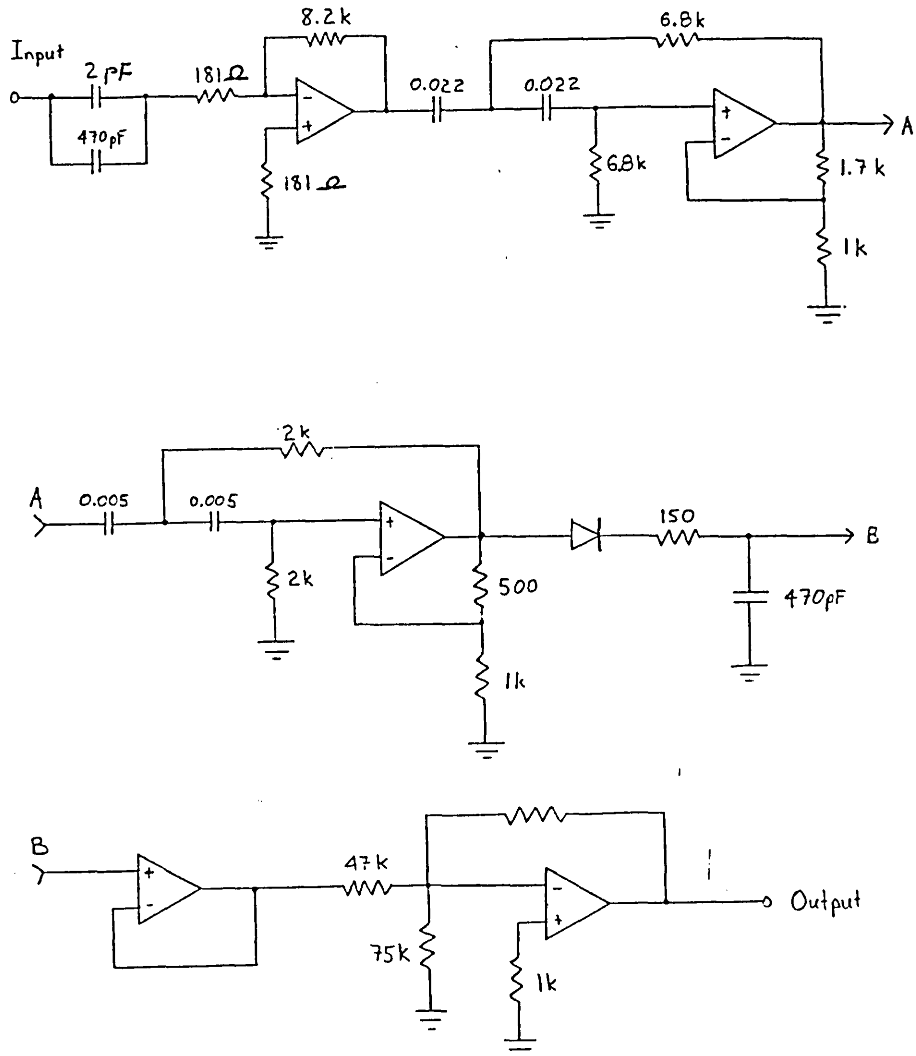

Figure 4.4. Inverting peak and hold circuit schematic.

deposition process.

A *LABVIEW II* program from National Instruments is used to facilitate the interface between the operator and the MacII computer during the sputtering process. Figure 4.5 shows the front panel displayed during the deposition process. On the bottom left side of the panel is all the data required to describe the membrane properties (e.g. density, radius, initial stress, and thermal expansion coefficient). On the top left side of the display is the control panel for the function generator that we used to drive the membrane. Here we can specify the sweeping frequency range, driving amplitude, and number of data points to be collected for each frequency sweep. On the bottom of the display is a graphical display of the membrane response to the frequency sweep, and all the data extracted or measured for that particular time interval of data collection (i.e. the measured resonant frequency, the ideal resonant frequency, sputtering pressure and deposited W film thickness). On top of this graphical display is a plot of measured membrane resonant frequency as a function of sputtering time. Finally the top right corner of the display is the control panel for the mass flow controller, which allows the direct setting of Ar flow rate into the sputtering chamber.

Both B-doped Si membranes and low stress SiNx membranes[19] were used. The former are 1 μm thick and 2.25 cm in diameter; the latter 1.8 μm thick and 2.54 cm in diameter. A 5nm film of Cr followed by 10nm of α-phase W is evaporated on the front side of the the membrane as a "seed layer". This is followed by loading the substrate into the chamber and sputtering W at 200°C. Ar flow rate was set at 25 sccm. Pressure was set to a predetermined value in the range 16-17 mtorr and controlled

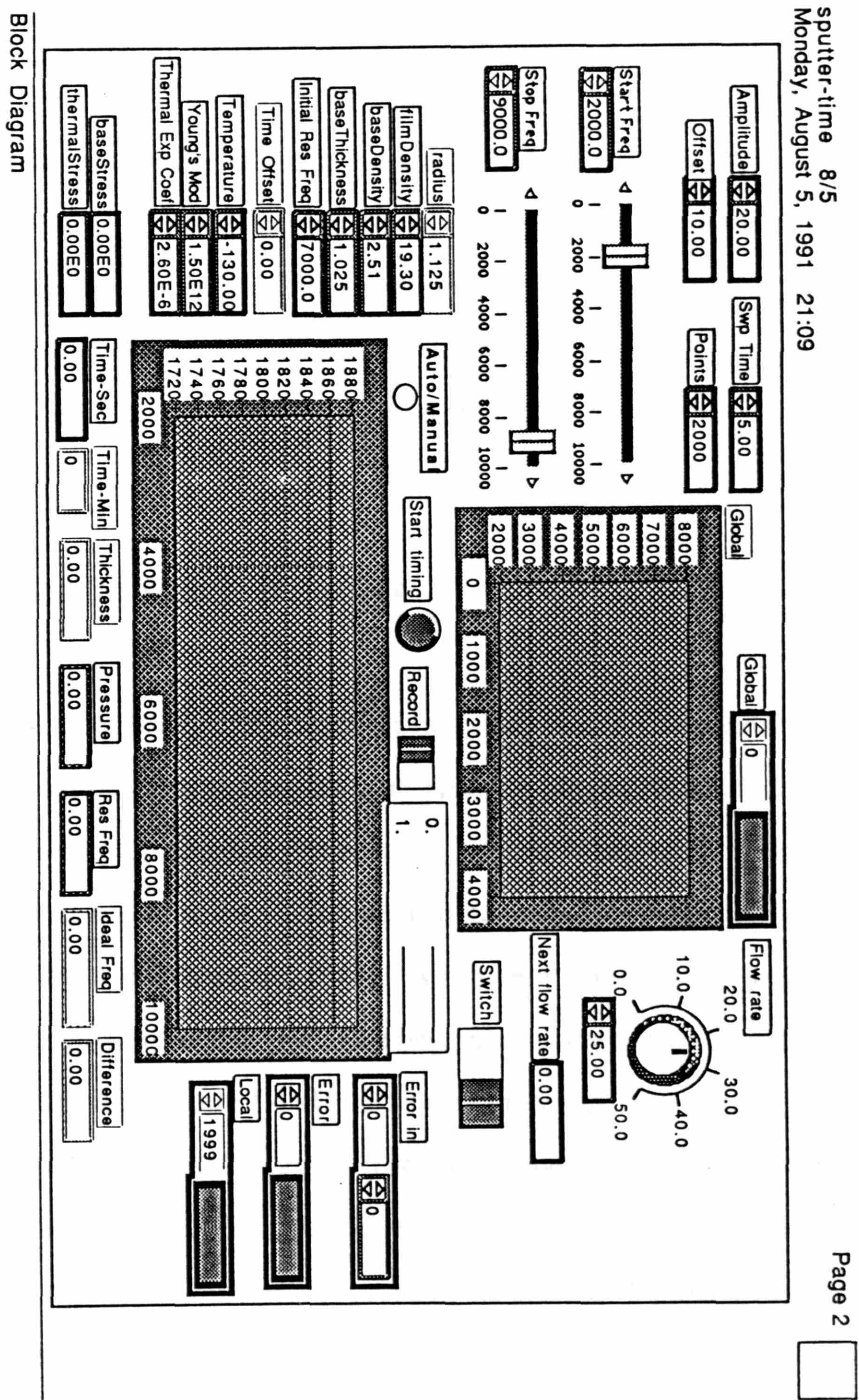

Figure 4.5. Front panel display from LABVIEW II for in-istu stress monitoring.

continuously throughout the sputtering run to within 0.05 mtorr using the MKS-252A throttle valve.

As described earlier, a Linnik interferometer is used to measure the stress in the sputtered W film. The procedure consists of etching a step in the W and measuring any resulting out-of-plane deflection of the membrane[1]. The minimum detectable deflection is ~10 nm which corresponds to a minimum detectable stress of ~5×10^7 dynes/cm^2, assuming a 400 nm thick W film and a membrane stress of 1×10^9 dynes/cm^2.

4.3 Experimental Results

To test the efficacy of the resonant frequency monitoring deposition, experiments were carried out on SiNx membrane with pressure ranging from 17.25 mtorr to 16.85 mtorr. Figure 4.6 plots resonant frequency, f_c, versus W thickness, t_f, for three values of pressure (the measured stress values are also given). The three SiNx membranes used differed slightly in thickness and stress. All three membranes showed similar drop in frequency of approximately 1.2 kHz at the beginning of the sputtering run when the shutter is opened, and approximately 1.4 kHz increase in resonant frequency when the shutter is closed at the end of the sputtering run. The drop in membrane resonant frequency can be attributed to the reduction of membrane tensile stress (more compressive) from the rapid heating of the membrane when it is exposed to the plasma. Similarly the rapid rise in the membrane resonant frequency when the plasma is turned off can be attributed to the increase in the membrane tensile stress (more tensile). After depositing about 80-100 nm of W the substrate temperature stabilizes and f_c follows a smooth curve in accordance with eq.(33). One can clearly see that the curvature differs for the three cases. Assuming that

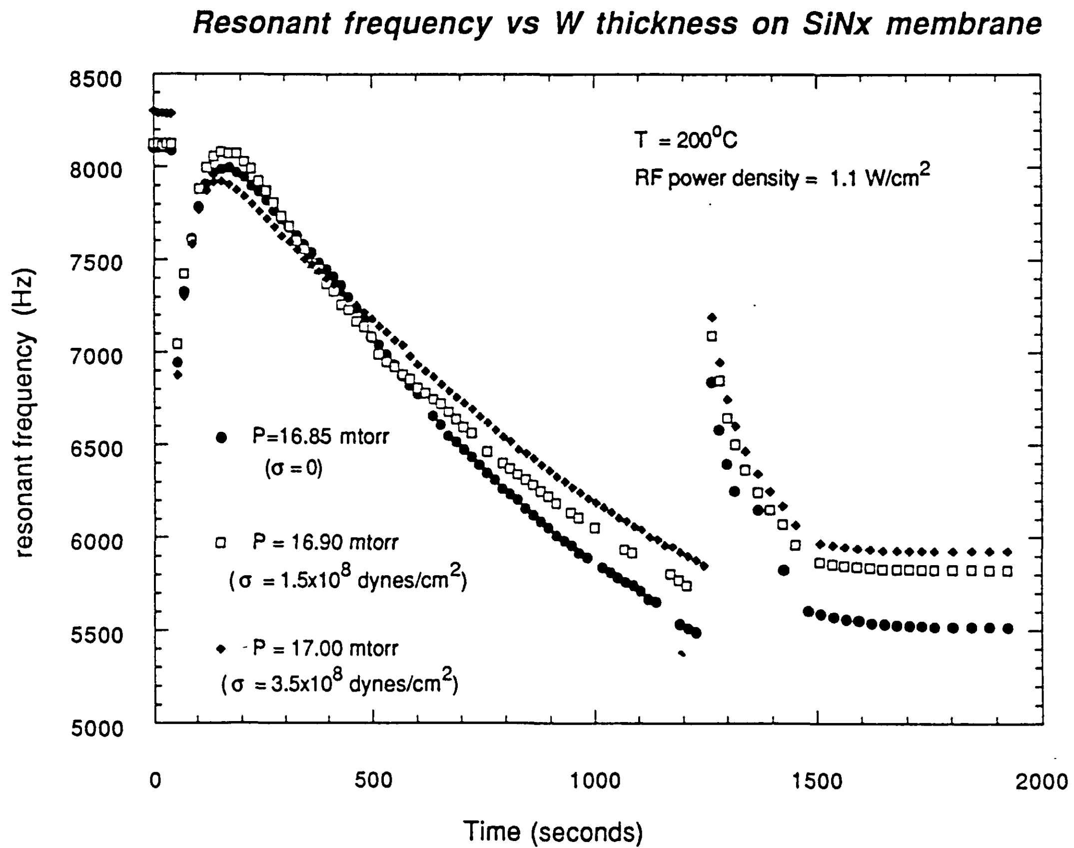

Figure 4.6. Plots of resonant frequency versus the sputtering time for three different sputtering pressure.

one works with a standard mask blank that has repeatable characteristics, the functional dependence of f_c on t_f should be sufficient to permit discrimination between a run that will produce zero stress and one that will produce a stress greater than 1×10^8 dynes/cm^2.

Beyond the issue of merely monitoring the progress of a W deposition run, experiments were carried out to explore the possibilities of controlling stress by altering the sputtering pressure during the run to obtain zero stress W film at the end of the sputtering run. An ideal response curve was first derived, experimentally, by incorporating an empirically determined constant temperature difference (~140°C) between the epi-Si membrane and its silicon frame into eq. (33). Preliminary results on epi-Si membranes, using a nonheated platform, are shown in Fig. 4.7. Fig. 4.7(a) shows a sputtering run carried out with a wide variation in pressure, causing the stress to vary about the ideal response, from highly compressive to highly tensile. Fig. 4.7(b) shows a sputtering run carried out over a smaller variation in pressure, and hence smaller stress variation around the ideal response. Nevertheless, as long as the final experimental point falls on the ideal response, the W stress at room temperature will be effectively zero.

Furthermore if one works with a standard mask blank that has repeatable characteristics, the functional dependence curve of f_c on t_f can be obtained for a zero stress W film sputtered on a blank mask. Once this functional form is obtained, it could then be used as the ideal response curve for stress control to sputter W on similar mask blanks.

4.3.1 Stress Control in SiNx membrane

Figure 4.8 gives stress versus sputtering pressure for a tungsten film sputtered on SiNx membranes of 1.8μm in thickness and 2.54cm in diameter. The sputtering condition is the same as usual, with 5nm of evaporated Cr followed by 10nm of evaporated W seed

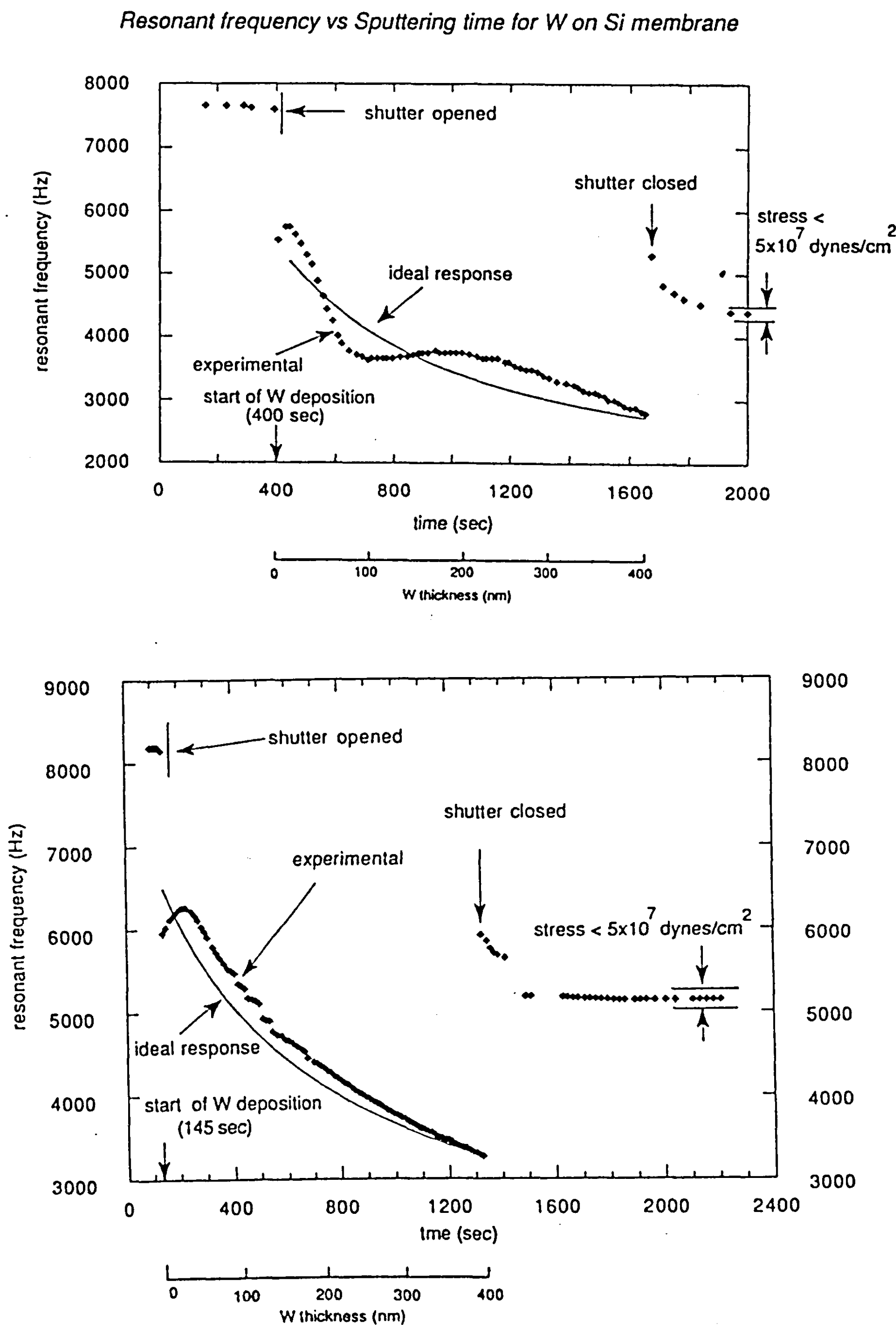

Figure 4.7. Plots of resonant frequency versus sputtering time for two different sputtering runs and two different varaitions in pressure. The final film stress is less than 5x10^7 dynes/cm^2.

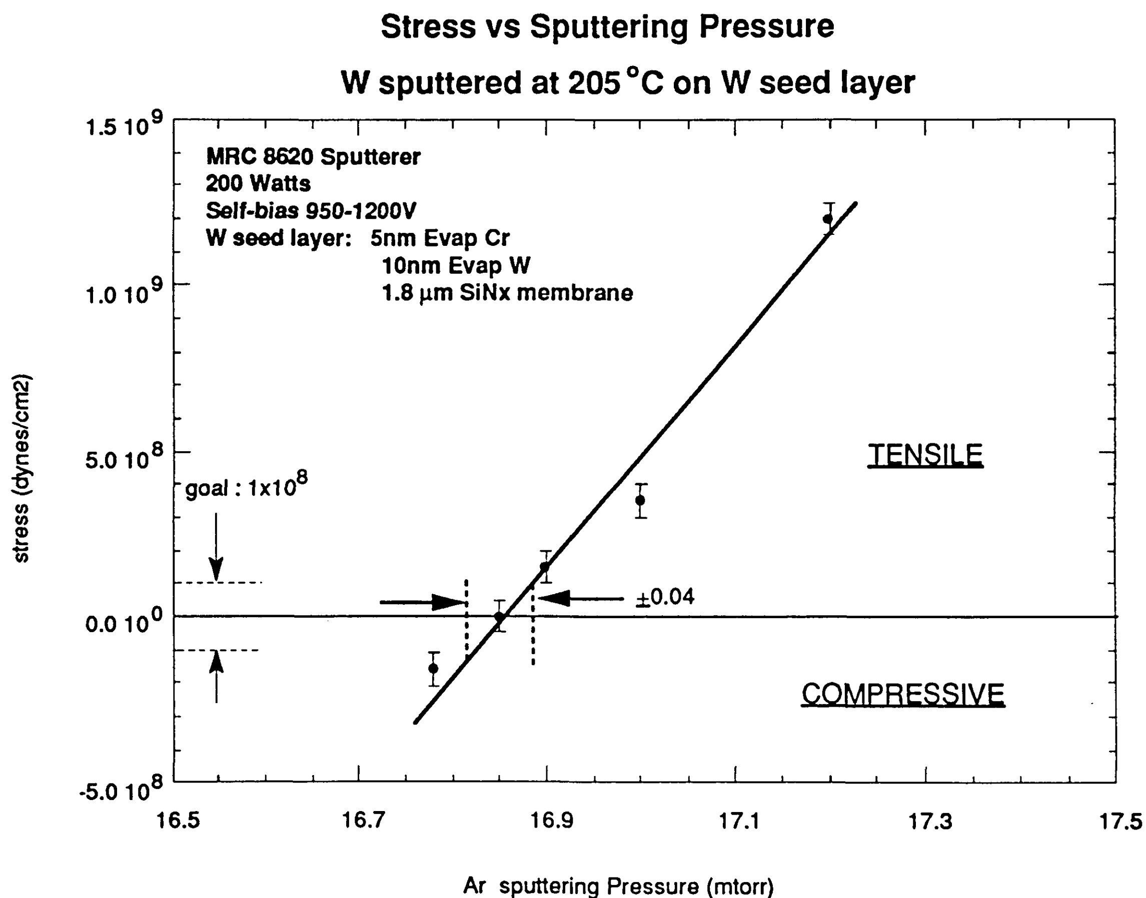

Figure 4.8. W absorber stress versus sputtering pressure for W film sputtered on the SiNx membrane over a small sputtering pressure range.

layer. Again, we see a very steep slope in the stress versus sputtering pressure curve. Therefore, low stress W film (i.e. < 1×10^8 dynes/cm^2) can be obtained if the sputtering pressure is set within ± 0.04 mtorr of the zero stress pressure of 16.85mtorr.

Furthermore the sputtering runs were carried out over a period of two months to check the repeatability of the zero-stress W sputtering condition and the corresponding frequency response during these sputtering runs. Four SiNx nitride membranes, with similar geometry and thickness, were used for the experiments. Once the zero stress (i.e. < 5×10^7 dynes/cm^2) pressure was found for W sputtered at an elevated temperature of 200°C on these nitride membranes coated with Cr-W seed layer, more sputtering runs were carried out under the same sputtering conditions and substrates to check the repeatability of getting zero stress W film. Figure 4.9 shows the repeatability of getting zero stress W films when sputtering runs were carried out at a fixed pressure of 16.85 mtorr. The pressure was fixed at 16.85 mtorr and controlled to $\pm$ 0.01 mtorr, that is, the drift in the pressure during the run was less than 0.01 mtorr. In addition to fixing the sputtering pressure, the runs were carried out with a fixed Ar flow rate of 25 sccm, and sputtered at an elevated temperature of 200°C with a plasma power density of 1.1 watts/cm^2.

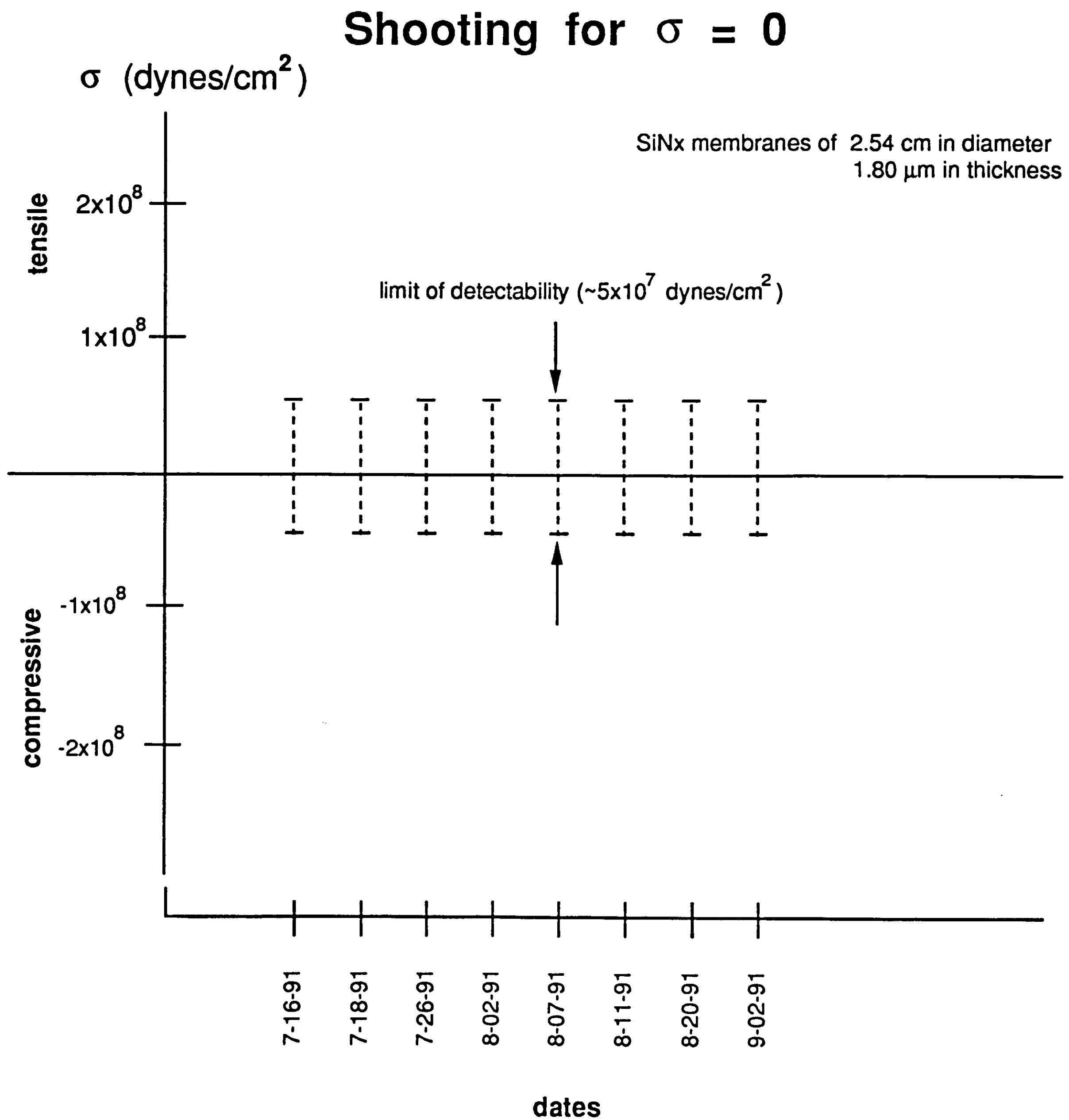

Figure 4.9. Demonstration of the repeatability of getting zero stress W film on SiNx membranes using the in-situ stress monitoring system.

Chapter 5

Membrane Characterization

The basic building block of x-ray masks starts with membrane, therefore there are some essential requirements being placed on the membrane materials and they are: (1) transparency to x-rays, (2) smoothness, (3) flatness, (4) dimensional stability, (5) high mechanical strength, (6) chemical durability, (7) high optical transparency, (8) low susceptibility to radiation damage, and (9) fabrication ease. In addition a x-ray mask has a rather unusual large aspect ratio difference in its geometrical configuration (it is usually 1-2μm thick and 2-4cm in diameter), the mechanical strength is of critical importance in developing a good x-ray mask technology. Presently there are many membrane materials being proposed to be used for the x-ray masks such as boron doped epitaxial Si, boron doped diffused Si, SiC[22], SiN_x, poly Si[32], diamond (C), Si_3N_4/Poly Si/Si_3N_4, and $Si_3N_4/SiO_2/Si_3N_4$ sandwich structures. As part of the effort to identify the "best" membrane material [33-39] to be used for x-ray lithography, a series of test procedures and equipments were developed to examine some of the critical membrane properties and the requirements.

5.1 Membrane Test Set-up

5.1.1 Bulge Test Measurement

As we mentioned earlier, one of the most important properties for a membrane is the mechanical strength. The other important mechanical property is Young's Modulus. A high Young's modulus is required to minimize the in-plane distortion due to the absorber stress as discussed in Chapter 2. A bulge tester was set-up to measure three mechanical properties of various membrane materials: intrinsic stress, Young's Modulus, and the tensile strength (or the breaking strength). These mechanical properties are compared among various membrane materials. Figure 5.1(a) depicts the schematic of a bulge tester. For the stress and bulk Young's Modulus measurement, the supporting rim (typically a Si wafer) was placed in contact with a sealing o-ring. The membrane was placed inside a leak-poof stainless steel chamber, with a circular transparent glass window on the top. This whole set up was placed on a microscope stage. A positive pressure was applied by flowing nitrogen into the enclosed chamber, and a digital pressure meter was used to monitor the differential pressure being applied. A digital z-axis readout unit was connected to the optical microscope to show the relative deflection. Two readings were taken at each pressure point to determine the absolute deflection, one at the center of the membrane and another at the edge of the membrane. Once the membrane was loaded inside the chamber, a series of pressure and membrane deflection data were then taken. Typically the pressure was stepped from 0 to approximately 6 psi at a increment of 0.1 psi. The measured data set was then analyzed and curve fitted using the load-deflection equation [33-39]:

$$P = \frac{4\,t\,h}{r^2}\left(\sigma_o + \frac{2}{3}\frac{E}{1-\nu}\frac{h^2}{r^2}\right) \qquad (34)$$

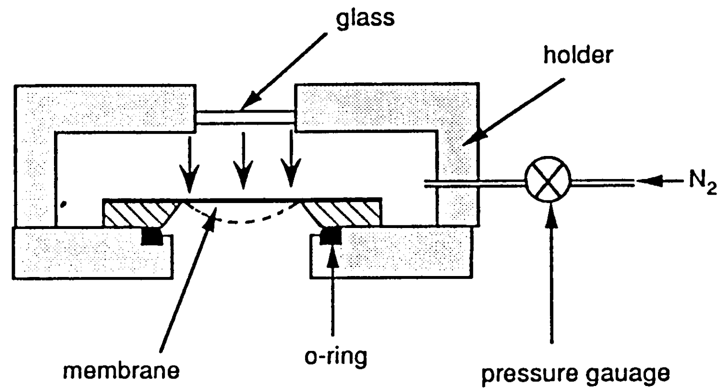

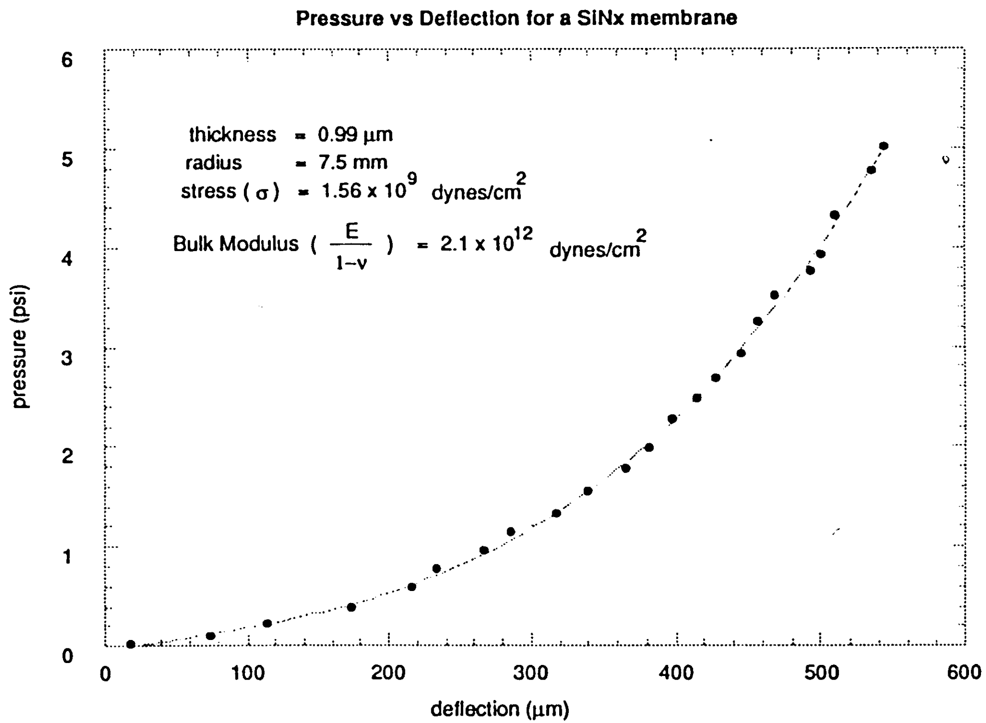

Figure 5.1. (a) Schematic of bulge tester set-up. (b) Typical plot of bulge tester measurement of pressure versus deflection.

where P is the applied pressure, t is the thickness of the membrane, r is the radius of the membrane, σ_o is the residual stress in the membrane, E/(1-ν) is the Bulk Modulus, and h is the deflection of the membrane. The Bulk Modulus and the stress of the membrane can be extracted from the above equations. Figure 5.1(b) shows a typical load-deflection data for a membrane and the extracted value for the stress and Young's Modulus.

The bulge test apparatus was also used to measured the burst strength (mechanical strength) of the membrane materials. In this test, the membrane was placed directly in contact with an o-ring and the pressure was applied until the breakage of membrane. This burst pressure (P_b) provides a mean to compare the strength of different membrane materials. However, when using this set-up, membrane could slip against the o-ring as the applied pressure increases. Thus a larger membrane deflection than the true deflection (deflection of membranes with a rigid frame) would be measured. Using the measured burst pressure, the following formula is used to compute a normalized Figure of Merit (FOM) for comparing different membrane materials: [35]

$$FOM = P_b \frac{D^2}{t \ h_b} \tag{35}$$

where D is the "o-ring" diameter, t is the membrane thickness, and h_b is the maximum membrane deflection right before the membrane breakage.

In order to gain some understanding regarding the relationship between the membrane strength and the membrane stress, a short analysis will be presented here. The burst pressure, P_b, is defined as the pressure when the membrane reaches the *apparent tensile strength* , σ_{app}, of the membrane material. The apparent tensile streength is defined as:

$$\sigma_{app} = \sigma_T - \sigma_o \tag{36}$$

where σ_o, is the membrane stress, and σ_T is the tensile strength of the memebrane. σ_o is positive when the membrane stress is tensile and negative when it is compressive. The breaking pressure, P_b, is related to the apparent tensile strength by the following equation [37-38]:

$$P_b = \frac{1}{\sqrt{K(v)^3 E}} \frac{t}{r} (\sigma_T - \sigma_o)^{3/2} \qquad (37)$$

$$K(v) \sim 0.41 \ (0.18 < v < 0.5)$$

where r is the radius of the membrane, t is the membrane thickness, and E and v are Youngs' modulus and Poisson's ratio for the membrane materials. Ideally, according to eq.(37), either reducing the membrane tensile stress or increasing the film thickness is effective in obtaining membrane with higher tensile strength (higher breaking pressure).

5.1.2 Mechanical Properties Comparison Results

Various membrane materials have been fabricated and tested using the bulge tester set-up, and the results are summarized in Table 1. As an indication of the extraordinary strength of the nitride membrane, Fig. 5.2 shows a quarter wafer with a 1 inch diameter of low stress nitride membrane used as a vacuum window for a x-ray system. Note the curvature of the membrane when a pressure differential of 1 atmosphere was applied across the 2 cm diameter membrane area enclosed by the o-ring. Also it should be pointed out that

Summary of Membrane Tests

Membrane Material (d) (Test dia., D, 20mm)	(a) Break Point (atm) P_{bp}	thick-ness (μm) t	(b) max. deflect. (μm) h_{bp}	(c) typical stress (dyn/cm²) x 10^9 σ_m (meas.)	(c) Bulk Modulus (dyn/cm²) x 10^{12} $\frac{E_m}{1-\nu}$ (meas.)	(d) FOM (atm) x 10^5	Optical Trans. T @ 633nm (%)	x-ray rad. dose J/cm² (Δσ)	# of trials
UCB Nitride	> 1.0	2	930	0.6 - 1.5	1.5-1.9	>2.2	58.1	8400 (<2%)	4
MIT-ICL Nitride	> 1.0	2	1057	3 -4	1.0	>1.9	63.6		2
Epi-Si (Source 1, SF)		1		0.9 - 1.4		1.3	43.4	9800 (0%.)	3
Epi-Si (Source 1, NSF)	0.08	1	456	1.1 - 1.4	2.0	0.70	40.3-47		2
Poly Si (Source 2)	0.33	1	2288			0.58	17		1
SiC (Source 3)	0.13	1.3	540			0.74			1
SiC (Source 4)	0.06	0.86	404	1.2	2.4	0.69			1
Nitride/Poly/ Nitride (MIT)	0.97	1.2	1705			1.9			1
Nitride/Oxide/ Nitride (MIT)	0.50	1.5	611			2.2			1

(a) &(b) The burst pressure and the maximum deflection height were measured using the bulge tester with the membrane touching the sealing o-ring. For complete discussion please refer to pg. 86 of this thesis.

(c) The stress and bulk modulus were measured using the bulge tester with the supporting rim (typically the Si wafer) placed in contact with the sealing o-ring.

(d) The test diameter (20mm) refer to the diameter of the sealing o-ring used in the burst test measurement, and not the actual membrane size.

$$FOM = P_{bp} \left[\frac{D^2}{t\, h_{bp}}\right]$$

1 atm = 100 kPa
1Pa = 1 N/m² = 10 dynes/cm²

SF = stacking faults

Table 1 Membranes characterization and comparison table.

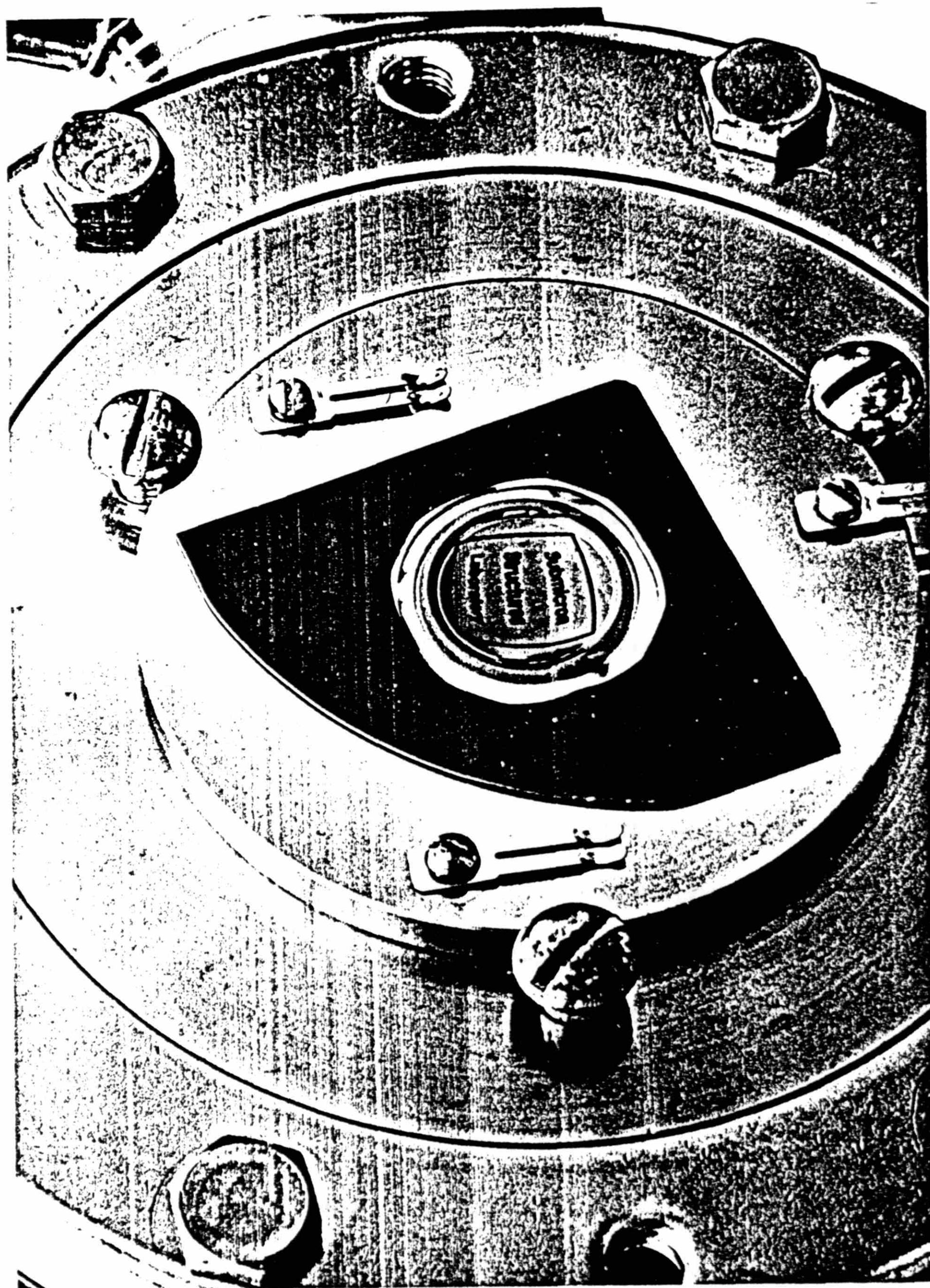

Figure 5.2. Demonstration of the high strength of low stress LPCVD nitride membrane, used as a vacuum window for a x-ray system.

even though SiC is believed [22] to be a promising membrane material for the x-ray mask in the future due to its high Young's Modulus, the mechanical strength from the two sources that were evaluated was very low compared to the Si-rich nitride. The main reason for the low strength of the membranes from these two sources may be the high defect density. Also interestingly, even though the sandwich structures of nitride/ploy Si/nitride membrane material offers high breaking strength, problem with low optical transmission makes it an undesirable membrane material.

5.2 Other Measurement Techniques

5.2.1 Resonant Frequency Stress Measurement

A resonant frequency method was developed to measure the stress of membranes. It is known that resonant frequency is a direct function of the membrane geometry and the membrane stress [30-31]. Thus it provides another way to characterize the membrane stress. Ideally the resonant frequency measurement can be done most accurately in an vacuum environment, since the stress (σ_o) can be directly related to the undamped resonant frequency (ν_{vac}) from the following equation:

$$\sigma_o = d_f [\, 2.61\, r\, \nu_{vac}]^2 \qquad (38)$$

where r is the radius of the membrane, and d_f is the density of the membrane. However for a day to day operation, the resonant frequency can be most easily measured in an atmospheric environment. The resonant frequency measured at atmospheric pressure was corrected for air loading to obtain the "vacuum" resonant frequency ν_{vac} which is given by:

$$\nu_{vac} = \nu_{air} \left[1 + 1.34 \frac{a\, d_a}{d_f\, t_f} \right]^{1/2} \quad (39)$$

where d_a is the density of air, t_f is the membrane thickness, and ν_{air} is the measured resonant frequency in the air. The stress of the membrane can then be calculated using eq(38). The density of dry air at 20°C at 760 mmHg is typically 1.204×10^{-3} g/cm^3. Figure 5.3 depicts the set-up built for the resonant frequency measurement in the air. The speaker with the frequency generator acoustically excited the membrane, and the microphone was placed directly behind the center of the membrane to measure the frequency response of the membrane. The output from microphone was then amplified and analyzed by an AC voltmeter to determine the resonant frequency of the membrane.

5.2.2 Alpha Step Profilometer Stress Measurement

Two additional techniques were also used to determine the stress of the deposited film. The first technique utilized a Tencor Alpha-Step stylus profilometer to measure the curvature of the wafer before and after the film deposition. From the change in wafer curvature over the scanned length of the profilometer, the stress of the deposited film can be calculated using Stoney's formula [33]:

$$\sigma_o = \frac{h}{3\, r^2} \frac{E}{1-\nu} \frac{t_s^2}{t_f} \quad (40)$$

where t_f and t_s are the thickness of the sputtered film and substrate, respectively, h and r are the difference in the bow for a given wafer before and after the film deposition over a radius r, E and ν are the Young's modulus and Poisson's ratio of the substrate. For

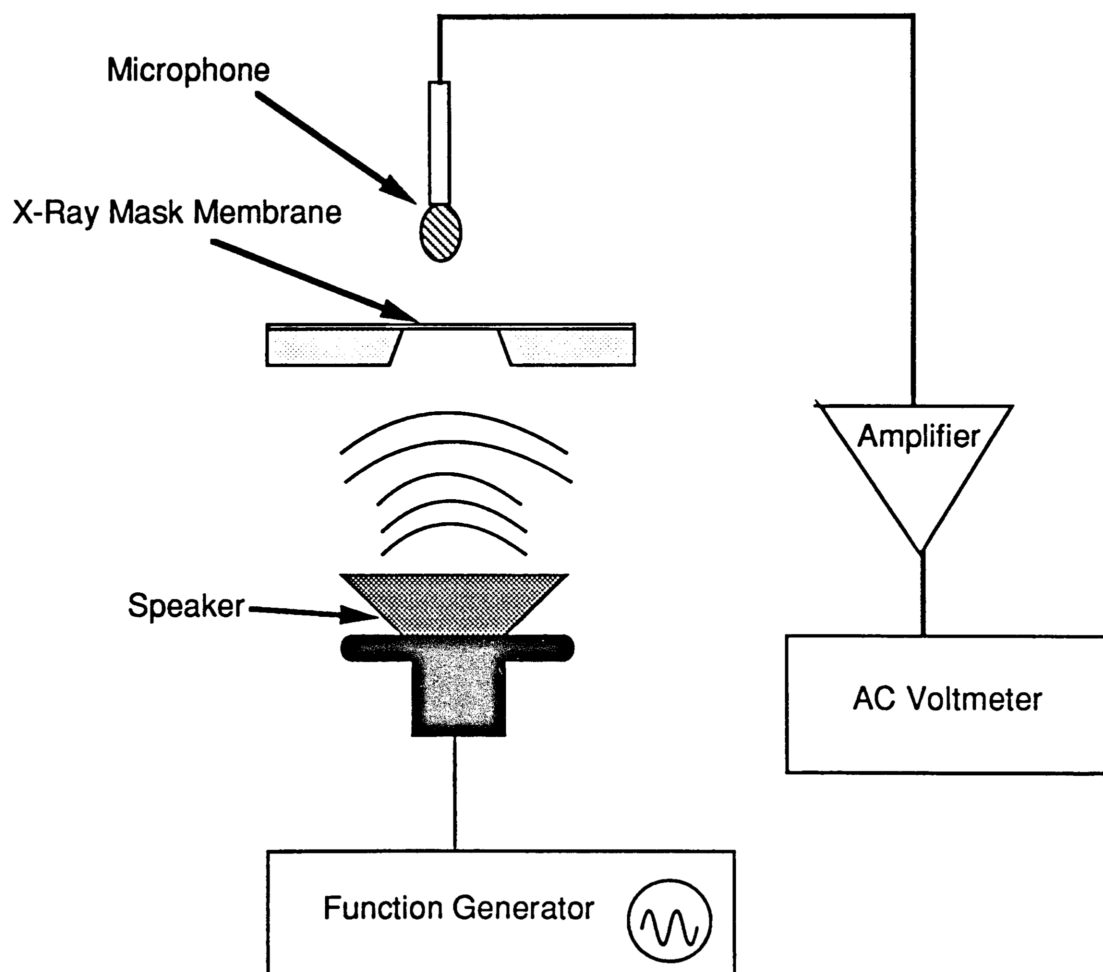

Figure 5.3. Sketch of resonant frequency measurement set-up in air.

example, the procedure used to measure stress of the deposited LPCVD SiNx film involved first stripping off, typically using RIE, the nitride on the back side of the wafer. This is to determine the wafer curvature due to the nitride film stress on the front side. Following the curvature measurement, SiNx film on the front side of the wafer was stripped off and the curvature of the plain wafer was re-measured. The difference between these two measurements would give the change in the curvature, h, due to the stress of the membrane film, and the direction of the change in curvature will provide the information on the stress type (compressive or tensile). Figure 5.4 shows typical scans before and after the film deposition for the stress measurement. Using this technique, a thinner substrate material and a longer scanning distance will be more desirable for higher accuracy. However, the maximum scanning distance for the profilometer is only 1cm, therefore the accuracy is limited to approximately $6\text{-}7\times10^8$ dynes/cm^2 when a 500 μm thick Si wafer was coated with 1 μm thick membrane film and with a change of deflection of 0.1 μm over an 1cm scanning distance.

5.2.3 Fizeau Interferometer Stress Measurement

The second measurement technique utilized a Fizeau interferometer (λ = 632.8 nm) to measure wafer curvatures before and after film deposition. The change in the bow of wafer can be measured from the change in the fringe patterns in the Fizeau interferograms taken before and after the film deposition. Fizeau interferometer offers the advantage of displaying the entire wafer curvature, and thus a large measurement area. Once the change in wafer curvature was measured, the stress could be computed using Stoney's formula. Figure 5.5 shows typical Fizeau interferograms, displaying wafer curvature, before and after the film deposition. Using this instrument, a change of one fringe in the wafer bow corresponds to a height difference of 316nm. Thus stress value down to 1×10^8 dynes/cm^2

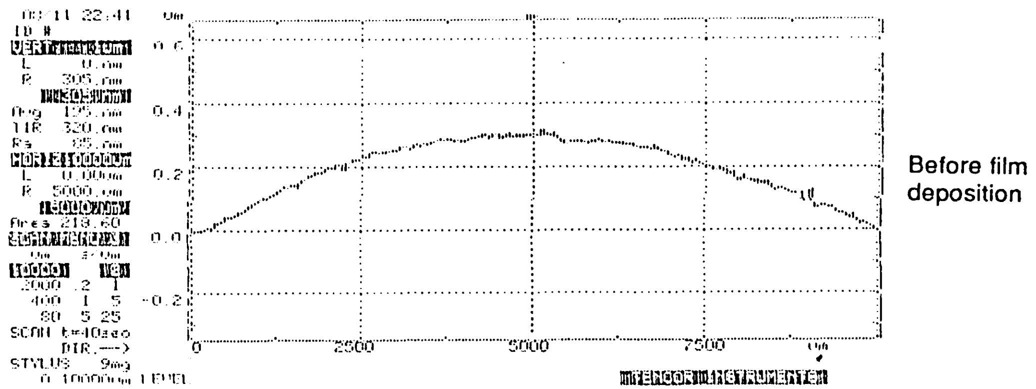

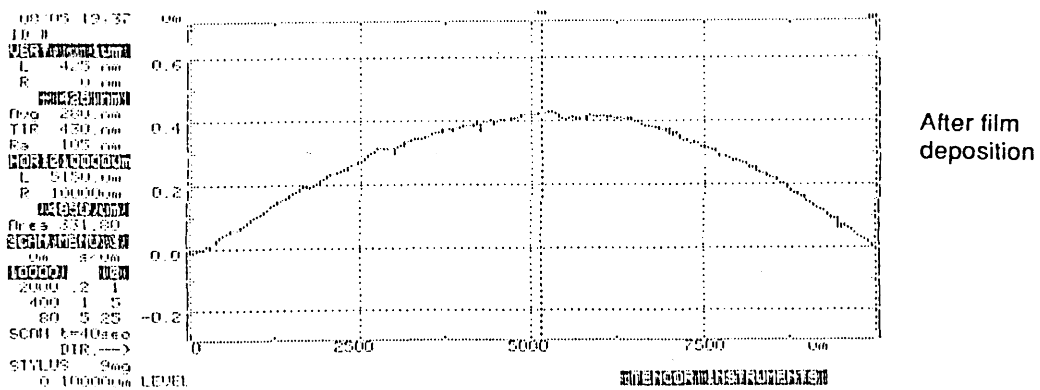

Figure 5.4. Plots from Tencor Alpha-Step Profilometer scanning over wafer surface before and after nitride deposition.

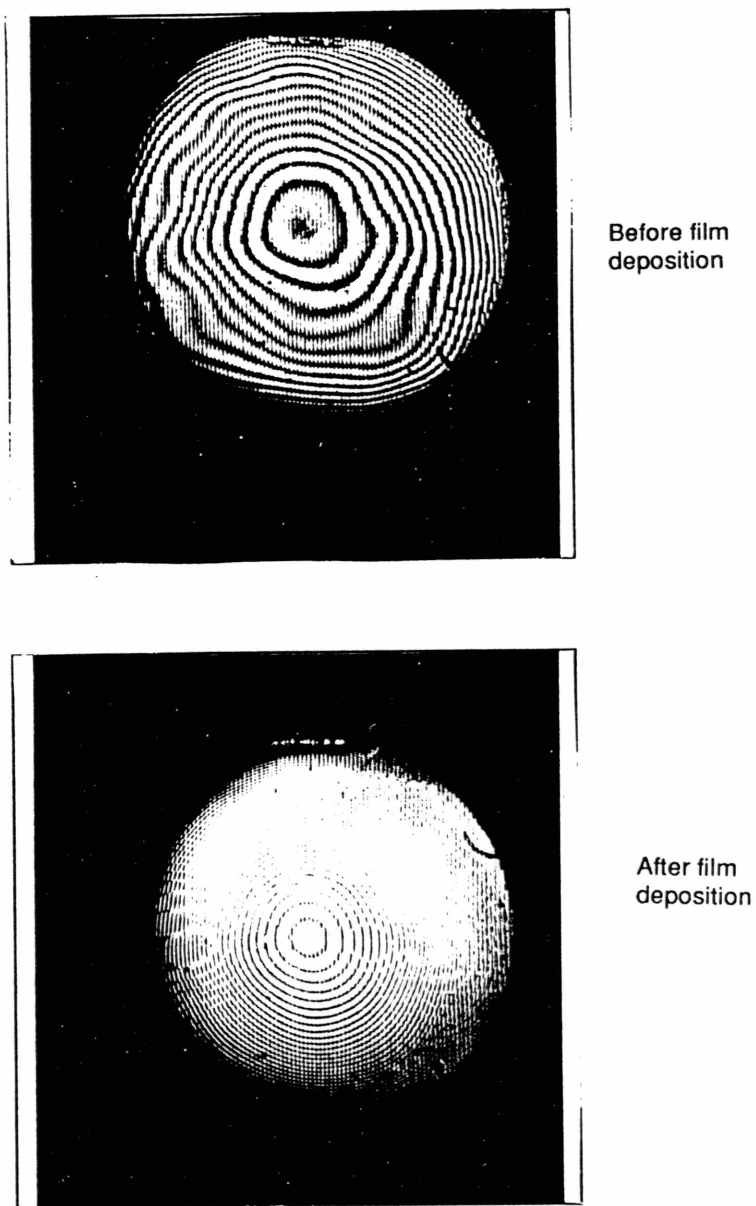

Figure 5.5. Wafer topography, before and after nitride deposition, measured with Fizeau interferometer. One fringe represent a height differential of 316.4nm.

can be resolved, assuming that a change in wafer bow of 316.4nm (i.e. one fringe), over a 4cm diameter area, was measured after a 500 μm thick Si wafer was coated with 1 μm thick membrane film on the front.

5.3 Additional Membrane Characterization Results

Applying various measurement technique mentioned in the earlier sections, mechanical properties of membranes from various sources can be measured and compared. Particularly these tests were performed to evaluate low-stress silicon-rich SiN_x deposited by low-pressure chemical vapor deposition (LPCVD). Three external sources of Si-rich nitride (source 1, 2, and 3) were evaluated. Deposition parameters and uniformity results are indicated in Table 2. It can be concluded from this table that due to the effects of gas depletion, a lower-pressure/lower-temperature/higher-flow-rate process can result in better thickness and stress uniformity. Nitride stress can be tuned simply by adjusting the flow ratio of dichlorosilane to ammonia and/or the LPCVD deposition temperature.

Nitride films obtained from source 1 were characterized by using various techniques mentioned in the earlier sections. From the resonant frequency measurement, it was determined that wafer to wafer stress uniformity was 1.32×10^9 dynes/cm^2 with a variation of ±3% across the 25 wafer boat. Average membrane thickness across the 25 wafer boat was approximately 0.95μm. Furthermore membranes, of 2cm in diameter, were etched from these batch of nitride films and their burst pressures were measured using the bulge tester. Using a 1cm diameter test o-ring in the bulge tester, burst pressure ranging from 0.6 to 3.7 atmosphere were obtained for these nitride membranes. Highest burst pressure was obtained on membranes from the middle of the the 25-wafer boat. This

	Source 1	Source 2	Source 3
$Si_2H_2Cl_2$	54 sccm	64 sccm	150 sccm
NH_3	9 sccm	16 sccm	25 sccm
Temperature	800±7 °C	835 °C	785±6 °C
Pressure	120 mtorr	300 mtorr	300 mtorr
Stress (tensile)	$2x10^9$ dynes/cm^2	$6x10^8$ dynes/cm^2	$3x10^9$ dynes/cm^2
Deposition Rate	30 Å/min	60 Å/min	30 Å/min
Uniformity	± 1%	± 45%	± 5%

Table 2. Nitride deposition parameters from three different sources.

indicates that the strength is most likely limited by particulate contamination during the deposition.

5.4 Radiation Stability of Nitride Membranes

Radiation hardness experiments were performed at the synchrotron of the University of Wisconsin Center for X-ray lithography. Vacuum resonant frequency of two low stress Si-rich SiN_x membranes, 4654 and 4837 Hz (or 7.13×10^8 and 7.7×10^8 dynes/cm^2) respectively, were measured before and after x irradiation with large doses of synchrotron radiation. These two membranes were subjected to doses of 8400 J/cm^2 (~17.5 MJ/cm^3) and 12500 J/cm^2 (~26 MJ/cm^3) respectively, and these doses correspond to approximately one million exposures (assuming a 10mJ/cm^2 resist). The change in resonant frequency for these two membranes after the irradiation were 47 and 57 Hz, which correspond to a stress change of 1.4×10^7 and 1.7×10^7 dynes/cm^2 respectively. This represents a stress change of less than 2% from the original membrane stress. Oizumi etal. [42] have shown that if oxygen is excluded from LPCVD nitride then it is radiation hard. The low stress Si-rich nitride membranes used for this radiation experiments may include a small oxygen contamination.

Chapter 6

Reactive Ion Etching of Tungsten

Once a low stress tungsten is sputtered, the ability to etch features in the sub-micron regime is one of the important criteria in the x-ray mask fabrication. Some of the requirements for successful pattern transfer from the resist level to tungsten are: the ability to etch tungsten with high selectivity (between the W and the etch mask), high directionality (minimum lateral etch rate), and a reasonable etch rate. Experiments were carried out to investigate the feasibility of reactive ion etching (RIE) W lines down to 0.25μm or below.[17-23] Several etching parameters were investigated for the W RIE experiments. These parameters were: etching gas or gas mixtures, flow rate, pressure, bias voltage, and power. The etching gas/gas mixtures that were investigated for W etching were: $CBrF_3$, CCl_2F_2, $CCl_2F_2/CF_4/O_2$, and $CCl_2F_2/CHF_3/O_2$, CHF_3/SF_6. The proper gas flow rate and the pressure for each individual gas or gas mixtures were examined and optimized to get the highest etch rate and selectivity. In addition the use of low bias voltage for the etching of fine structures was also investigated. For low bias voltage and low pressure etching, a stable plasma cannot be sustained in the RIE system. Therefore a magnetic target, which increases the plasma density even at the low voltage and low pressure condition, was used to etch W.

6.1 Experimental Results

The initial experiments involved the RIE of W using a variety of gases and Microposit 1400-25 resist, 1μm thick. The resist was patterned in 2μm lines and spaces. The RIE parameters of gas compositions, bias voltage, pressure, and the magnetic field (to enhance plasma density) were varied. The following gases and gas mixtures were tried: $CBrF_3$, CCl_2F_2, $CF_4/CCl_2F_2/O_2$[26-27], and $CHF_3/CCl_2F_2/O_2$. The selectivities of $CBrF_3$[28] and CCl_2F_2 was about 1/2 (i.e. resist etched twice as fast as W), and the etch rate was slow, ~6 nm/minute for etching at a pressure of 10 mtorr, a bias voltage of 400 Volts, and a power density of 0.22 Watts/cm^2. The two mixtures had selectivities about 2 times better, and etch rates 2 to 6 times higher depending on the exact gas flow ratios. The scanning electron micrographs shown in Fig. 6.1 illustrates the vertical sidewalls (slope $<3^o$) obtained when gas mixtures of $CHF_3/CCl_2F_2/O_2$ with a flow ratio of 10:1:5, at a pressure of 10 mtorr, a bias voltage of 400 volts, and a power density of 0.22 Watts/cm^2 were used. From this initial results it appears that 0.25 μm linewidths should be feasible.

In order to carry out the etching experiments for linewidth of 0.25μm or below, samples of 500nm period gratings (250nm lines) were holographically exposed to define the desired linewidth on the W film. Figure 6.2 illustrates the basic sequence in the sample preparation. W film of 400nm thick was spun coated with 300nm thick anti-reflection coating (ARC) followed by 500nm of photoresist. The samples were then holographically exposed to define the 500 nm period gratings. Following the holography,

RIE of Tungsten

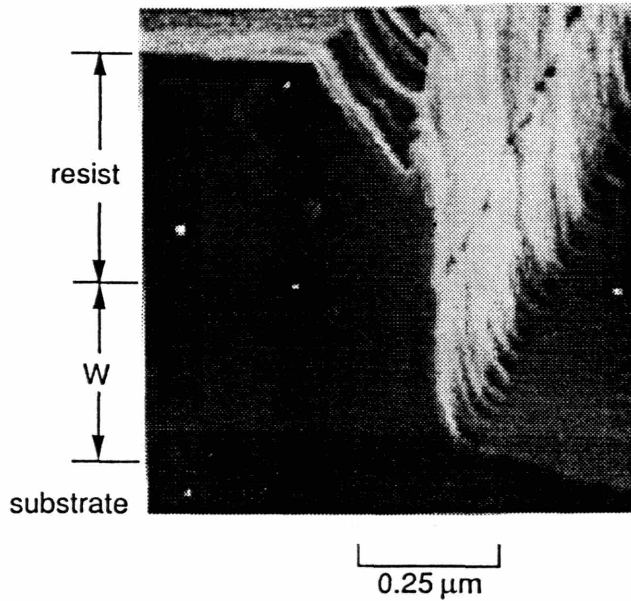

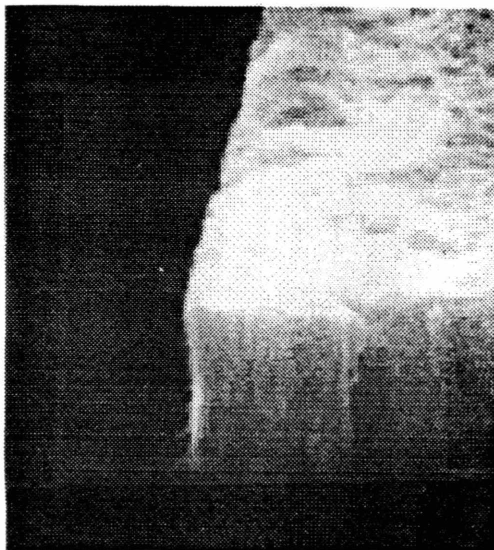

0.25 μm

Bias - 400 V
Power - 40 Watts
Pressure - 10 mtorr
Flow - CHF_3 / CCl_2F_2 / O_2
10 / 1 / 5
Rate - 34 nm/minute

Figure 6.1. W etching profile using gas mixtures of $CHF_3/CCl_2F_2/O_2$ mixed at a flow ratio of 10:1:5, using novalak-based photoresist as etch mask.

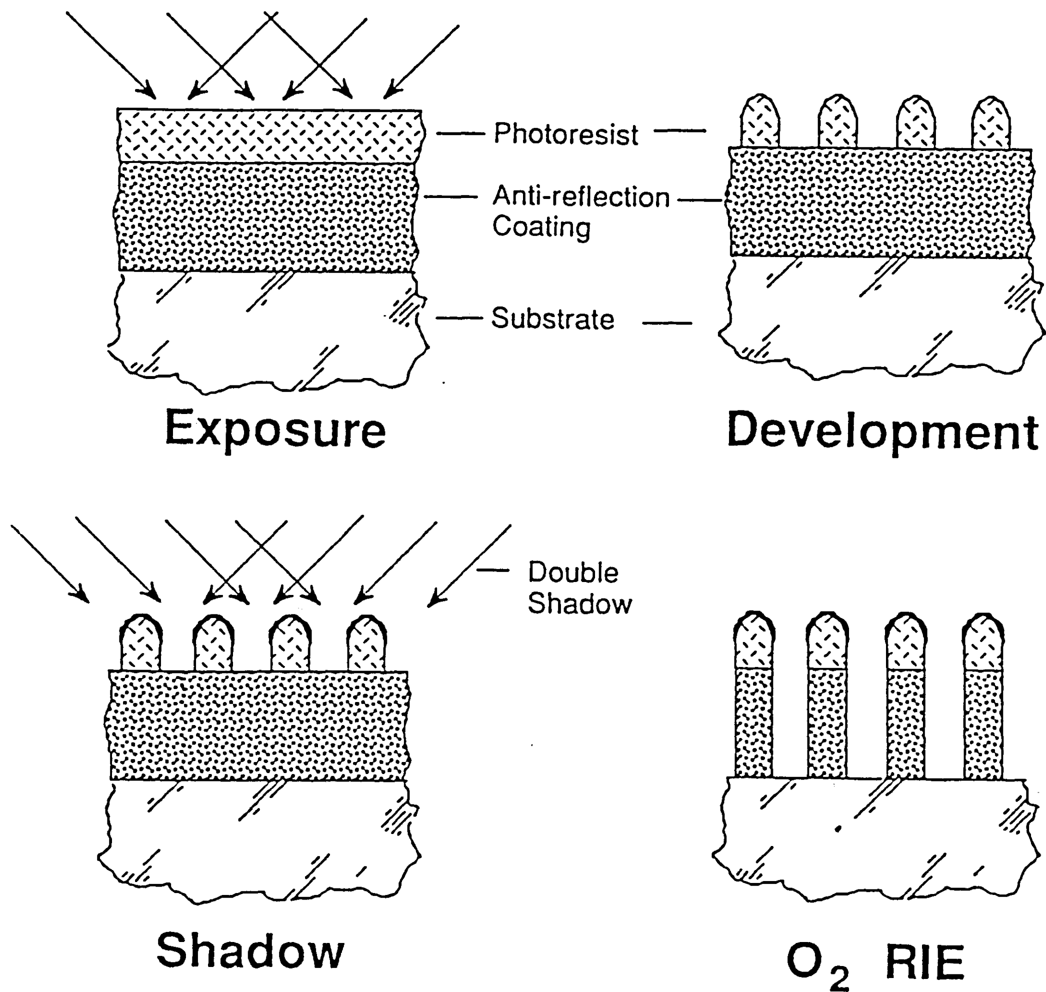

Figure 6.2. Diagrams illustrating the holographic process used to prepare samples for W RIE.

these samples were shadow evaporated with a thin layer of magnesium floride as an etch mask for the subsequent oxygen RIE to etch through the ARC layer and down to W layer. After the O_2 RIE the sample was ready for W etching experiments.

Tungsten etching was carried out using various gas mixtures as described earlier. Scanning electron micrographs of the W etching profile using gas mixtures of $CCl_2F_2/CHF_3/O_2$ are shown in Fig. 6.3 and Fig. 6.4. In both cases 0.25μm W lines were obtained. Figure 6.3 and Fig. 6.4 shows the etching profile of W lines obtained when etched at a bias voltage of 105 Volts and at a bias voltage of 600 Volts, respectively. However even with the "non-ideal" vertical profile, only a small change in the x-ray intensity profile is expected as indicated in Fig. 6.3. For both cases, the etching rate is approximately 20 nm/minutes. Furthermore this gas mixture was used to etch W grating lines of 50 nm [43] for a x-ray mask, and the corresponding PMMA exposure using the tungsten x-ray mask is shown in Fig. 6.5.

One of the main difficulties in optimizing the etching profiles and etch rate for the three gas mixtures is the large number of variables involved, i.e. parameters such as flow ratio for the three gases, bias voltage, and pressure. Therefore two gas combinations of SF_6 and CHF_3 was investigated for W etching. In this experiment, etching was carried out with all the other etching parameters held fixed except the flow ratio of SF_6 and CHF_3. Figure 6.6 shows the etch rate and the directionality achievable using this gas mixtures. Using the "optimized" parameters from this experiment, a vertical W profile (0.4μm thick and 0.25μm wide), is shown in Fig. 6.7. Minimum undercut were obtained using a SF_6/CHF_3 flow ratio of 1:1.8, with a bias voltage of 600 volts and at a power density

W RIE

CHF_3 : CCl_2F_2 : O_2

27 : 9 : 8

Bias Voltage 105V

Pressure 8 mtorr

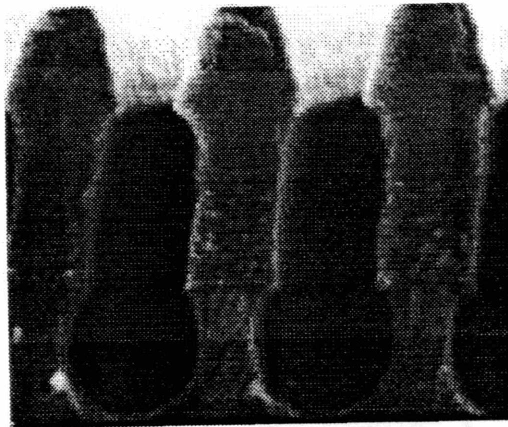

0.25 µm

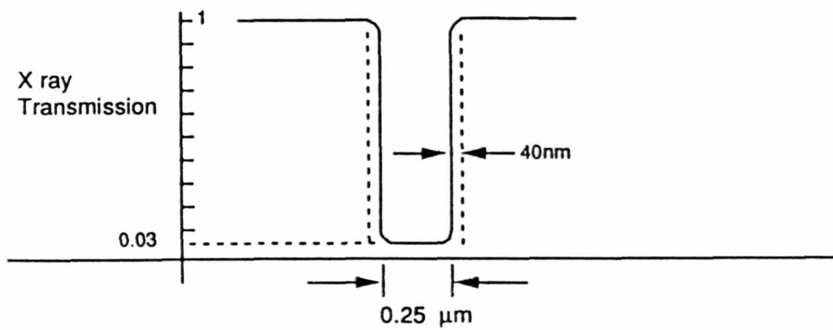

Figure 6.3. Scanning electron micrograph of W etching profile using $CHF_3/CCl_2F_2/O_2$ mixed at a flow ratio of 27:9:8, at a bias voltage of 105 volts and at a pressure of 8mtorr.

W RIE

CHF_3 : CCl_2F_2 : O_2

20 : 9 : 8

Bias Voltage 600V

Pressure 8 mtorr

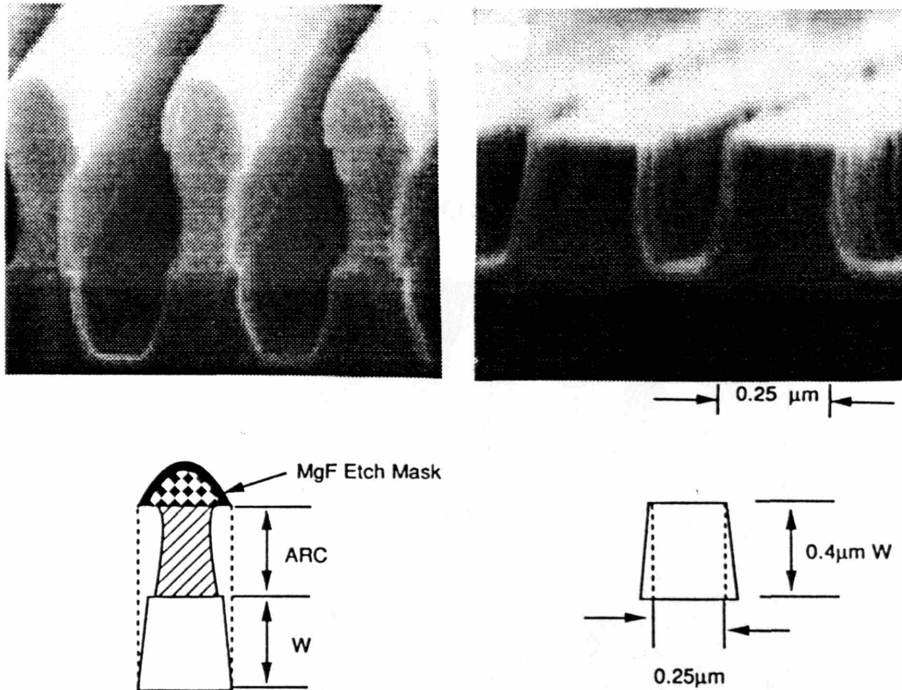

Figure 6.4. Scanning electron micrograph of W etching profile using $CHF_3/CCl_2F_2/O_2$ mixed at a flow ratio of 20:9:8, at a bias voltage of 600 volts and at a pressure of 8mtorr.

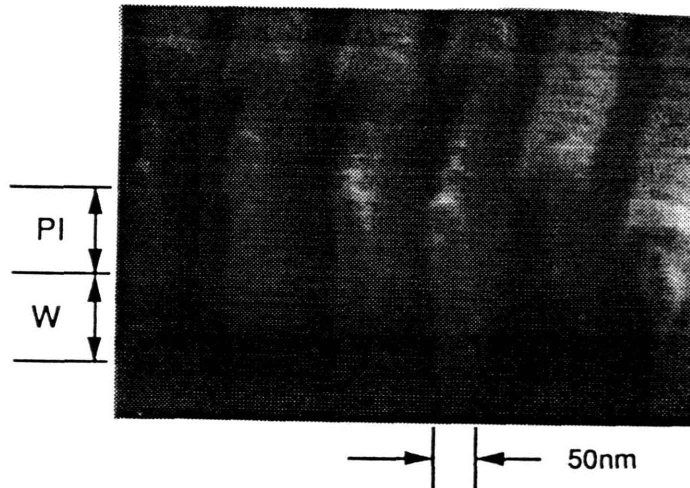

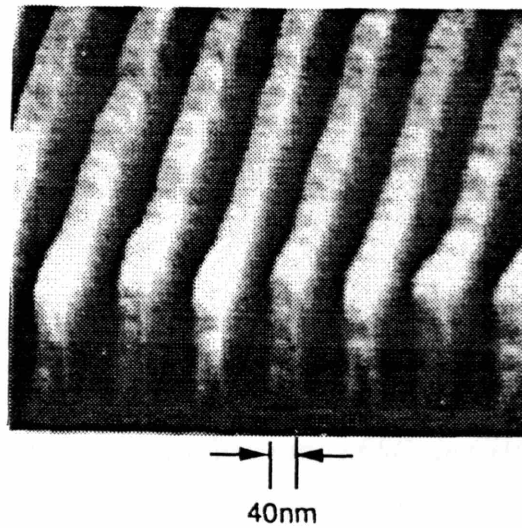

Figure 6.5. Top view shows 100nm period W grating lines for a x-ray mask etched using $CHF_3/CCl_2F_2/O_2$. Bottom graph shows the 100nm period PMMA lines exposed using the W x-ray mask shown on the top.

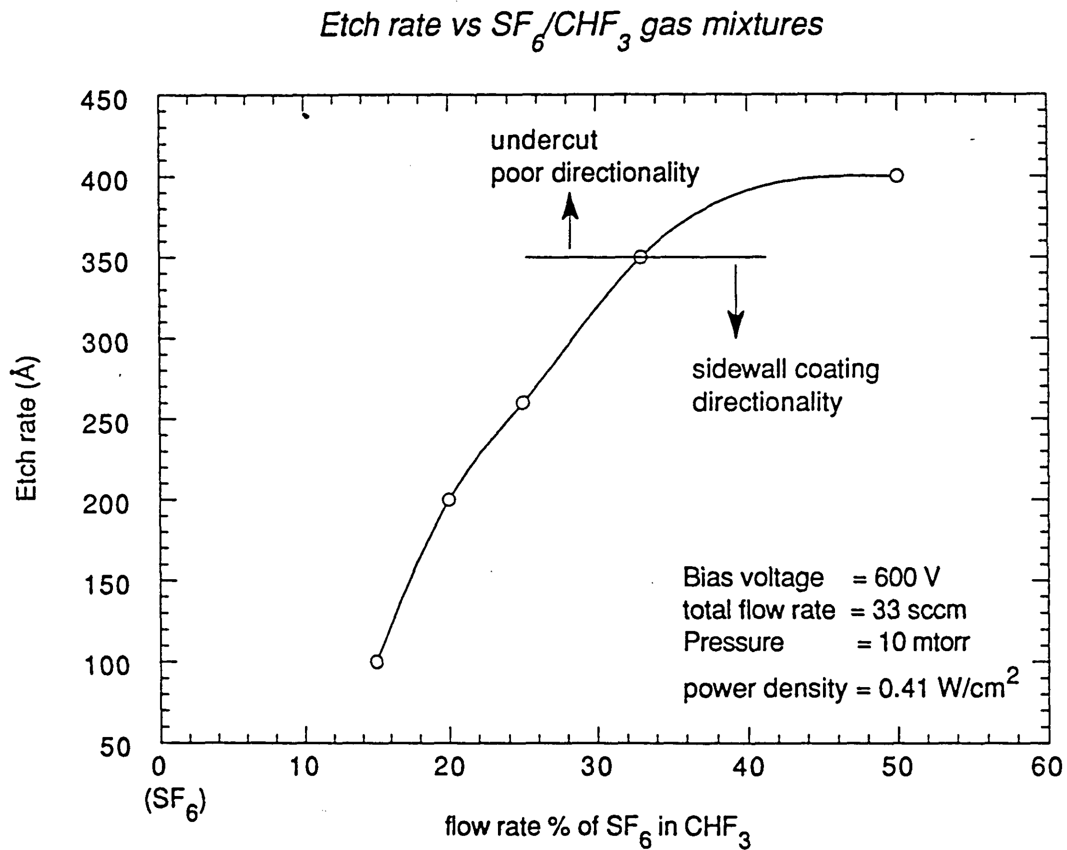

Figure 6.6. Plot of W etch rate versus gas flow ratio of SF_6 in CHF_3. A higher SF_6 flow ratio resulted in a faster etch rate and less directionality in the etching profile.

New RIE Process

Gas $SF_6 : CHF_3$
1 : 1.8

Bias Voltage : 600V

Pressure : 10motrr

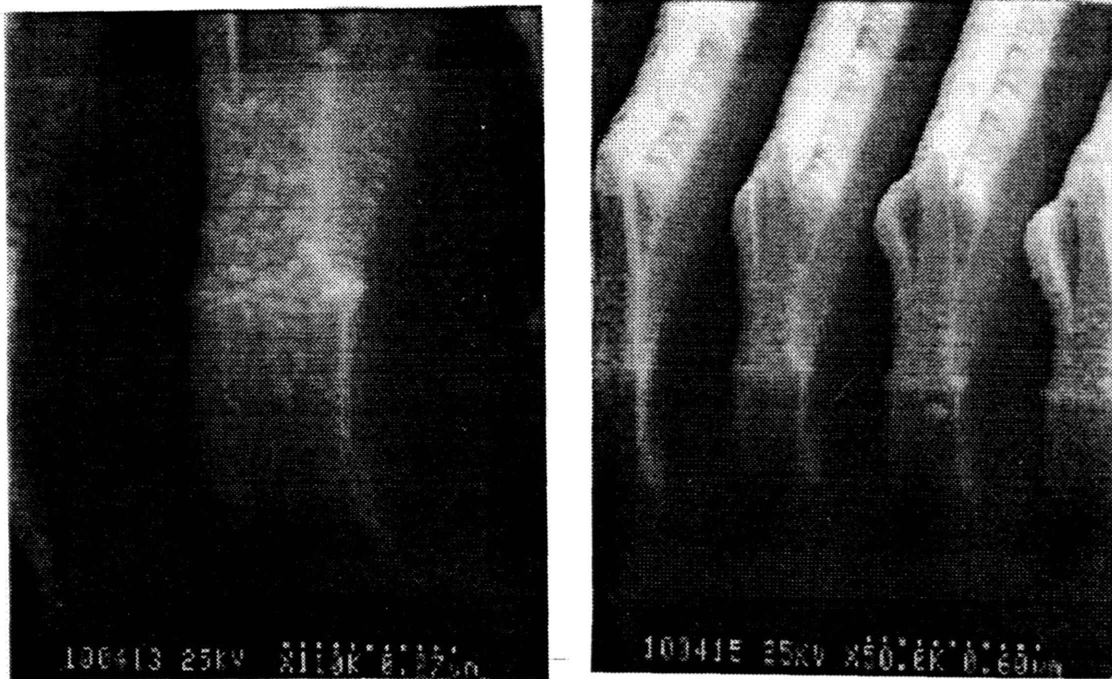

Figure 6.7. Scanning electron micrograph of W etching profile using SF_6/CHF_3 mixed at a flow ratio of 1:1.8, at a bias voltage of 600 volts and at a pressure of 10mtorr.

of 0.41 Watts/cm^2. A relatively high etch rate of 37 nm/minutes was achieved.

6.2 Membrane Backside Cooling

The main difficulties in etching of the W directly on the membrane is the heat dissipation during the etching process. The membrane, with its small thermal mass, tends to be heated up very quickly when it is exposed to the plasma during the RIE step. This will cause melting of the resist lines and hence complete failure of linewidth control. One way to overcome the heating problem is coat the backside of the membrane with diffusion pump oil during the etching process, and performing the intermittent etching as described earlier in chapter 2. However it is not a desirable process. A better solution is to provide a helium backside cooling[22], which will not only solve the problem of overheating of membrane but it should also provide better uniformity in the etching process[41].

Chapter 7

Conclusion and Future Work

7.1 Conclusion

This thesis has demonstrated the technologies required to fabricate distortion-free x-ray masks, compatible with minimum device feature size of 0.1 μm and below, using tungsten absorbers. Zero stress (i.e. $< 5 \times 10^7$ dynes/cm^2) α-tungsten films were obtained, by sputtering at fixed pressure with an elevated temperature, on substrates coated with Cr-W seed layer. The sputtered α-W films showed good thermal and radiation stability. Furthermore the high temperature sputtering process also demonstrated good stress uniformity across the whole x-ray mask.

A theoretical analysis of the OPD and IPD was also presented. Good correlation between the measured IPD and OPD was shown by direct measurement of the OPD through the Linnik interferometry, and IPD measurement through a moire technique.

An in-situ stress monitoring technique was also developed to track the resonant frequency behavior of the x-ray mask membranes during the tungsten sputtering process. Although no exact theoretical model could be developed to predict resonant frequency versus sputtered tungsten film thickness on various mask membranes, due to the variation

in mask properties (i.e. different mask membranes have different configurations, membrane materials, geometries, and thickness), an empirical curve was established using the in-situ stress monitor set-up for a specific mask membrane configuration. It was shown in the thesis that membranes with different absorber film stress, measured after the deposition run was completed, exhibited different curvatures in resonant frequency versus W film thickness curves. Furthermore it was demonstrated that as long as the resonant frequency at the final sputtered thickness falls on an empirically determined curve at the end of the sputtering process, a low stress tungsten film (i.e. $< 5\text{x}10^7$ dynes/cm^2) was obtained even with large excursions in the frequency versus W thickness curve.

Finally a tungsten RIE process using SF_6/CHF_3 gas mixtures was shown to etch 0.25μm W lines of 0.4 μm thick using an optimized flow ratio and etching parameters. It was found that a key point in successfully etching W with good linewidth control was the cooling of substrates coated with W.

7.2 Future Work

To further extend the process to deposit low stress tungsten films of $5\text{x}10^7$ dynes/cm^2 or below, improvements in both the precision in stress measurement, and the control and measurement of sputtering pressure. It was shown in Fig 4.8 that by setting pressure within 0.04 mtorr of the zero stress sputtering pressure, tungsten film stress of $1\text{x}10^8$ dynes/cm^2 could be obtained. Therefore if tungsten film stress of $5\text{x}10^7$ dynes/cm^2 or below is desired, pressure setting should be better than 0.02 mtorr within the zero stress pressure, and a pressure drift of less than 0.01 mtorr during the sputtering process should be ensured.

Also in order to extend the accuracy of distortion measurement (OPD and IPD) techniques, and to ensure that the correlation continue to apply for lower absorber stress,

improvement in the measurement apparatus will be required. First of all, in order to measure OPD of 10nm or below, an interferometry scheme with digital image processing will be required to measure smaller deflections induced by lower absorber film stress. The Wyco interferometer (discussed in Chaper 2) should have the capability to extend the OPD measurement down to a few nanometer range, that is, stress values down to a few 10^6 dynes/cm^2 range. Secondly, in order to measure smaller IPD induced by the absorber film using the moire technique, digital image processing techniques to sharpen the moire fringe pattern will be required. From the improvement of both distortion measurement techniques, it will enabled the determination of the correlation between IPD and OPD as the distortion approaches zero.

The ultimate goal for the in-situ stress monitoring sputtering system is the construction of an automated feed-back control loop to monitor and to control the sputtered film stress, and hence obtaining zero stress tungsten film all the time. From the initial results shown in Chapter 4, it should be feasible to develop an automated pressure control algorithm, which will enable the computer to keep track and to follow an empirically determined resonant frequency versus sputtered film thickness curve for a particular mask membrane, throughout the sputtering process.

Finally, once the low stress tungsten has been deposited onto the membrane, the final process would involve the transfering of the circuit patterns from the resist layer down to the tungstenabsorber. The main requirement would be the linewidth control during the etching process. It has been shown that if the etching can be carried out at a low substrate temperature[41], a uniform etching with good linewidth control is feasible. Therefore for a successful RIE of W on a x-ray mask membrane, the construction of a stage holder with He backside cooling is critical. By using a combination of backside membrane cooling with an optimized etching gas mixtures and etching parameters as discussed in Chapter 6, it should be feasible to fabricate x-ray masks with 0.1µm W lines or below.

Bibliography

[1] A. W. Yanof, D. J. Resnick, C. A. Jankoski, and W. A. Johnson, in *Proceedings of the SPICE*, Vol. 632, (Electron-Beam, X-Ray, and Ion-Beam Techniques for Submicrometer Lithographies V), Ed. P. D. Blais, 118, (1986).

[2] K.-H. Muller, P. Tischer, and W. Windbracke, *J. Vac. Sci. Technol.* ***B 4***, Jan/Feb, 230 (1986).

[3] Tsuneaki Ohta, Yoshiyuki Kawazu, and Yoshio Yamashita, *Jap, J. of Appl. Phys,* ***Vol 29***, Oct , 2195(1990).

[4] D. W. Hoffman and J. A. Thornton, *Thin Solid Films* ***40***, 355 (1977).

[5] D. W. Hoffman and J. A. Thornton, *J. Vac. Sci. Technol.* ***17***, 380 (1980).

[6] D. W. Hoffman and J. A. Thornton, *J. Vac. Sci. Technol.* ***20***, 355 (1982).

[7] R. C. Sun, T. C. Tisone, and P. D. Cruzan, *J. Appl. Phys.* Vol. **46**, 112(1975)

[8] A. Bensaoula, J. C. Wolfe, A. Ignatiev, F-O. Fong, and T-S. Leung, *J. Vac. Sci. Technol. A 2* , Apr/Jun, 389 (1984).

[9] M. Karnezos, R. Ruby, B. Heflinger, H. Nakano, and R. Jones,*J. Vac. Sci. Technol.* ***B 5***, Jan/Feb, 283 (1987).

[10] R.R. Kola, G. K. Celler, J. Frackoviak, C. W. Jurgensen, and L. E. Trimble, *J. Vac. Sci. Technol.* ***B 9*** Dec (1991).

[11] Masamitsu Itoh, Masaru Hori, Soichi Nadahara, and Ichiro Mori, *Proc. of 1989 Intern. Symp. on MicroProcess Conference*, p 85-88.

[12] Y. C. Ku, H. I. Smith, and I. Plotnik, *J. Vac. Sci. Technol.* ***B 6*** Jan/Feb, 2174 (1988).

[13] Y. C. Ku, H. I. Smith, and I. Plotnik, *Microelectronic Engineering 11*, 303 (1990).

[14] P.Petroff, T.T. Sheng, A. K. Sinha, G. A. Rozgonyi, and F. B. Alexander, *J. Appl. Phys*. Vol. **44**, 2545 (1973).

[15] R. S. Wagner, A. K. Sinha, T. T. Sheng, H. J. Levinstein, and F. B. Alexander, *J. Vac. Sci. Technol.* ***11***, 582 (1974).

[16] A. M. Haghiri-Gosnet, F. R. Ladan, C. Mayeux, H. Launois, and M. C. Joncour, *J. Vac. Sci. Technol. A 7*, 2663 (1989).

[17] Katsumi Suzuki, *Proc. of 1989 Intern. Symp. on MicroProcess Conference*, p. 76-78.

[18] H. Luthje, A. Bruns, H. Harms, I. Kohler, U. Mescheder, U. Mackens, T. Stuck, *Microelectronic Engineering 11*, 255(1990).

[19] T. H. Daubenspeck, E. J. White, and P. C. Sukanek, *J. Vac. Sci. Technol.* ***B 7***, 167 (1989).

[20] M. E. Burba, E. Degenkolb, S. Henck, M. Tabasky, E. D. Jungbluth, and R. Wilson, *J. Electrochem. Soc.,* ***133***, 2113 (1986).

[21] M. L. Schattenburg, I. Plotnik, and H. I. Smith, *J. Vac. Sci. Technol.* ***B 3***, 272 (1985).

[22] Masao Yamada, Kazuaki Kondo, Masafumi Nakaishi, Jinko Kudo, and Kenji Sugishima, *J. Electrochem. Soc.*, vol 137, 2231 (1990).

[23] W. S. Pan and A. J. Steckl, *J. Vac. Sci. Technol.* ***B 6***, Jul/Aug, 1073 (1988).

[24] L. G. Jaeger, *Elementary Theory of Elastic Plates*, chap. 1, Pergamon Press (1964).

[25] S. Timoshenko, and J. N. Goodier, *Theory of Elasticity*, chap. 2-4, 7, McGraw-Hill (1951).

[26] L. D. Landau and E. M. Lifshitz, *Theory of Elasticity*, p.52, Pergamon Press (1959).

[27] G. M. Welles, G. Chen, D. So, E. L. Brodsky, K. Kriesel, and F. Cerrina, *J. Vac. Sci. Technol.* ***B 6*** Dec (1988).

[28] Akihiko Kishimoto, Shinji Kuniyoshi, Naoto Saito, Takashi Soga, Kozo Mochiji, and Takeshi Kimara, *Proc. of 1990 Intern. MicroProcess Conference*, p. 92-95.

[29] B. S. Berry, W. C. Pritchet, and C. E. Uzoh, *J. Vac. Sci. Technol.*, Nov/Dec 1989.

[30] Lord Rayleigh, *The Theory of Sound*, (Dover Publications, New Yory), Chap 9 (1945).

[31] Morse and Feshbach, *Methods of Theoretical Physics*, Vol. III , 1452 (1565).

[32] L. E. Trimble and G. K. Celler, *J. Vac. Sci. Technol.* ***B 7***, Nov/Dec (1989).

[33] R. Glang, R. A. Holmwood and R. L. Rosenfeld, *Rev. Sci. Inst.* ***36***, 7 (1965).

[34] M. G. Allen, M. Mehregany, R. T. Howe, and S. D. Senturia, *Appl. Phys. Lett.,* Vol. **51**, 241(1987).

[35] C. E. Uzoh, J. R. Maldonado, S. S. Dana, R. Acosta, I. Babich, and O. Vladimirsky, *J. Vac. Sci. Technol. B 6*, 2178 (1988).

[36] J. W. Beams, *Structure and Properties of Thin Films*, edited by C. A. Neugebaur, J. B. Newkirk, and D. A. Vermilyea (Wiley, New York, 1959), p. 183.

[37] Misao Sekimoto, Hideo Yoshihara, and Takashi Ohkubo, *J. Vac. Sci. Technol.* 21(4), Nov/Dec (1982).

[38] Toshiki Ebata, Misao Sakimoto, and Satoshi Nakayama, *Jap. J. of Appl. Phys.*, vol. 21, No. 5, 762 (1982)

[39] E.I. Bromley, J. N. Randall, D. C. Flanders, and R. W. Mountain, *J. Vac. Sci. Technol. B 1*, 1364(1983).

[40] M. Kobayashi, M. Sugawara, K. Yamashiro, Y. Yamaguchi, *Microcircuit Engineering 11*, 237 (1990).

[41] Konstantinos P. Giapis, Geoffrey R. Scheller, Richard A. Gottscho, William S. Hobson, and Yong H. Lee, *Appl. Phys. Lett.*, 983 (1990).

[42] H. Oizumi, S. Iijima, and K. Mochiji, *Jap. J. Appl. Phys*, p.82 (1990).

[43] A. Yen, R. G. Ghanbari, Y. C. Ku, W. Chu, M. L. Schattenburg, and H. I. Smith, *Micorcircuit Enginnering* 1990.